Computational Study of Hydrogen Storage Materials for Fuel Cells

Thesis submitted to the

University of Pune

for the Degree of

Doctor of Philosophy

in Chemistry

By

Tuhina Kelkar

Research Guide: Dr. Sourav Pal

Physical Chemistry Division
National Chemical Laboratory
Pune – 411 008

September 2009

Computational Study of Hydrogen Storage Materials for Fuel Cells

Thesis submitted to the

University of Pune

for the Degree of

Doctor of Philosophy
in Chemistry

By

Tuhina Kelkar

Research Guide: Dr. Sourav Pal

Physical Chemistry Division
National Chemical Laboratory
Pune – 411 008

September 2009

Declaration

I, Tuhina Kelkar, hereby declare that the work incorporated in this thesis entitled,

Computational study of hydrogen storage materials for fuel cells

submitted by me for the degree of Doctor of Philosophy to the University of Pune is the record of the work I have carried out at the Physical Chemistry Division, National Chemical Laboratory, Pune – 411 008 from April 2007 to September 2009 under the supervision of Dr. Sourav Pal. Further, this work is original and has not formed the basis of award of any degree or diploma. Such material as has been obtained from other sources has been duly acknowledged in this thesis.

Date: ______________________

Tuhina Kelkar
Physical Chemistry Division,
National Chemical Laboratory,
Pune – 411 008

Certificate

CERTIFIED THAT the work done in the thesis entitled,

Computational study of hydrogen storage materials for fuel cells

submitted by **Tuhina Kelkar** for the degree of Doctor of Philosophy to the University of Pune, was carried out by the candidate under my supervision in the Physical Chemistry Division, National Chemical Laboratory, Pune - 411 008, India. Such material as has been obtained from other sources has been duly acknowledged in the thesis.

Date: ________________________

Dr. Sourav Pal
(Research Guide)
Physical Chemistry Division,
National Chemical Laboratory,
Pune – 411 008

To Mummy up above
and Daddy

Acknowledgements

It gives me great happiness in expressing my gratitude to Dr. Sourav Pal, my Research Guide for readily accepting me into his group at National Chemical Laboratory (NCL), Pune and for introducing me to the challenging world of hydrogen storage materials. I have to thank him for the freedom he gave me to carry out research in my individualistic way. I must also acknowledge Dr. Sourav Pal for his advice, guidance, and faith without which this work would not have been possible. It has been wonderful working under him and I have imbibed so much through this association. I will always remember a conversation during which he said that success should really be measured in terms of the view that our peers hold for us.

I am obliged to Director, NCL for providing me the infrastructure to carry out the work presented in this thesis. I am grateful to CSIR for funding my Junior Research Fellowship through the NMITLI Project and also for awarding me the direct Senior Research Fellowship. I am thankful to NCL, CSIR, DST, and CCSTDS for granting me the timely financial support to participate in WATOC 2008, Sydney and AsiaNANO 2008, Singapore.

I must next acknowledge Prof. D. G. Kanhere for the enriching discussions which helped improve the quality of my work on many an occasion. I am grateful to Dr. K. Vijayamohanan for his kind interest in my research. I cannot do without professing that it was my Organic Chemistry teacher at St. Stephens College, Dr. Eeswaran's passion which first instilled in me the dream of pursuing a career in research and brought me to the portals of NCL, Pune.

Life during these years at NCL would not have been as easy going had it not been for the varied associations. I thank my seniors Dr. Nayana Vaval, Sharan, Sophy, Akhilesh, Prashant, and Sajeev for their timely help and advice. I am particularly grateful to Sharan for teaching me how to use VASP and for his tremendous help during the initial phase of my Ph.D. In the last year of my Ph.D. I also had the fortune of interacting with the new scientists of our thriving group: Dr. Kumar Vanka, Dr. Neelanjana Sengupta, and Dr. Sudip Roy.

I have had great fun interacting with my batchmates and juniors Arijit, Subrata, Bhakti, Saikat, Ideh, Deepti, Sumantra, and Sapna. I must specially mention Himadri for being a competent System Administrator which kept the cluster running and Rahul for his uncomplaining company in Sydney. I cannot do without thanking Lalitha for her patient listening, sweet cheering, and for being a wonderful friend. I should also acknowledge our youngest team members Mudit, Jitendra, Sayali, and Debarati for their camaraderie and in particular Shantanu for helping me proofread this thesis.

Outside my lab, I will always remember my friends Meera for all the moments of joy and laughter, Manish Dubey for his thoughtfulness, and Azahar Machwe for setting the alarm bells ringing whenever my pace slackened.

I do not have enough words to convey my gratitude to my family for their kindness and unwavering support. I thank my elder sister Ulka and my brother-in-law Siddhartha for their sincere concern and good counsel. Daddy, I thank you for your seamless patience, words of wisdom, and the independence that you gave me. Daddy, I dedicate this thesis to you and Mummy, who I wish could have been here today with us. Finally, I thank someone for his unconditional encouragement, for understanding the importance that this Ph.D. holds for me, for motivating me in this crucial period of thesis writing, and for appreciating my aspirations.

Date:

Tuhina Kelkar

Contents:

List of Abbreviations:

The following abbreviations, in alphabetical order, that have been used in this thesis:

AE	All-electron
AIMD	*Ab initio* molecular dynamics
BOMD	Born-Oppenheimer molecular dynamics
BZ	Brillouin zone
CC	Coupled cluster
CI	Configuration interaction
CPMD	Car-Parrinello molecular dynamics
DFT	Density functional theory
DOS	Density of states
FC	Fuel cell
GGA	Generalized gradient approximation
HF	Hartree-Fock
HK	Hohenberg-Kohn
ICE	Internal combustion engine
KS	Kohn-Sham
LDA	Local density approximation
MD	Molecular dynamics
MOF	Metal-organic framework

MP	Møller-Plesset
PW91	Perdew and Wang 1991
PAW	Projector augmented wave
PEMFC	Polymer electrolyte membrane fuel cell
PP	Pseudopotentional
QHA	Quasiharmonic approximation
TF	Thomas-Fermi
USPP	Ultra-soft pseudopotential
VASP	Vienna *ab initio* simulations package

List of Figures:

List of Tables:

List of Publications:

This thesis is based on the following papers, which are referred to in the text by their Roman numerals:

I. **Theoretical investigation of complex metal hydrides: Potential hydrogen storage materials,** Tuhina Kelkar, Sharan Shetty, D. G. Kanhere, and Sourav Pal, *Proceedings of the 58th Chemical Engineering Congress of IIChE (CHEMCON-2005)*, New Delhi, 14-17 December **2005**.

II. **Density functional investigations of electronic structure and dehydrogenation reaction of Al- and Si-substituted MgH_2,** Tuhina Kelkar, Sourav Pal, and D. G. Kanhere, *ChemPhysChem* **2008**, *9*, 928-934.

III. **First-principles calculations of thermal equations of state and thermodynamic properties of MgH_2 at finite temperatures,** Tuhina Kelkar, D. G. Kanhere, and Sourav Pal, *Computational Materials Science* **2008**, *42*, 510-516.

IV. **Electronic structure, thermodynamics and kinetics study of Al- and Si-doped α, γ, and β phases of MgH_2 for hydrogen storage,** Tuhina Kelkar and Sourav Pal, *Journal of Materials Chemistry* **2009**, *19*, 4348-4355.

V. **Effect of M = Li^+, Na^+, Be^{2+}, Mg^{2+}, and Al^{3+} doping on hydrogen adsorption in metal-organic framework-5: a density functional study,** Tuhina Kelkar and Sourav Pal, **2009** (manuscript in preparation).

The following papers are co-authored by me but are not included in this thesis:

- **$Si_xC_{1-x}O_2$ alloys: A possible route to stabilize carbon-based silica-like solids?**
  Solid State Communications **2007**, *144*, 273-276.

Abstract

Fuel cells are rapidly turning into a cutting-edge technology of the future which will provide a very efficient and clean source of electrical energy and will be responsible for achieving the hydrogen economy. Besides stationary and portable applications, fuel cells can even power vehicles. This technology is driven by using hydrogen as the fuel. On-board storage of hydrogen by compression and liquefaction has several technical limitations. Solid-state hydrogen storage is an ingenious alternative.

Presently a number of materials are under investigation. But none are able to simultaneously meet all the criteria for practical vehicular storage of hydrogen. Therefore, today it is imperative to bring about breakthroughs in the existing technologies as well as develop new hydrogen storage materials. Experimentally this is a long drawn process requiring significant human and financial resources. Computational materials science in comparison is a fast and cost effective strategy for evaluating novel materials. In addition theory and simulations can be used for supporting experimental results.

Thus, the main motivation of this thesis is to use a computational approach to model different classes of hydrogen storage materials and to understand the hydrogen desorption processes associated with them. In the thesis we will be specifically studying magnesium hydride (MgH_2), complex metal hydrides, and metal organic frameworks (MOFs) due to their tremendous promise for the purpose of hydrogen storage and the need for enhancing their hydrogen storage properties. To this end, in the thesis we have performed density functional theory (DFT) based calculations to study theoretically the ground state lattice structure, electronic structure, chemical bonding, dehydrogenation thermodynamics, hydrogen desorption kinetics, and effect of (a) high pressure phases, (b) adding dopants, and (c) including lattice vibrations of these hydrogen storage materials.

The organization of the thesis will be as follows:

Chapter 1 Introduction

In Chapter 1 we will begin by giving a brief introduction to fuel cells and their advantages and applications. Thereafter we will describe the use of hydrogen as a fuel for fuel cells. This will be followed by providing a brief discussion on the problems associated with storage of hydrogen by compression and liquefaction. We will also expound on the three mechanisms of solid-state hydrogen storage. In addition we will review select few hydrogen storage materials, namely, clathrate hydrates, metal organic frameworks, intermetallics, magnesium hydride, and complex metal hydrides. We will end the chapter by describing the motivation behind the research carried out and by presenting an outline of the thesis.

Chapter 2 Theoretical background

In Chapter 2 we will present an outline of the theoretical framework behind the methodology used in the most part of the work presented in the thesis. We will begin with a brief introduction to the many-body problem by talking about the Hartree approximation, the Hartree-Fock (HF) approximation, and the methods which go beyond HF. This will be followed by a discussion on the use of density functional theory (DFT) as an alternative route for performing such calculations. Next a description of the concepts of molecular dynamics and *ab initio* molecular dynamics will be given. We will also explain and compare the ideas and algorithms behind Born-Oppenheimer molecular dynamics and Car-Parrinello molecular dynamics. Lastly, we will illuminate on the implementation of the plane wave-pseudopotential molecular dynamics method in the program package of VASP for performing solid-state calculations.

Chapter 3 Electronic structure

The term electronic structure refers to the energy levels of electrons and their distributions in space and momentum. Their characterization, calculation, and experimental investigations are central goals of condensed matter physics, materials science and chemistry. We will begin Chapter 3 with a discussion of the different tools available for studying electronic structure of solids. Our results of the charge density, band structure, and density of states (DOS) analyses on pure and Al- and Si-doped α-, γ-, and β-MgH_2 will be presented. It will be shown that bonding between Mg and H atoms is essentially ionic and that between Al/Si and H atoms is covalent. We will illustrate from the band structure and DOS calculations that Al and Si doping reduces the band gaps of the three phases of MgH_2. By examination of the partial DOS, it will be further shown that this reduction in band gaps is due to generation of additional bands arising from the Al and Si impurities. Finally, the decreased band gaps will be used to suggest that doping with Al and Si can destabilize α-, γ-, and β-MgH_2 and may lead to a possible lowering of their dehydrogenation reaction energies.

Chapter 4 Thermodynamics and kinetics of hydrogen desorption

In Chapter 4, questions regarding the energy requirement for removal of hydrogen and the activation energy barriers for hydrogen desorption will be addressed through our DFT based investigations on complex metal hydrides ($LiAlH_4$ and $LiBH_4$) and magnesium hydride (MgH_2). The effect of presence of metastable phases of these hydrides and the influence of doping with light elements Al and Si on the above mentioned properties will be illustrated. On the basis of enthalpies of formation and reaction energies it will be shown that amongst the complex metal hydrides under study dehydrogenation of β-$LiBH_4$ will require much less energy and will therefore have a greatly reduced dehydrogenation temperature making it the most potential hydrogen storage material. It will also be shown that doping with Si decreases the dehydrogenation energy of α-, γ-, and β-MgH_2 more than Al doping. The absence of similar consistent trends for activation energy barriers will exemplify the importance of studying hydrogen desorption kinetics along with dehydrogenation thermodynamics in order to choose a suitable additive for enhancing hydrogen storage of MgH_2.

Chapter 5 Effect of lattice vibrations at finite temperature

Over the years the stability and static equation of state of magnesium hydride have been studied theoretically at 0 K. However, it is important to go beyond the static calculations in order to assess the effect of temperature on its properties. In Chapter 5 we will present our work in which the contribution of lattice vibrations to the free energy of magnesium hydride at a series of finite temperatures between 0-1000 K have been evaluated via the quasiharmonic approximation (QHA). In this chapter we will begin with a short description of QHA and the small displacement method used for determining the above mentioned lattice contributions. QHA will be shown as a useful theoretical tool for calculating the thermodynamic quantities of MgH_2 even at temperatures greater than its melting point through the good agreement between our computational values of entropy and heat capacity with experimental results at various temperatures. From a comparison of the temperature variation of percentage change in cell volume with thaat in bulk modulus, application of temperatures slightly greater than 298K will be suggested as a potential approach for enhancing the volumetric hydrogen storage capacity of MgH_2 because of its better compressibility at these temperatures.

Chapter 6 Doped metal organic framework-5

Metal-organic frameworks (MOFs) are hydrid organic/inorganic materials built up of metal clusters joined by organic linkers. Their hydrogen storage applications have been extensively studied over the last few years. Many MOFs have been reported to exhibit significant storage capacity at 77 K which drastically decreases at room temperature. In *Chapter 6*, we will examine the feasibility of doping Na^+, Be^{2+}, Mg^{2+}, and Al^{3+} ions as opposed to Li^+ doping on benzene, the model for the 1,4-benzenedicarboxylic acid organic linker in MOF-5 by density functional theory (DFT) calculations. The performance of the DFT functionals: B3LYP, BHHLYP,

PBELYP, and PWLOC is tested by comparing first the hydrogen binding energies (ΔB.E.) of $M:1H_2$ models with MP2 binding energies and then of $Li^+C_6H_6:nH_2$ (n=1-3) systems with previously reported solid-states calculations. On the basis of ΔB.E. of $MC_6H_6:1H_2$ systems it will be illustrated that Li^+ and Mg^{2+} are the most suitable dopants for MOF-5 for improving its hydrogen adsorption thermodynamics. Further, multiple H_2 adsorption will be studied in Li^+ and Mg^{2+}-doped C_6H_6. It will be shown that H_2 molecules adsorb weakly over $Li^+C_6H_6$ with low ΔB.E.s. In contrast $Mg^{2+}C_6H_6$ is envisaged to adsorb n=4 H_2 molecules adsorbed with a ΔB.E. that lies within the range of 15-50 kJ/mol H_2 required for practical on-board hydrogen storage. Finally, assuming a formula unit of $Zn_4O(BDC)_3Mg_6(4H_2)_6$ a storage capacity of 5 wt.% H_2 is predicted. This suggests Mg^{2+} doping as a scheme for enhancing the efficiency of MOF-5 as a hydrogen storage material.

CHAPTER 1

Introduction

Begin at the ***beginning****, the King said,*
very gravely, and go on till
you come to the end: then stop.
-Lewis Caroll (Alice in Wonderland)

Sustainable development means meeting the needs of the present generation without compromising the ability of the future generations to meet their own needs. This tells us that while growth must not stop, we must remember that environmental restrictions exist because of the limited ability of the biosphere to deal with wastes from human activities. Thus a formidable task today is to responsibly develop and use technologies that will protect our environment. Fuel cell technology is an innovative solution, which addresses local, national, and global environmental needs. Hydrogen can be used as an efficient fuel for fuel cells. However, hydrogen storage is a materials science challenge which requires reduction of an enormous volume of hydrogen gas. A solution to this problem is allowing hydrogen to interact with solid-state materials. Designing such materials requires invention, experimentation, and developing an understanding of the fundamentals of hydrogen storage. The latter can be achieved by a synergistic approach involving both theory and computation, which can be used not only to understand experimental results but also to guide them.

In this chapter we begin by giving a brief introduction to fuel cells, its advantages and applications, and the use of hydrogen as the fuel in Section 1.1. The problems associated with gaseous and liquid hydrogen storage are defined in Section 1.2. In Section 1.3 we discuss the three mechanisms of solid-state hydrogen storage. In Sections 1.4 – 1.7 we provide a brief summary of experimental and theoretical studies of a few select hydrogen storage materials. We end the chapter by describing the motivation behind the research carried out herein and by presenting an outline of this thesis in Section 1.8.

1.1
Fuel cells

A *fuel cell* (FC) is an electrochemical energy conversion device which produces electricity, water and heat using fuel and oxygen in the air. The first demonstration of a FC was made in 1839 by William Grove, a British jurist and amateur scientist. Grove utilized four large cells containing hydrogen (H_2) and oxygen, to produce

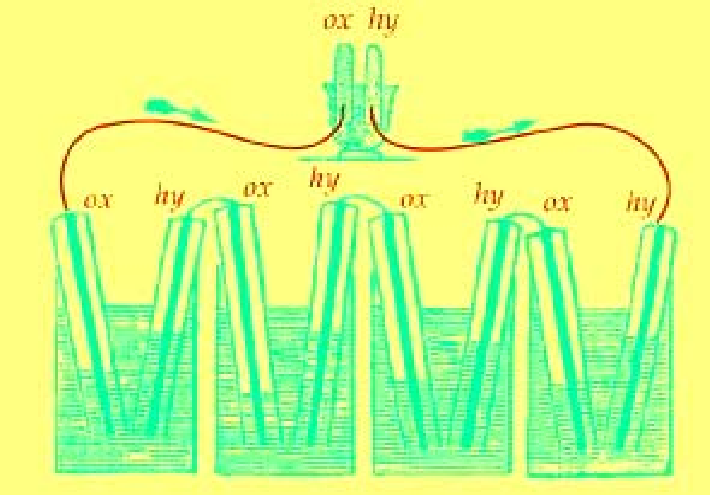

Figure 1.1 Schematic diagram of William Grove's experimental set up for demonstration of a fuel cell.

electric power which was then used to split the water in the small upper cells into H_2 and oxygen (see Fig. 1.1). However, the currents that are produced in such experiments are small because of the low contact area between the gas, electrode, and the electrolyte and due to the large distance between the electrodes which causes the electrolyte to resist the flow of electronic current.

To overcome these problems in FCs, the electrodes are usually made flat with a thin layer of electrolyte sandwiched between them as shown in Fig. 1.2. The reaction between H_2 and oxygen to generate electricity occurs as follows. First, H_2 flows into the anode side of the FC where it ionizes to release electrons and H^+ ions.

$$2H_2 \rightarrow 4H^+ + 4e^- \qquad (1.1.1)$$

This reaction releases energy. The hydrogen ions pass through the membrane and at

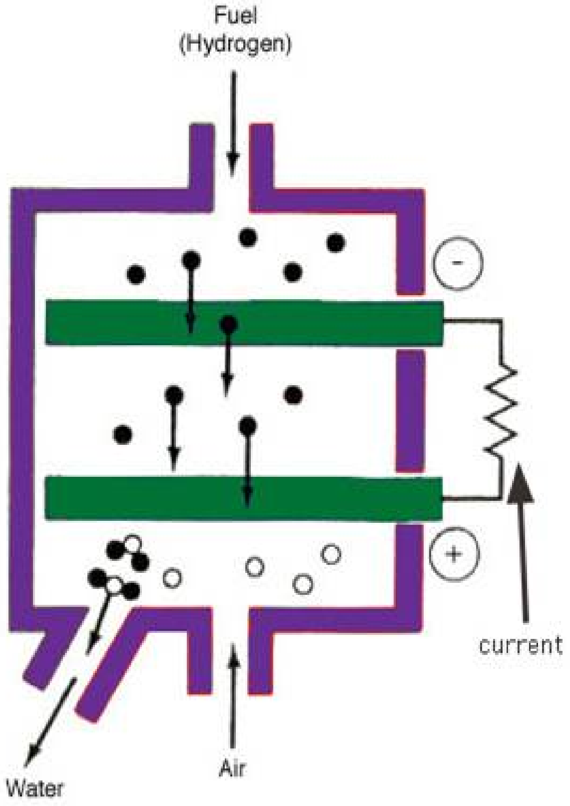

Figure 1.2 Basic structure of a fuel cell.

the cathode react with oxygen to form water.

$$O_2 + 4e^- + 4H^+ \rightarrow 2H_2O \qquad (1.1.2)$$

The electrons which cannot pass through the membrane flow from the anode to the cathode via an external circuit containing a motor, which consumes the power generated by the FC.

1.1.1
Advantages and applications

FCs, internal combustion engines (ICEs) and batteries all convert energy from one form to another. ICEs run on noisy, high temperature explosions resulting from the release of chemical energy by burning fuel with oxygen in the air. In comparison essentials of a FC are very simple with few moving parts which make it very quiet. ICEs first change chemical energy of a fuel into thermal energy and then into mechanical energy. The second step is limited by the Carnot Cycle. On the other hand, FCs and batteries directly convert chemical energy into electrochemical energy and thus are generally more efficient than ICEs. However, in a battery the reactants are stored internally and when used up the battery must either be replaced or recharged. In FCs the reactants are stored externally and once refuelled they immediately start functioning. A further advantage of using FCs is that when H_2 is used as the fuel the only by-product is water which is environmentally benign. When used in vehicles they would result in essentially zero harmful emissions.

FCs have a wide variety of applications which are classified as transportation, portable and stationary. Polymer electrolyte membrane fuel cells (PEMFCs) which are provide a continuous electrical energy supply from fuel at high levels of efficiency and power density at low operating temperature-pressure conditions are well suited for the transportation applications. PEMFCs can also be used for the purpose of portable applications such as laptops, mobile cell phones and even military communications equipment along with direct methanol fuel cells. The commercial stationary FC systems that are used for providing combined heat and power and for distributed power generation are based on molten carbonate fuel cells and solid-oxide fuel cells.

1.1.2
Hydrogen as a fuel

Over the years the world has moved from using fuels rich in carbon such as wood and coal to fuels such as oil and natural gas which are rich in H_2. Thus, a transition to a hydrogen based economy is easily foreseeable. H_2 with its high energy content, excellent electrochemical reactivity and zero emission characteristics is indeed the most attractive fuel for FCs. Although H_2 is the most abundant element in the universe, it does not occur naturally as a gaseous fuel and so for practical FC systems it has to be generated from either fossil fuels or water before it can be used as a fuel.

Steam reforming is the most practiced technology for large scale production of H_2. The basic reforming reactions for a hydrocarbon of the form C_nH_m are:

$$C_nH_m + nH_2O \rightarrow nCO + (m/2 + n)\ H_2 \qquad (1.1.3)$$

$$CO + H_2O \rightarrow CO_2 + H_2 \qquad (1.1.4)$$

These reactions are carried out normally over a supported nickel catalyst at temperatures typically above 500^oC. Alternatively H_2 can be produced via *partial oxidation* which requires still higher temperatures ($1200\text{-}1500^oC$) but can be used for handling much heavier petroleum fractions. The corresponding reaction for CH_4 is:

$$CH_4 + ½\ O_2 \rightarrow CO + H_2 \qquad (1.1.5)$$

H_2 generation can also be performed by *pyrolysis* or *thermal cracking* of hydrocarbons in absence of air. The advantage in this case is that the H_2 produced in very pure. A challenge however is to remove the carbon that is also formed. In *photoelectrolysis* the electricity generated from sunlight via photovoltaic cells is used to generate H_2 from water by electrolysis. Currently there is a great interest in manufacturing H_2 from *biological processes* such as photosynthesis and fermentation using bacteria. For transportation and low-power portable applications it is more convenient and efficient to have a local store of H_2 so that fitting a hydrogen-processing unit to produce H_2 on an as needed basis would not prove cost effective.

1.2
Problem of hydrogen storage

Difficulties in H_2 storage arise because of its large volume and extremely low energy density. At ambient temperature and atmospheric pressure, 1 kg of H_2 occupies a volume of only 11 m^3. This makes it intricate to store a large amount of H_2 in a small space, like the gas tank of a car. The energy density of gaseous H_2 can be improved by storing H_2 at higher pressures. A greater driving range can be achieved by increasing the amount and pressure of H_2 but at the expense of increased cost and valuable space within the vehicle. The other key challenges regarding gaseous H_2 storage that need to be addressed are refueling times, heat management requirements, volumetric capacity and energy density.

H_2 when stored as a liquid has an energy density (8.4 MJ/L) which is nearly twice that of H_2 gas compressed at 10,000 psi (4.4 MJ/L). However, liquefaction is an energy intensive process. Several stages are involved. The gas is first compressed and then cooled to about 78 K using liquid nitrogen. High pressure is then used to further cool the H_2 by expanding it through a turbine. Furthermore, liquid H_2 has a very low boiling point of -253^{o}C requiring excellent insulation techniques to avoid boil-off. Thus practical applications of H_2 storage by liquefaction are severely limited.

1.3
Solid-state hydrogen storage

Alternative to classical storage of H_2 in pressurized tanks and cryogenic vessels, H_2 can be stored in solid-state materials. This method offers (i) a H_2 storage route that is feasible at low-pressure and room-temperature, (ii) the best opportunities for meeting the requirements for on-board storage, and (iii) the highest packing density.

A potential H_2 storage material must exhibit reversible H_2 uptake/release. It should be lightweight with a high gravimetric H_2 storage capacity. It must have a low energy requirement and easily attainable operation temperature and pressure conditions for H_2 removal. It should also have a fast H_2 desorption/absorption kinetics. Finally the material must have a good stability and a low manufacture cost.

Presently there are three generic mechanisms known for storing H_2 in materials, namely, absorption, adsorption, and chemical reaction. In *absorptive hydrogen storage* H_2 is absorbed directly into the bulk of the material. For example, in simple crystalline metal hydrides atomic hydrogen gets incorporated in the interstitial sites of the lattice (see Fig. 1.3). *Adsorptive hydrogen storage* can take place via physisorption or chemisorption. Such sorptive processes typically occur on high-surface area porous materials. The *chemical reaction route for hydrogen storage* involves displacive chemical reactions, which may be reversible or irreversible, for both H_2 generation and H_2 storage. In the former case, H_2 generation and H_2 storage involve a simple reversal of the chemical reaction as a result of modest changes in the

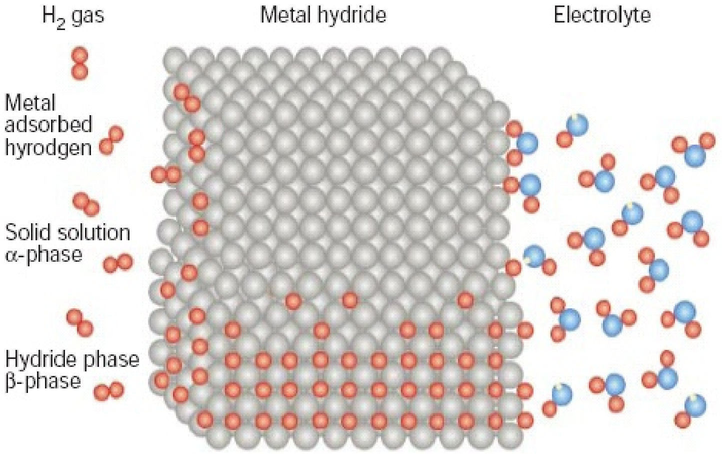

Figure 1.3 Schematic model of a metal structure with H atoms in the interstices between the metal atoms, and H_2 molecules at the surface. Hydrogen atoms are from the physisorbed H_2 molecules on the left-hand side and from the dissociation of water molecules on the right-hand side. (Source: Ref. 1)

temperature and pressure. For irreversible H_2 storage chemical reactions, the H_2 generation reaction is not reversible under modest temperature/pressure changes, so that storage requires larger temperature/pressure changes or alternative chemical reactions. In the following sections we discuss some of the H_2 storage materials of current interest.

1.4
Metal hydrides

Intensive research has been carried out over the years for light metals, transition metals and their alloys, which can combine with H_2 to produce stable metal hydrides, as H_2 storage materials. A critical discussion on the material challenges associated with hydrogen storage and in particular on the effect of mechanical milling and chemical additives in modifying metal hydride properties can be found in Ref. [2]. Recently in another review Shevlin and Guo [3] outline the fundamentals behind density functional theory (DFT) and expound upon its applications for calculating quantities such as hydrogen binding energies, enthalpies and free energies of formation, diffusion and reaction pathways, activation barriers, and transition states of metal hydride mixtures.

1.4.1
Intermetallic hydrides

Of special interest are the *intermetallic compounds* represented as AB_x formed by combining an element A usually a rare earth or alkaline earth metal that forms a stable hydride phase and an element B mostly a transition metal with weaker hydriding properties. The properties of several families of intermetallic compounds containing different amounts of A and B elements are summarized in Table 1.1. These intermetallic compounds exhibit a good volumetric H_2 storage capacity and undergo reversible hydrogenation/dehydrogenation at low temperatures with suitable thermodynamics and good kinetics. An interesting point about these systems is that their H_2 absorption and desorption can be tuned by alloying with correct

Table 1.1 Structure and hydrogen storage properties of intermetallic compounds reproduced from Ref. [4].

Type	*Metal*	*Hydrides*	*Mass%*	*Peq, T*
AB_5	$LaNi_5$	$LaNi_5H_6$	1.4	2 bar, 298 K
AB_3	$CaNi_3$	$CaNi_3H_{4.4}$	1.8	0.5 bar, 298 K
AB_2	ZrV_2	$ZrV_2H_{5.5}$	3.0	10-8 bar, 323K
AB	TiFe	$TiFeH_{1.8}$	1.9	5 bar, 303 K
A_2B	Mg_2Ni	Mg_2NiH_4	3.6	1 bar, 555 K

concentrations and types of elements. However, except for Mg_2NiH_4 the gravimetric H_2 storage capacity of these compounds is typically less than 3.0 wt.% H_2 as a result of which intermetallic hydrides are not recommended for on-board H_2 storage applications.

1.4.2
Magnesium hydride

Magnesium hydride (MgH_2) offers a high H_2 storage capacity of 7.6 wt.% H_2 coupled with the distinct advantages of low manufacture cost and good reversibility. It has the highest energy density 9 MJ/kg of all reversible hydrides applicable for H_2 storage. The drawbacks of MgH_2 are its: (a) high thermodynamic stability which results in a relatively high desorption enthalpy and a corresponding high desorption temperature of 300^oC at 1 bar H_2 [5, 6], (b) slow H_2 desorption kinetics [7], and (c) high reactivity towards air and oxygen. [8] Thus many efforts in recent years have focused on improving the dehydrogenation thermodynamics and kinetics of MgH_2.

A critical factor for H_2 absorption by metals is the metal surface, which activates dissociation of H_2 molecules and allows easy diffusion of H_2 into the bulk. Ball-milling creates an increased surface area, micro/nanostructures and defects on the surface and in the interior of the material. Huot et al. [9] found that ball milling resulted in a 10 fold increase in surface area, reduced activation energy barriers, and enhanced the H_2 desorption kinetics of MgH_2. In another approach, ball-milling is carried out under H_2 atmosphere. MgH_2 generated by this method exhibited better hydride formation kinetics. [10] Further effect of using different concentrations of carbon on hydrogen adsorption and desorption of mechanically milled MgH_2 was examined by Shang and Guo. [11] The results showed that graphite did not pose much influence on the desorption properties of MgH_2. But it did cause rapid hydrogen uptake in the re-hydrogenated sample. After dehydrogenation, 5.0 wt.% H_2 was reabsorbed within 30 min at 250^{o}C for the MgH_2 + 10G mixture prior-milled for 8 h as compared to 0.8 wt.% for the pure MgH_2 milled for 8 h. This was attributed to the interaction between crystalline graphite with H_2 disassociation close to the MgH_2 or Mg surface. Moreover, graphite also inhibited the formation of a new oxide layer on the surface of Mg particles.

Ródenas et al. [12] investigated hydrogen sorption properties of selected ball milled mixtures of MgH_2 with graphite as well as other carbon materials including activated carbon fibers, multi-walled carbon nanotubes (MWCNTS), carbon nanofibers (CNFs) and activated carbon fibers. It was found that introduction of the carbon materials decreases the decomposition temperature of MgH_2 with the best results being obtained with CNFs and MWCNTs. The decomposition kinetics of MgH_2 was shown to significantly improve specially with CNF additions with the improved kinetics being maintained even after several hydriding/dehydriding cycles. In a subsequent study [13] the authors illustrated with regards to MgH_2 decomposition that carbon-supported nickel catalysts exhibited superior performance than those just containing carbon and nickel physically mixed and, especially, than those containing only nickel.

The thermodynamic and kinetic limitations can also be overcome by adding small amounts of effective catalysts. Various transition metals (Pd, Ni, Ti, and V) [7, 14, 15] and metal oxides (V_2O_5, Cr_2O_3, Nb_2O_5) [8, 16-19] have been reported to play a catalytic role in hydriding/dehydriding reactions of MgH_2. Over the years theoretical studies have strived to explain the role of catalysts in hydrogen sorption in

MgH_2. First-principles calculations on the stability and electronic structure of MgH_2-M alloys where M = Al, Ti, Fe, Ni, Cu, or Nb suggested that the destabilization of MgH_2 by the alloying elements occurred due to the weakening of the Mg-H bond. [20-22] Li et al. [23] used DFT in conjunction with *ab initio* molecular dynamics simulations to provide a fundamental understanding of the effect of the Nb_2O_5 catalyst on the dehydrogenation mechanism of MgH_2. This was done by substituting Nb at the Mg site as well as by creating a Mg vacancy. It was found that although both methods resulted in lowering the H_2 desorption temperature, it was the substitution of Nb at the Mg site which was energetically more favorable than the formation of Mg vacancies. The catalytic role of transition metals Ti, V, Fe, and Ni in dehydrogenation of MgH_2 nanoclusters has also been investigated using DFT calculations. [24] It was shown that these transition metal atoms not only decreased desorption energies significantly but also continued to attract at least four hydrogen atoms even when the total hydrogen content of the cluster decreased. Recently Ramzan et al. [25] through *ab initio* molecular dynamics have demonstrated that nanoclusters increase the hydrogen diffusion rate and lower the desorption temperature of MgH_2. They also determined that it was the edge site Ni catalyst that resulted in fast diffusion of hydrogen in MgH_2 nanoclusters.

However, despite this extensive research Mg-based compounds displaying simultaneously the desired properties of low H_2 desorption temperature, fast kinetics and high gravimetric storage capacity are yet to be achieved.

1.4.3
Complex metal hydrides

Another class of hydrides to have received considerable attention is that of the *complex metal hydrides*. In these materials hydrogen reacts with Group I, II, and III light metals to form stable hydrides of the form $NaAlH_4$, Na_3AlH_6, $LiBH_4$, $LiNH_2$, and Li_2NH. In all of these systems the hydrogen atoms are covalently bonded to the central atoms in the "complex" anions.

$NaAlH_4$ is one of the widely studied complex aluminium hydride or alanate which releases H_2 via a two-step process:

$$3\ NaAlH_4 \rightarrow Na_3AlH_6 + 2\ Al + 3\ H_2 \tag{1.4.1}$$

$$Na_3AlH_6 \rightarrow 3\ NaH + Al + 3/2\ H_2 \tag{1.4.2}$$

that is associated with a H_2 storage capacity of about 5.5 wt.%. The operating temperatures for Reactions (1.4.1) and (1.4.2) are 185-230^{o}C and 260^{o}C, respectively. These reactions were characterized by high kinetic barriers and irreversibility due to which their practical applications seemed out of reach for many years. This scenario changed when Bogdanović and Schwickardi [26] demonstrated through their pioneering work that doping $NaAlH_4$ with selected Ti compounds kinetically enhanced their dehydrogenation reactions were as well as made the reactions reversible under moderate conditions in solid state. However, the H_2 capacities were found to quickly diminish upon cycling. Furthermore the H_2 adsorption/desorption kinetics of these materials was still inadequate to allow practical application for on-board H_2 storage. Subsequently it was found that charging the hydride with a catalyst by doping $NaAlH_4$ with suitable precursors through mechanical-milling was an effective means of bringing the kinetic and cycling properties closer to those desired in a practical H_2 storage medium. [27, 28]

Several theoretical studies which tried to decipher the role played by Ti in lowering the dehydrogenation temperature of $NaAlH_4$ gave conflicting results about the favourable site in the material for Ti substitution. [29-32] Araújo et al. [33] showed irrespective of the way the energetics was calculated the energy needed to remove hydrogen from Ti-substituted $NaAlH_4$ was significantly lower than for the pure alanate. Further, the authors demonstrated the important role played by Na vacancies during hydrogen desorption. [34] They found that the process of removing two hydrogen atoms from such a system was in fact exothermic with respect to formation of a H_2 molecule. A similar DFT study was performed to examine the influence of Ti and metal vacancies on the electronic structure, stability, and dehydrogenation of Na_3AlH_6. [35] Later Blomqvist et al. [36] performed a systematic study of the catalytic effect of other transition metal atoms on dehydrogenation of $NaAlH_4$ from which Cr and Fe were predicted to be even more effective than Ti.

A recent combined experimental and theoretical approach revealed that carbon nanostructures (fullerenes, nanotubes, and graphene) can be used as catalysts for hydrogen uptake and release in $NaAlH_4$. [37] The calculated electron affinities of these carbon substrates were found to be related to the hydrogen sorption mechanism. In addition, the curvature of the carbon nanostructure was suggested to play a role in the catalytic process with fullerene being a better catalyst than nanotubes.

Some of the other well studied alanates are $LiAlH_4$, $KAlH_4$ and $Mg(AlH_4)_2$. $LiAlH_4$ is an unstable hydride which decomposes easily but which cannot be rehydrogenated. [38] Its desorption reactions are the same as given in Equations (1.4.1) and (1.4.2) with Na replaced by Li. The first reaction take places at 187-218°C and the second dehydrogenation occurs at 228-282°C. [39] Together these lead to a H_2 release of 7.9 wt.%. The initial dehydrogenation of $KAlH_4$ to the hexahydride occurs at a much higher temperature (300°C) than the analogous process for $NaAlH_4$. Morioka et al. [40] suggested that as the formation enthalpies of KH and NaH were nearly equal while those of $KAlH_4$ and $NaAlH_4$ were quite different, it was the disparity in the thermodynamic stabilities of the parent alanates which was responsible for the differences in the dehydrogenation temperatures. Of the alkaline earth metal alanates, only $Mg(AlH_4)_2$ has an attractive gravimetric storage density which is above 7.0 wt.% H_2. It was shown by Fichtner et al. [41] that dehydrogenation of $Mg(AlH_4)_2$ at 163°C did not involve a hexahydride $[AlH_6]^{3-}$ intermediate and proceeded according to the following reaction:

$$Mg(AlH_4)_2 \rightarrow MgH_2 + 2\ Al + 3\ H_2 \qquad (1.3.3)$$

MgH_2 produced further dehydrogenates at 287°C to produce Mg. The thermodynamic properties of this material however appear to be unfavourable for reversible H_2 storage under practical conditions as the enthalpy seems to be close to 0 kJ/mol. [42]

An in case of $NaAlH_4$, Ti doping has been found to enhance the dehydrogenation kinetics of $LiAlH_4$ and $Mg(AlH_4)_2$. Balema et al. [43] found that on the addition of 3 mol% $TiCl_4$ the first dehydrogenation reaction of $LiAlH_4$ occurred at room temperature after five minutes of mechanical milling. Chen et al. [44] showed

Table 1.2 Hydrogen storage properties of pure and doped alanates

Reaction	*Ideal H_2 wt.%*	*Observed H_2 wt.%*		*Conditions Temp (^oC) (Pressure (MPa))*		*Ref*
		first dehyd	*rehyd*	*first dehyd*	*rehyd*	
$LiAlH_4 = LiH + Al + 3/2\ H_2$	8.0	8.0		201		45
$LiAlH_4 = 1/3\ Li_3AlH_6 + 2/3\ Al + H_2$	5.3	5.3		187-218		39,45
With Ti dopant	5.3	5.3		25		43
$Li_3AlH_6 = 3\ LiH + Al + 3/2\ H_2$	5.6	5.6		228-282		39,45
With Ti dopant	5.6	5.5		100-120		44
$NaAlH_4 = NaH + Al + 3/2\ H_2$	5.6	5.6	5.6	265	27 (17.5)	46,47
With Ti dopant	5.6	5.0	3.5-4.3	160	12-15 (11.5)	26-28
$KAlH_4 = KH + Al + 3/2\ H_2$	4.3	3.5	2.6-3.7	290	25-33 (0.10)	14
$Mg(AlH_4)_2 = MgH_2 + 2Al + 3\ H_2$	6.9	6.9		163-285		41
With Ti dopant	6.9	6.9		140-200		41

that doping intermediate hydride Li_3AlH_6 with 2 mol% $TiCl_3$ lowered its dehydrogenation temperature to as low as 100°C. Fitchner et al. [41] studied the kinetic effects of $Mg(AlH_4)_2$ doped with 2 mol% $TiCl_3$ and mechanically milled for up to 100 min and illustrated that the peak decomposition temperature was reduced in the presence of the titanium dopant. Table 1.2 summarizes the H_2 storage properties of both the pure and doped alanates.

Lithium-based complex hydrides first caught attention as possible hydrogen storage materials when Chen et al. [48] reported the reversibility of the interaction between Li_3N. This takes place by the following two-step reactions,

$$Li_3N + 2\ H_2 \leftrightarrow Li_2NH + LiH + H_2 \leftrightarrow LiNH_2 + 2\ LiH \qquad (1.4.3)$$

with an overall hydrogen storage capacity of 11.5 wt.%. The theoretically calculated formation enthalpies for the first and the second reaction are −162.0 kJ/mol and −40.9 kJ/mol, respectively. [49] The corresponding dehydrogenation temperatures of 423–473 K and 550 K however are high for practical applications. [50-52] For reducing this high desorption temperature requirement the bonding between Li^+ and $[NH_2]^-$ ions needs to be modified. One such approach involves alloy the binary hydride with some divalent alkaline earth metal such as Ca or Mg. Bhattacharya et al. [53] have carried out a comparative first-principles density functional study of the structural and thermodynamical properties of $Li_2Ca(NH)_2$ and $Li_2Mg(NH)_2$ with the parent imide. It was observed that the reaction enthalpy decreased from 108.8 kJ/mol in Li-imide to 102.6 kJ/mol and to 82.8 kJ/mol for Ca and Mg ternary imides, respectively. Based on first-principles molecular dynamics simulations Araújo et al. [54] recently attempted to answer questions regarding the temperature induced order-disorder phase transformation that occurs in Li_2NH, the hydrogenated phase of Li_3N, at about 385 K.

Reactions of $LiNH_2$ with other complex hydrides such as $LiBH_4$, $LiAlH_4$, and Li_3AlH_6 are also well known. More than 11 wt.% H_2 can be desorbed exothermically from a mixture of $2LiNH_2 + LiBH_4$ in the temperature range 250–350°C. [55, 56] Introducing nanosized Pd, Pt, Ni, and Co drastically decreased the dehydrogenation temperature to ~150 °C. [57, 58] However, further reductions are still needed to achieve onboard H_2 production.

The $Mg(NH_2)_2$–LiH systems have also attracted attention due to their reversible nature and suitable thermodynamic parameters. The dehydrogenation of $Mg(NH_2)_2$ and 2LiH takes place in the temperature range 150–250ºC, which gives 5.6 wt.% H_2 and a solid product $Li_2Mg(NH)_2$. But H_2 release at a reasonable rate requires temperatures above 150^{o}C even if the $Mg(NH_2)_2$/2LiH sample has been ball-milled intensively due to a possibly large activation energy barrier. Recently Wang et al. [59] found that a potassium-modified system in which LiH has been partially replaced with KH exhibited a set-off temperature of 80^{o}C, which is the operation temperature in PEMFCs, and also required a lowered H_2 desorption peak by 50°C as compared to the pristine sample. The DFT calculations in the same study suggested that substituting one Li atom by K in $Li_{32}Mg_{16}(NH)_{32}$ weakened the bonding which can facilitate atom reallocation across the amide/imide and/or imide/hydride phase boundaries, and mass transport through the imide phase, as a consequence of which much improved kinetics can be achieved.

For a more detailed review of the light metal hydrides and complex metal hydrides for H_2 storage the reader may refer to Refs. [60]-[63].

1.5
Clathrate hydrates

Clathrate hydrates are crystalline inclusion compounds consisting of hydrogen bonded water cages which can host a significant amount of guest molecules. It was long believed that each cage in a clathrate hydrate could accommodate-date only one guest molecule limiting the guest/water ratio R to ~0.167.

H_2 clathrate hydrates were first discovered in 2002 by Mao et al. [64] with the classical sII structure with a unit cell containing 136 H_2O molecules forming frame-works around eight hexakaidodecahedron ($5^{12}6^4$) and 16 pentagonal dodecahedron (5^{16}) cages. These were synthesized at high pressures of 220 ± 30 MPa and a temperature of 234 K with R = 0.45±0.05. This H_2/H_2O ratio was explained on the basis of multiple occupancy in which a cluster of two H_2 molecules were present in the small 5^{16} cages and four H_2 molecules in each of the large $5^{12}6^4$ cages. Figures 1.4 (a)-(c) show the structures of the sII H_2 clathrate hydrate and its two types of cages. Lokshin et al. [65] in contrast observed sII type H_2 clathrate hydrate having a small cage occupancy of 1 and a large cage occupancy of 4 at a pressure of 200 MPa. At atmospheric pressure the large cage occupancy changed to 2 with the small cages remaining singly occupied even when the temperature was increased.

There are three significant barriers to real applications of H_2 clathrate hydrates, namely, (a) slow kinetics associated with enclathration, (b) high pressures required for clathrate formation and stabilization, and (c) relatively low H_2 storage

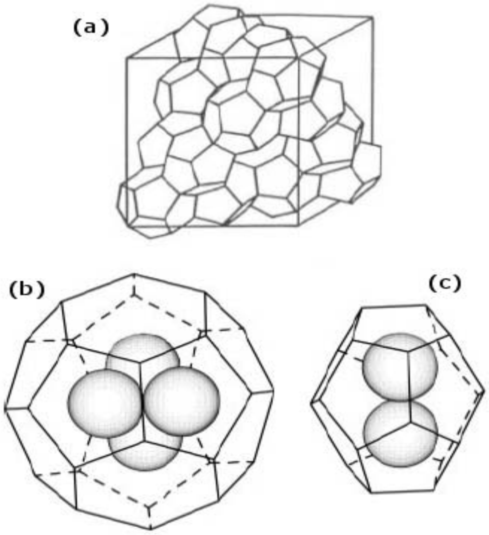

Figure 1.4 (a) Structure of sII clathrate hydrate built of large and small cages, (b) Large $5^{12}6^4$ cage containing a tetrahedral cluster of four H_2 molecules, and (c) Small 5^{16} cage occupied by two H_2 molecules. (Source: Ref. 64)

capacities. One of the ways of enhancing the kinetics of clathrate formation in the bulk is by increasing the surface-to-volume ratio of clathrate hydrates by using small crushed ice particles [66]. However, the use of crushed ice particles is inconvenient and, for multiple storage/release cycles, the material would revert to the bulk state upon melting. Methods such as efficient mechanical mixing or multiple temperature cycles can accelerate clathrate formation in laboratory but are likely to be unsuitable for on-board storage. Recently Su et al. [67] demonstrated a method using an ultralow-density, emulsion-templated polymerized high internal phase emulsion (polyHIPE) material as support for dramatically improving the kinetics and reusability for gas hydrates.

It has been shown that the pressure required to form a clathrate can be reduced significantly by introducing promoter molecules such as tetrahydrofuran into the larger $5^{12}6^4$ cage. [68] However this reduction in required pressure comes at the cost of reduced H_2 storage capacity, with potential H_2 storage volume taken up by the promoter molecule. Lee et al. [69] reported that H_2 storage capacities in THF-containing binary-clathrate hydrates can be increased to ~4 wt.% H_2 at modest pressures by tuning their composition to allow the H_2 guest molecules to enter both the large and the small cages, while retaining low-pressure stability.

The above experimental results have led to several attempts aiming to tune the hydrogen storage characteristics of clathrate hydrates. [70-73] In a new work [74] it was shown by means of pressure–volume–temperature measurements that the H_2–absorption rate of tetrahydrothiophene and furan hydrates was much greater than that of tetrahydrofuran hydrate. Their H_2 storage capacities however were determined to be coincident. An in-depth discussion on the structures, stabilities, occupancies, and dynamics of hydrogen clathrates and their analogues and an overview of the recent developments towards hydrogen storage is provided in Ref. [75].

The group of Chakravarty has been doing significant theoretical research on (a) the dynamical properties of water [76-78], (b) multi-time scale behaviour of hydrogen-bonded network in water [79, 60], and (c) structure, entropy, and mobility of network forming-ionic melts exhibiting water-like anomalies [81-86].

Studies regarding the stability and structural attributes of clusters of water have always been of great interest. [87-90] In the light of the importance of water-clathrate hydrates for hydrogen storage such studies have become even more important today. Ludwig and Appelhagen [91] performed *ab initio* calculations on clathrate-like water clusters with buckminsterfullerene as the guest species. In contrast Shameema and co-workers [92] have investigated the effect of spatial confinement on the properties of water and other isoelectronic molecules when encapsulated in a C_{60} fullerene cage. It is observed that depending on the molecular environment the larger clusters adopt seemingly different structures. [93, 94] Hydrogen bonding in protanted water molecules has been studied using an atoms-in-molecules (AIM) approach. [95] In a latest report, Parthasarthi et al. [96] have extended the application of this technique to examine the of linear water chains $(H_2O)_n$, n = 5-20 from *ab initio* DFT calculations. In another recent work, Kirov and co-authors [97] have presented a new discrete model, relying on the screening of the energy of the local network based on the concept of ‘strong’/‘weak’ nearest neighbor interactions according to their (*trans*/*cis*) orientation and the connectivity of the respective pairs to neighbours, to identify the most stable networks in polyhedral water clusters.

Theoretical studies have also tried to answer several questions regarding the thermodynamic stability of clathrate hydrates as a function of cage occupancy, the bonding in the H_2 molecules, and their clustering inside the cages. A statistical mechanical method in conjunction with first-principles calculations showed that the stability of the clathrate was mainly due to the dispersive interactions between H_2 molecules and the water forming the cages. [98] Calculations at the experimental conditions of 200 MPa and 250 K confirmed the picture of multiple occupancy in the clathrate cages. Sluiter et al. [99] showed through an electronic density functional study that the enclathration of H_2 molecules in clathrates is based on physisorption with energy of the order of 20-25 meV/H_2. As the H_2 interaction with the cage wall was much stronger than that with other H_2 molecules it was suggested that the H_2 molecules in a cage bind individually to the cage walls and that the H_2-H_2 interaction played a role in for crowding only, dispelling the picture of H_2 clusters in the cages. However, in this study only the quantum effects of rotational movement were considered while those of translational motion were neglected. Thus here the zero-point vibrations were accounted partially.

Inerbaev et al. [100] extended this work within the lattice dynamics approach in the quasiharmonic approximation (QHA) to examine the effect of cage occupancy and temperature on the structural, dynamic and thermodynamic properties of sII H_2 clathrate hydrate taking into account all types of molecular vibrations. Calculations at the experimentally measured cage occupancy and temperature agreed well with the equilibrium pressure of the H_2 clathrate hydrate reported by Lokshin et al. [65] as opposed to that by Mao et al. [64]. It was also shown that at temperatures above approximately 125 K and for large cage occupancies of 3 H_2 or less, the guest molecules did not affect the host lattice. Furthermore, the quantum zero-point vibrations were found to be of fundamental importance for calculating the thermodynamic properties of the H_2 clathrate hydrates.

Narrowing down the range of possible promoter compounds that can reduce the high pressure requirement of the clathrates requires an understanding of their characteristics. Such an insight can be gained in terms of the interaction of promoter molecules with both water and H_2 and by determining the mechanisms of the processes that lead to promoted clathrate formation and stabilization, through theoretical studies. Thus, in the future computational modelling will play an important role in the development of promoted H_2 containing clathrate hydrates.

1.6
Metal-organic frameworks

Metal-organic frameworks (MOFs) are hybrid inorganic/organic crystalline materials in which metal ion clusters are linked by organic ligands to form extended frameworks that are highly stable as well as microporous. [101] With a number of organic ligands and metal ions that are available for use in the synthesis scheme a variety of networks with desired pore dimensions and metal centers can be designed.

In a path breaking work in 2003 Rosi et al. [102] reported favourable H_2 sorption properties of up to ~4.5wt.% H_2 at 78 K for MOF-5. It can be seen from Fig. 1.5 (a) that MOF-5 is built from inorganic $[OZn_4]^{6+}$ groups joined by an octahedral array of $[O_2C\text{-}C_6H_4\text{-}CO_2]^{2-}$ (1,4-benzenedicarboxylate or BDC) groups. The H_2 storage capacity however reduced to 1.0 wt.% H_2 at room temperature and 20 bar pressure. The corresponding H_2 adsorption isotherms of MOF-5 at 78 K and 298 K are displayed in Figs. 1.5 (b) and (c). MOF-177 [103, 104], IRMOF-20 [105, 106], MIL-101 [106, 107] and $[Cu(L^2)(H_2O)_2]$ (L^2=terphenyl-3,3'',5,5'-tetracarboxylate) [108] have also been reported to show high H_2 uptake in the range of 5.0-7.5 wt.% H_2 at 77 K and moderate pressure. But at 298 K their maximum H_2 uptake falls below 1.5 wt.% H_2.

H_2 adsorption in MOFs can be improved by using coordinately unsaturated ions such as Mg^{2+} [109], Ni^{2+} [110] and Zn^{2+} [111] in the metal oxide core. The coordinative unsaturation basically brings about stronger physisorption with a concurrent decrease in the density of the framework. Another approach that is currently being considered for enhancing H_2 storage of these materials is using Li for doping MOFs. Blomqvist et al. have explored Li doping onto 1,4-

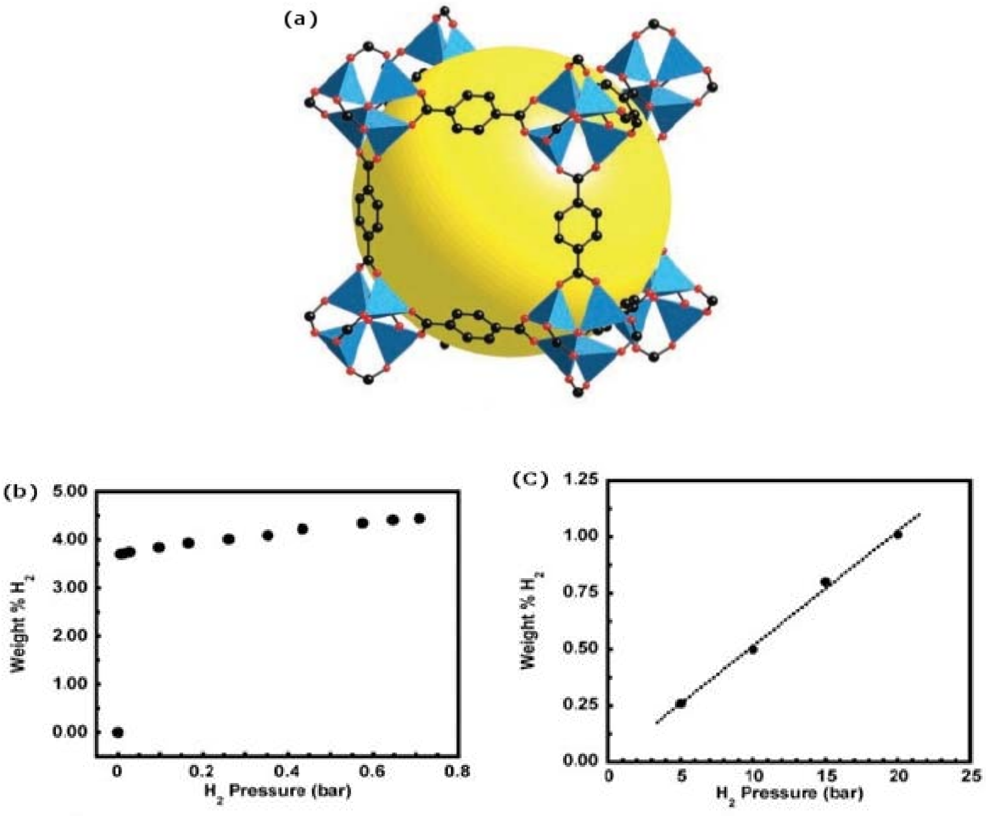

Figure 1.5 (a) Single-crystal x-ray structure of MOF-5 illustrated for a single unit cell. On each of the corners is an oxygen-centered Zn_4 cluster $[OZn_4(CO_2)_6]$. These are bridges by six carboxylates of the 1,4-benzene dicarboxylate linkers.; Hydrogen gas adsorption isotherms of MOF-5 at (b) 78 K and (c) 298 K. (Source: Ref. 102)

benzenedicarboxylate (BDC) linkers in MOF-5. [112] They showed by means of first-principles calculations that two Li atoms were strongly adsorbed on the surfaces of the BDC six-carbon rings, one on each side, carrying a charge of +0.9e per Li. Each Li was found to be able to cluster three H_2 molecules around itself with a binding energy (12.0 kJ/mol H_2) more than two times larger than the binding energy (5 kJ/mol H_2) for pure BDC [113]. Dalach et al. [114] have applied density functional theory (DFT) to selected clusters representative of two MOFs: $Zn_2[NDC]_2(BIPY)$ and $Zn_2(BPDC)_2(DPNI)$ where BIPY=4,4'-bipyridine, NDC=2,6-naphthalenedicarboxylic acid, BPDC=biphenyl-4,4'-dicarboxylate, and DPNI=N,N'-di(4-pyridyl)-1,4,58-naphthalenetetracarboxydiimide, to examine the effect of doping electrons through Li into their structures. The DFT studies confirmed an enhancement of H_2 adsorption energies both on the organic linkers and the metal oxide cornerposts when Li was doped into the structure. In contrast to previous model assumptions the authors found that Li associated more strongly to the metal oxide cornerposts than to the aromatic rings of the organic linkers.

Recently, Kolmann et al. [115] performed a systematic study in order to validate the use of DFT for Li-doped MOFs. In their work they used a Li^+-benzene complex as a model for Li-doped MOF-5. They considered the following DFT functionals: BMK [116], B3LYP [117, 118] and M05-2X [119] whose performance was compared with MP2 and CCSD(T). M05-2X was found to be the best DFT method chosen as it successfully reproduced the MP2 and CCSD(T) H_2 binding energies to Li^+-doped benzene. It was further suggested that the interaction between H_2 and Li was primarily a local interaction which depends little on the nature of the extended structure of the material, implying that model compounds can be used to describe these systems.

In all the above mentioned DFT studies attempts have been made to model the interaction of H_2 with doped MOFs but questions regarding the kinetics and enthalpy of H_2 adsorption need to be answered. The experimental feasibility of manufacturing these Li-doped MOFs for H_2 storage also requires to be tested.

For a good account on MOFs and on the various other techniques besides light metal atom doping aimed at improving H_2 uptake in these materials such as optimization of pore size, impregnation of another adsorbate surface within large-pore MOFs, catenation framework, open metal sites, and using functionalized linkers, the reader may see the review by Roswell and Yaghi [120].

1.7
Other hydrogen storage materials

Besides the materials discussed above, there are other approaches which also deserve a special mention.

1.7.1

Zeolites

Zeolites are classic examples of microporous materials. These are crystalline inorganic polymers based on a three-dimensional arrangement of SiO_4 and AlO_4 tetrahedra connected through their oxygen atoms to form large negatively-charged lattices which are balanced by extra-framework alkali and/or alkali earth cations. Some of the commonly known zeolites are silicalite-1, ZSM-5, zeolite Beta (BEA) and zeolites X, Y, and A. It has been observed that incorporating transition metal ions into their frameworks can acidity. Thus, several quantum chemical calculations have focussed on examining the structural properties, adsorption properties and proton affinity of zeolites and on deducing the effect of transition metal ions. [121-127]

Other studies have concentrated on determining the sites that will prefer to incorporate the transition metal ion. [128-132] Figure 1.6 displays the unit cell of

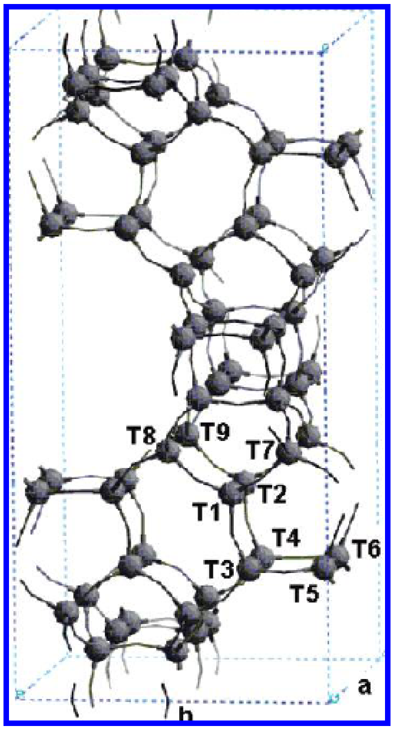

Figure 1.6 Crystallographically defined 9 T sites of BEA zeolite. The grey spheres represent the Si sites. (Source: Ref. 128)

BEA zeolite and the nine T sites where Sn and Ti substitution can possibly take place. Zeolites with their well–organised and regular system of pores and cavities also represent almost ideal matrices for hosting nanosized particles. The effects of pore structure of zeolites, temperature and pressure on the hydrogen adsorption of several zeolites and ion-exchanged zeolites have been explored with respect to their application for hydrogen storage. [133-142] At 77 K, the temperature at which most measurements are taken, zeolites exhibit poor maximum adsorption capacities in the 1–2 wt% region at pressures of 1 bar. [143]

Template synthesis is a promising technology to prepare novel porous carbon materials with large surface area and relatively uniform pores. Among the possible templates, zeolites can be used to obtain ordered carbon materials with very high microporous volumes due to a very well defined and narrow pore size distribution (PSD). Surprisingly though zeolites themselves face drawbacks when attempting to reach the Department of Energy targets, current studies have demonstrated that zeolite based template carbons have strong potential for H_2 storage. [144-151]

1.7.2
Graphene

Carbon nanostructures such as fullerenes and nanotubes are promising candidates for hydrogen storage. But their large-scale production and high cost serve as severe limitations. Lately graphene, a two-dimensional flat monolayer of carbon atoms packed into a honeycomb lattice, has come into prominence because of the developments in its experimental fabrication techniques. Due to its fascinating physics for fundamental studies and its potential applications for the next-generation electronic devices and H_2 storage materials graphene attracts a lot of attention.

Lu et al. [152] have recently investigated in detail the electronic structure of tetracyanoethylene (TCNE) on graphene using the first-principles method based on DFT. It was demonstrated that the electronic structure of graphene can be controlled over a wider range by organic molecules, and that it is possible to build graphene-based electronic devices by modifying the graphene with patterned organic molecules, without the need for cutting or etching graphene. Another route that has been recently suggested for tuning the electronic structure involves growing graphene on a substrate. [153, 154]

In many computations polycyclic aromatic hydrocarbons (PAHs) are chosen to model graphene. Heine et al. [155] calculated the physisorption energy of H_2 as a function of the PAH size and the adsorption site. The adsorption energies were found to be between 4-7 kJ/mol and these results were then extrapolated to graphene layers. A similar *ab initio* study was also carried out by the authors for modelling N_2 adsorption on grapehene platelets which revealed that the trends for H_2 and N_2 adsorption on PAHs and graphene were same but with N_2 binding twice as strongly as H_2. [156] At room temperature quantum effects are significant and need to be accounted for. This nontrivial task was performed by Patchkovskii and co-workers [157] who found that H_2 storage in graphene depended on the interlayer distance. For distances less than 5 Å the H_2-graphene interaction potential was repulsive which prevented the penetration of H_2 in between the graphite layers. The storage capacity peaked at an interlayer distance of 6 Å and then reduced continuously with increasing distance. For the limit of a single graphene sheet an insignificant uptake of H_2 on the layer surface was predicted. It was concluded that with an appropriate interlayer the H_2 storage in graphene could be tuned to reach reasonable values. Introduction of spacers was suggested as a possible route for achieving this such uniform interlayer distances. In an interesting study C_{60}-intercalated graphite (CIG) was simulated. [158] Between 50-300 K temperatures CIG was found to have double the interaction free energy with H_2 than the empty structure. Compared to Li-doped carbon nanotubes and Li-doped graphite, CIG was able to achieve a high H_2 storage capacity at low temperatures.

More recently a combined experimental and theoretical investigation has been performed on the H_2 and CO_2 uptake of graphene. [159] Graphene samples with different surface areas prepared by exfoliation of graphitic oxide or conversion of nanodiamond showed significant absorption of H_2 and CO_2. The maximum H_2 uptake was found to be 3.1 wt.% at 100 atm and 298 K. The theoretical calculations yielded a 7.7 wt.% of H_2 uptake by a single-layer graphene both in the parallel and perpendicular orientations.

Current advancements in experiments have now permitted production of finite sized graphene layers or graphene nanoribbons (GNRs) with varying widths. Depending up on where the layers are terminated one can have two different edge geometries, namely, zigzag and armchair edges which vary largely in their electronic properties. Their electronic and magnetic properties have only recently been explored using a many-body description. In this regard the detailed configuration interaction and density functional studies of undoped and doped GNRs done by Pati and co-workers are noteworthy. [160-162] In another fresh study Lu et al. have investigated effects of hydrogen passivation of edges of armchair GNRs on their electronic properties using first-principles method. [163]

1.8

Motivation and outline of the thesis

Presently there are a variety of solid-state H_2 storage materials being investigated, but none of these systems satisfy all the requirements for practical on-board storage of hydrogen. In view of this fact the current need, therefore, today is to bring about breakthroughs in the existing technologies as well as develop new H_2 storage materials. Experimentally this is a long drawn process requiring significant human and financial resources. Computational materials science in comparison is a fast and cost effective strategy for evaluating novel materials. In addition theory and simulations can be used for supporting experimental results. Thus, the main motivation behind this thesis is to use a computational approach to model different classes of H_2 storage materials and to understand the H_2 desorption processes associated with them.

The intensive studies carried out over the past decade reveal that MgH_2, complex metal hydrides, and MOFs have tremendous promise for the purpose of H_2 storage. The need for enhancing their H_2 storage properties, which calls for further research, inspired us to specifically study these materials in the present thesis. To this end, herein we have performed DFT based calculations to study theoretically the ground state structure, electronic structure, chemical bonding, dehydrogenation thermodynamics, H_2 desorption kinetics, and effect of (a) high pressure phases, (b) addition of dopants, and (iii) inclusion of lattice vibrations at finite temperatures.

The outline of this thesis is as follows. Chapter 2 provides the theoretical background of the computational techniques employed in this work. In the succeeding chapters 3-6, results from our theoretical studies are presented. Specifically, Chapter 3 deals with a detailed study of chemical bonding in α- and β-$LiAlH_4$ and -$LiBH_4$ and in pure and Al- and Si-doped α-, γ-, and β-MgH_2. In Chapter 4 the thermodynamics and kinetics associated with H_2 removal from the same materials are discussed. The effect of temperature on the thermodynamical properties of MgH_2 is summarized in Chapter 5. Chapter 6 is an indicator study in which H_2 binding energies of light metal ion doped MOF-5 has been evaluated by using molecular complexes of the organic linker, that is, benzene ring with metal ions and different number of H_2 molecules as model systems. Finally in Chapter 7 we summarize the important results of this thesis and provide an outlook into the future scope of this work.

References

1. L. Schlapbach and A. Züttel, *Nature* **2001**, *414*, 353.
2. Z. X. Guo, C. Shang, and K. F. Aguey-Zinsou, *J. Eur. Ceramic Soc.* **2008**, *28*, 1467.
3. S. A. Shevlin and Z. X. Guo, *Chem. Soc. Rev.* **2009**, *38*, 211.
4. P. Chen and M. Zhu, *Mater. Today* **2008**, *11*, 36.
5. W. Grochala and P.P. Edwards, *Chem. Rev.* **2004**, *104*, 1283.
6. H. Imamura, K. Masanari, M. Kusuhara, H. Katsumoto, T. Sumi, and Y. Sakata, *J. Alloys Compd.* **2005**, 386, 211.
7. A. Zaluska, L. Zaluski, and J. O. Ström-Oslen, *J. Alloys Compd.* **1999**, *288*, 217.
8. G. Barkhordarian, T. Klassen, and R. Bormann, *J. Alloys Compd.* **2004**, *364*, 242.
9. J. Huot, G. Liang, S. Boily, A. V. Neste, and R. Schulz, *J. Alloys Compd.* **1999**, *293-295*, 495.
10. J. Huot, E. Akiba, and T. Takada, *J. Alloys Compd.* **1995**, *231*, 815.

11. C. X. Shang and Z. X. Guo, *J. Power Sources* **2004**, *129*, 73.
12. M. A. Ródenas, Z. X. Guo, K. F. Aguey-Zinsou, D. Cazorla-Amorós, and A. Linares-Solano, *Carbon* **2008**, *46*, 126.
13. M. A. Ródenas, K. F. Aguey-Zinsou, D. Cazorla-Amorós, A. Linares-Solano, and Z. X. Guo*, J. Phys. Chem. C* **2008**, *112*, 5984.
14. C. Iwakura, S. Nohara, S. G. Zhang, and H. Inoue, *J. Alloys Compd.* **1999**, *285*, 246.
15. G. Liang, J. Huot, S. Boily, A. V. Neste, and R. Schultz, *J. Alloys Compd.* **1999**, *292*, 247.
16. K. S. Jung, E. Y. Lee, and K. S. Lee, *J. Alloys Compd.* **2005**, *421*, 179.
17. M. Y. Song, J-L. Bobet, and B. Darriet, *J. Alloys Compd.* **2002**, *340*, 256.
18. Z. Dehouche, T. Klassen, W. Oelerich, J. Goyette, T. K. Bose, and R. Schultz, *J. Alloys Compd.* **2002**, 347, 319.
19. G. Barkhordarian, T. Klassen, and R. Bormann, *J. Alloys Compd.* **2006**, *407*, 249.
20. Y. Song, Z. X. Guo, and R. Yang, *Mater. Sci. Eng., A* **2004**, *365*, 73.
21. C. X. Shang, M. Bououdina, Y. Song, and Z. X. Guo, *Int. J. Hydrogen Energy* **2004**, *29*, 73.
22. Y. Song, Z. X. Guo, and R.Yang, *Phys. Rev. B* **2004**, *69*, 094205.
23. S. Li, P. Jena, and R. Ahuja, *Phys. Rev. B* **2006**, *74*, 132106.
24. P. Larsson, C. M. Araújo, J. A. Larsson, P. Jena, and R. Ahuja, *Proc. Natl. Acad. Sci. U.S.A.* **2008**, *105*, 8227.
25. M. Ramzan, T. Hussain, and R. Ahuja, *Appl. Phys. Lett.* **2009**, *94*, 221910.
26. B. Bogdanović and M. Schwickardi, *J. Alloys Compd.* **1997**, *253-254*, 1.
27. C. M. Jensen, R. Zidan, N. Mariels, A. Hee, and C. Hagen, *Int. J. Hydrogen Energy* **1999**, *23*, 461.
28. R. A. Zidan S. Takara, A. G. Hee, and C. M. Jensen, *J. Alloys Compd.* **1999**, *285*, 119.
29. J. Íñiguez and T. Yildirim, *Appl. Phys. Lett.* **2005**, *86*, 103109.
30. J. Íñiguez, T. Yildirim, T. J. Udovic, M. Sulic, and C. M. Jensen, *Phys. Rev. B* **2004**, *70*, 060101.

31. O. M. Løvvik and S. M. Opalka, *Phys. Rev. B* **2005**, *71*, 054103.
32. O. M. Løvvik and S. M. Opalka, *Appl. Phys. Lett.* **2006**, *88*, 161917.
33. C. M. Araújo, R. Ahuja, J. M. O. Guillén, and P. Jena, *Appl. Phys. Lett.* **2005**, *86*, 251913.
34. C. M. Araújo, S. Li, R. Ahuja, and P. Jena, *Phys. Rev. B* **2005**, *72*, 165101.
35. S. Li, P. Jena, and R. Ahuja, *Phys. Rev. B* **2006**, *73*, 214107.
36. A. Blomqvist, C. M. Araújo, P. Jena, and R. Ahuja, *Appl. Phys. Lett.* **2007**, *90*, 141904.
37. P. A. Beresth, A. G. Harter, R. Zidan, A. Blomqvist, C. M. C. M. Araújo, R. H. Scheicher, R. Ahuja, and P. Jena, *Nano Lett.* **2009**, *9*, 1501.
38. L. Zaluski, A. Zaluska, and J. O. Ström-Oslen, *J. Alloys Compd.* **1999**, *290*, 71.
39. J. Block and A. P. Gray, *Inorg. Chem.* **1965**, *4*, 304.
40. H. Morioka, K. Kakizaki, S. Chung, and A. Yamada, *J. Alloys Compd.* **2003**, *353,* 318.
41. M. Fitchner, O. Fuhr, and O. Kircher, *J. Alloys Compd.* **2003**, *356-357*, 418.
42. P. Claudy, B. Bonnetot, and J. M. Létoffé, *J. Therm. Anal. Calorimetry* **1979**, *15*, 119.
43. V. P. Balema, K. W. Dennis, and V. K. Pecharsky, *Chem. Commun.* **2000**, 1665.
44. J. Chen, N. Kuriyama, Q. Xu, H. T. Takeshita, and T. Sakai, *J. Phys. Chem. B* **2001**, *105*, 11214.
45. W. E. Garner and E. W. Haycock, *Proc. R. Soc. (London)* **1952**, *A211*, 335.
46. P. Claudy, B. Bonnetot, G. Chahine, and J. M. Létoffé, *Thermochim. Acta* **1980**, *38*, 75.
47. J.-P. Bastide, B. Bonnetot, J. M. Létoffé, and P. Claudy, *Mater. Res. Bull.* **1981**, *16*, 91.
48. P. Chen, Z. Xiong, J. Luo, J. Lin, and K. L. Tan, *Nature* **2002**, *420*, 302.
49. Y. Song and Z. X. Guo, *Phys. Rev. B* **2006**, *74*, 195120.
50. S. Orimo, Y. Nakamori, G. Kitahara, K. Miwa, N. Ohba, T. Noritake, and S. Towata, *Appl. Phys. A* **2004**, *79*, 1765.

51. Y. Nakamori and S. Orimo, *J. Alloys Compd.* **2004**, *370*, 271.
52. Y. Nakamori and S. Orimo, *Mater. Sci. Eng., B* **2004**, *108*, 48.
53. S. Bhattacharya, G. Wu, C. Ping, Y. P. Feng, and G. P. Das, *J. Phys. Chem. B* **2008**, *112*, 11381.
54. C. M. Araújo, A. Blomqvist, R. H. Scheicher, P. Chen, and R. Ahuja, *Phys. Rev. B* **2009**, *79*, 172101.
55. F. E. Pinkerton, G. E. Meisner, M. S. Meyer, M. P. Balogh, and M. B. Kundrat, *J. Phys. Chem. B* **2005**, *109*, 6.
56. M. Aoki, K. Miwa, T. Noritake, G. Kitahara, Y. Nakamori, S. Orimo, and S. Towata, *Appl. Phys. A Mater. Sci. Proc.* **2005**, *80*, 1409.
57. F. E. Pinkerton, M. S. Meyer, G. E. Meisner, and M. P. Balogh, *J. Alloys Compd.* **2007**, *433*, 282.
58. W. S. Tang, G. Wu, T. Liu, A. T. S. Wee, C. K. Yong, Z. Xiong, A. T. S. Hor, and P. Chen, *Dalton Trans.* **2008**, *18*, 2395.
59. J. Wang, T. Liu, G. Wu, W. Li, Y. Liu, C. M. Araújo, R. H. Scheicher, A. Blomqvist, R. Ahuja, Z. Xiong, P. Yang. M. Gao, H. Pan, and P. Chen, *Angew. Chem. Int. Ed.* **2009**, *48*, 5828.
60. F. Schüth, B. Bogdanović, and M. Felferhoff, *Chem. Comm.* **2004**, 2249-2258.
61. B. Sakintuna, F. Lamary-Darkrim, and M. Hirscher, *Int. J. Hydrogen Energy* **2007**, *32*, 1121.
62. S. Orimo, Y. Nakamori, J. R. Eliseo, A. Züttel, and C. M. Jensen, *Chem. Rev.* **2007**, *107*, 4111.
63. P. Chen and M. Zhu, *Mater. Today* **2008**, *11*, 36.
64. W. L. Mao, Ho-kwang Mao, A. F. Goncharov, V. V. Struzhkin, Q. Guao, J. Hu, J. Shu, R. J. Hemley, M. Somayazulu, and Y. Zhao, *Science* **2002**, *297*, 2247.
65. K. A. Lokshin, Y. Zhao, D. He, W. L Mao, H. Mao, R. J. Hemley, M. V. Lobanov, and M. Greenblatt, *Phys. Rev. Lett.* **2004**, *93*. 125503.
66. T. A. Strobel, C. J. Taylor, K. C. Hester, S. F. Dec, C. A. Koh, K. T. Miller, and E. D. Sloan, *J. Phys. Chem. B* **2006**, *110*, 17121.
67. F. Su, C. L. Bray, and A. I. Cooper, *Adv. Mater.* **2008**, *20*, 2663.

68. L. J. Florusse, C. J. Peters, J. Schoonman, K. C. Hester, C. A. Koh, S. F. Dec, K. N. Marsh, and E. D. Sloan, *Science* **2004**, *306*, 469.
69. Jong-won Lee, D. Y. Kim, J. Park, Yu-Taek Seo, H. Zeng, I. L. Moudrakovski, C. I. Ratcliffe, and J. A. Ripmeester, *Nature* **2005**, *434*, 743.
70. Do-Youn Kim, Y. Park, and H. Lee, *Cat. Today* **2007**, *120,* 257.
71. T. A. Strobel, C. A. Koh, and E. D. Sloan, *Fluid Phase Equilib.* **2007**, *261*, 382.
72. S. Hashimoto, T. Sugahara, M. Moritoki, H. Sato, and K. Ohgaki, *Chem. Eng. Sci.* **2008**, *63*, 1092.
73. Ji-Ho Yoon, J. Han, J. Park, S. Choi, Sun-Hwa Yeon, and H. Lee *J. Phys. Chem. Solids* **2008**, *69*, 1432.
74. T. Tsuda, K. Ogata, S. Hashimoto, T. Sugahara, M. Moritoki, and K. Ohgaki, *Chem. Eng. Sci.* **2009**, *64*, 4150.
75. T. A. Strobel, K. C. Hester, C. A. Koh, A. K. Sum, and E. D. Sloan Jr., *Chem. Phys. Lett.* **2009** (in press).
76. A. Mudi, R. Ramaswamy, and C. Chakravarty, *Chem. Phys. Lett.* **2003**, *376*, 683.
77. A. Mudi and C. Chakravarty, *Mol. Phys.* **2004**, *102*, 681.
78. A. Mudi, C. Chakravarty, and R. Ramaswamy, *J. Chem. Phys.* **2005**, *122*, 104507-1.
79. A. Mudi and C. Chakravarty, *J. Phys. Chem. B* **2004**, *108*, 19607.
80. A. Mudi, C. Chakravarty, and E. Milotti, *J. Chem. Phys.* **2006**, *125*, 074508.
81. R. Sharma, A. Mudi, and C. Chakravarty, *J. Chem. Phys.* **2006**, *125*, 044705.
82. R. Sharma, S. N. Chakraborty, and C. Chakravarty, *J. Chem. Phys.* **2006**, *125*, 204501.
83. M. Agarwal, R. Sharma, and C. Chakravarty, *J. Chem. Phys.* **2007**, *127*, 164502.
84. M. Agarwal and C. Chakravarty, *J. Phys. Chem. B* **2007**, 13294.
85. R. Sharma, M. Agarwal, and C. Chakrvarty, *Mol. Phys.* **2008**, *106*, 1925.
86. M. Agarwal and C. Chakravarty, *Phys. Rev. E* **2009**, *79*, 030202(R).

87. S. Maheshwary, N. Patel, N. Sathyamurthy, A. D. Kulkarni, and S. R. Gadre, *J. Phys. Chem. A* **2001**, *105*, 10525.
88. J. D. Cruzan, L. B. Braly, K. Liu, M. G. Brown, J. G. Loeser, and R. J. Saykally, *Science* **1996**, *271*, 59.
89. J. D. Cruzan, L. B. Braly, K. Liu, M. G. Brown, J. G. Loeser, and R. J. Saykally, *J. Phys. Chem. A* **1997**, *101*, 9022.
90. J. Kim and K. S. Kim, *J. Chem. Phys.* **1998**, *109*, 5886.
91. R. Ludwig, and A. Appelhagen, *Angew. Chem., Int. Ed.* **2005**, *44*, 811.
92. O. Shameema, C. N. Ramachandran, and N. Sathyamurthy, *J. Phys. Chem. A* **2006**, *110*, 2.
93. S. K. Ghosh and P. K. Bharadwaj, *Angew. Chem., Int. Ed.* **2004**, *116*, 4490.
94. S. K. Ghosh and P. K. Bharadwaj, *Inorg. Chem.* **2004**, *43*, 3771.
95. R. Parthasarathi, V. Subramanian, and N. Sathyamurthy, *J. Phys. Chem. A Lett.* **2007**, *111*, 13287.
96. R. Parthasarathi, M. Elango, V. Subramanian, and N. Sathyamurthy, *J. Phys. Chem. A* **2009**, *113*, 3744.
97. M. V. Kirov, G. S. Fanourgakis, and S. S. Xantheas, *Chem. Phys. Lett.* **2008**, *461*, 180.
98. S. Patchkovskii and J. S. Tse, *Proc. Natl. Acad. Sci. U.S.A.* **2003**, *100*, 14645.
99. M. H. F. Sluiter, H. Adachi, R. V. Belosludov, V. R. Belosludov, and Y. Kawazoe, *Mater. Trans.* **2004**, *45*, 1452.
100. T. M. Inerbaev, V. R. Belosludov, R. V. Belosludov, M. Sluiter, and Y. Kawazoe, *Comp. Mater. Sci.* **2006**, *36*, 229.
101. M. Eddaoudi, H. Li, T. Reineke, M. Fehr, D. Kelley, T. L. Groy, and O. M. Yaghi, *Top. Catal.* **1999**, *9*, 105.
102. N. L. Rosi, J. Eckert, M. Eddaoudi, D. T. Vodak, J. Kim, M. O'Keeffe, and O. M. Yaghi, *Science* **2003**, *300*, 1127.
103. J. L. C. Roswell, A. R. Milward, K. S. Park, and O. M. Yaghi, *J. Am. Chem. Soc.* **2004**, *126*, 5666.
104. G. Wong-Foy, A. J. Matzger and O. M. Yaghi, *J. Am. Chem. Soc.* **2006**, *128*, 3494.

105. J. L. C. Roswell and O. M. Yaghi, *J. Am. Chem. Soc.* **2006**, *128*, 1304.
106. M. Latroche, S. Surblè, C. Serre, C. Mellot-Draznieks, P. L. Llewellyn, J. H. Lee, J. S. Chang, S. H. Jhung and G. Fèrey, *Angew. Chem., Int. Ed.* **2006**, *45*, 8227.
107. O. I. Lebedev, F. Millange, C. Serre, G. van Tendeloo, and G. Fèrey, *Chem. Mater.* **2005**, *17*, 6525.
108. X. Lin, J. Jia, X. Zhao, K. M. Thomas, A. J. Blake, G. S. Walker, N. R. Champness, P. Hubberstey and M. Schröder, *Angew. Chem., Int. Ed.* **2006**, *45*, 7358.
109. M. Dinca, A. Dailly, Y. Liu, C. M. Brown, D. A. Neumann, and J. R. Long, *J. Am. Chem. Soc.* **2006**, *128*, 16876.
110. P. M. Forster, J. Eckert, J.-S. Chang, S.-E. Park, G. Fèrey, and A. K. Cheetham, *J. Am. Chem. Soc.* **2003**, *125*, 1309.
111. Y. Liu, H. Kabbour, C. M. Brown, D. A. Neumann, and C. C. Ahn, *Langmuir* **2008**, *24*, 4772.
112. Blomqvist, C. M. Araújo, P. Srepusharawoot, and R. Ahuja, *Proc. Natl. Acad. Sci.* **2007**, *104*, 20173.
113. T. Sagara, J. Klassen, and E. Ganz, *J. Chem. Phys.* ***2001**, 121, 12543.*
114. P. Dalach, H. Frost, R. Q. Snurr, and D. E. Ellis, *J. Phys. Chem. C* **2008**, *112*, 9278.
115. S. J. Kolmann, B. Chan, and M. J. T. Jordan, *Chem. Phys. Lett.* **2008**, *467*, 126.
116. A.D. Boese and J.M.L. Martin, *J. Chem. Phys.* **2004**, ***121***, 3405.
117. C. Lee, W. Yang and R.G. Parr, *Phys. Rev. B* **1988**, ***37,*** 785.
118. A.D. Becke, *J. Chem. Phys.* **1993**, ***98***, 5648.
119. Y. Zhao and D.G. Truhlar, *J. Chem. Theory Comput.* **2007**, ***3***, 289.
120. J. L. C. Roswell and O. M. Yaghi, *Angew. Chem., Int. Ed.* **2005**, *44*, 4670.
121. A. K. Chandra, A. Goursot, and F. Fajula, *J. Mol. Catal. A: Chemical* **1997**, *119*, 45.
122. L. Campana, A. Selloni, J. Weber, A. Pasquarello, I. Papai, and A. Goursot, *Chem. Phys. Lett.* **1994**, *226*, 245.

123. S. Krishnamurty, S. Pal, R. Vetrivel, A. K. Chandra, A. Goursot, and F. Fajula, *J. Mol. Catal. A: Chemical* **1998**, *129*, 287.
124. A. Arbuznikov, V. Vasilyev, and A. Goursot, *Surf. Sci.* **1998**, *397*, 395.
125. D. Berthomieu, J.M. Ducéré, and A. Goursot, *Studies in Surf. Sci. Catal.* **2002**, *142*, 1899.
126. D. Berthomieu, A. Goursot, J-M. Ducéré, G. Delahay, B. Coq, and A. Martinez, *Studies in Surf. Sci. and Catal.* **2001**, *135*, 261.
127. A. Goursot, B. Coq, and F. Fajula, *J. Catal.* **2003**, *216*, 324.
128. S. Shetty, B. S. Kulkarni, D. G. Kanhere, A. Goursot, and S. Pal, *J. Chem. Phys. B* **2008**, *112*, 2573.
129. S. Shetty, S. Pal, D. G. Kanhere, and A. Goursot, *Chem. Eur. J.* **2006**, *12*, 518.
130. D. Berthomieu, N. Jardillier, G. Delahay, B. Coq, and A. Goursot, *Catal. Today* **2005**, *110*, 294.
131. N. Jardillier, D. Berthomieu, A. Goursot, J. U. Reveles, and A. M. Köster, *J. Phys. Chem. B* **2006**, *110*, 18440.
132. V. D. Dominguez-Soria, P. Calaminici, and A. Goursot, *J. Chem. Phys.* **2007**, *127*, 154710.
133. J. Weitkamp, M. Fritz, and S. Ernst, *Int. J. Hydrogen Energy* **1995**, *20, 967.*
134. H. W. Langmi, D. Book, A. Walton, S. R. Johnson, M. M. Al-Mamouri, J. D. Speight, P. P. Edwards, I. R. Harris, and P. A. Anderson, *J. Alloys Compd.* **2005***, 404-406*, 637.
135. L. Kang, W. Deng, K. Han, T. Zhang, and Z. Liu, *Catal. Today*, **2007**, *120*, 374.
136. J. Dong, X. Wang, H. Xu, Q. Zhao, and J. Li, *Int. J. Hydrogen Energy* **2007**, *32*, 4998.
137. S. H. Jhung, J. S. Lee, J. W. Yoon, D. P. Kim, and Jong-San Chang , *Int. J. Hydrogen Energy* **2007**, *32*, 4233.
138. M. Rahmati and H. Modarress, *Int. J. Hydrogen Energy* **2008**, *33*, 105.
139. G. T. Palomino, B. Bonelli, C. O. Areán, J. B. Parra, M. R. L. Carayol, M. Armandi, C. O. Ania, and E. Garrone, *Catal. Today*, 2008, *138*, 249.

140. K. P. Prasanth, R. S. Pillai, S. A. Peter, H. C. Bajaj, R.V. Jasra, H.D. Chung, T. H. Kim, and S. D. Song, *J. Alloys Compd.* **2008**, *466*, 439.
141. G. T. Palomino, M. R. L. Carayol, and C. O. Areán, *Appl. Surf. Sci.* **2009**, *255*, 4773.
142. K. P. Prasanth, H. C. Bajaj, H. D. Chung, K.Y. Choo, T. H. Kim, and R. V. Jasra*, Int. J. Hydrogen Energy* **2009**, *34*, 888.
143. A. Zecchina, S. Bordiga, J. G. Vitillo, G. Ricchiardi, C.Lamberti, G. Spoto, M. Bjorgen, and K. P. Lillerud, *J. Am. Chem. Soc.* **2005**, *127*, 6361.
144. L. Chen, R. K. Singh, and P. Webley, *Micropor. Mesopor. Mater.* **2007**, *102*, 159.
145. M. Armandi, B. Bonelli, C. O. Arean, and E. Garrone, *Micropor. Mesopor. Mater.* **2008**, *112*, 411.
146. Z. Yang, Y. Xia, and R. Mokaya, *J. Am. Chem. Soc.* **2007**, *129*, 1673.
147. A. Lachawiec and R.T. Yang, *Langmuir* **2008**, *24*, 6159.
148. C. Guan, X. Zhang, K. Wang, and C. Yang, *Sep. and Purification Tech.* **2009**, *66*, 565.
149. C. Guan. K. Wang, C. Yang, and X. S. Zhao, *Micropor. Mesopor. Mater.* **2009**, *118*, 503.
150. T. Roussel, C. Bichara, K. E. Gubbins, and R. J. –M. Pellenq, *J. Chem. Phys.* **2009**, *130*, 174717.
151. H. Nishihara, Peng-Xiang Hou, Li-Xiang Li, M. Ito, M. Uchiyama, T. Kaburagi, A. Ikura, J. Katamura, T. Kawarada, K. Mizuuchi, and T. Kyotani, *J. Phys. Chem. C* **2009**, *113*, 3189.
152. Y. H. Lu, W. Chen, Y. P. Feng, and P. M. He, *J. Phys. Chem. B* **2009**, *113*, 2.
153. Y. H. Lu, P. M. He, and Y. P. Feng, *J. Phys. Chem. C* **2008**, *112*, 12683.
154. Z. H. Ni, T. Yu, Y. H. Lu, Y. Y. Wang, Y. P. Feng, and Z. X. Shen, *ACS Nano* **2008**, *2*, 2301.
155. T. Heine, L. Zhechkov, and G. Seifert, *Phys. Chem. Chem. Phys.* **2004**, *6*, 980.

156. L. Zhechkov, T. Heine, and G. Seifert, *Int. J. Quantum Chem.* **2005**, *106*, 1375.
157. S. Patchkovskii, J. S. Tse, S. N. Yurchenko, L. Zhechkov, T. Heine, and G. Seifert, *Proc. Natl. Acad. Sci.* **2005**, *102*, 10439.
158. A. Kuc, L. Zhechkov, S. Patchkovskii, G. Seifert, and T. Heine, *Nano Lett.* **2007**, *7*, 1.
159. A. Ghosh, K. S. Subrahmanyam, K. S. Krishna, S. Datta, A. Govindaraj, S. K. Pati, and C. N. R. Rao, *J. Phys. Chem. C* **2008**, *112*, 15704.
160. S. Dutta, S. Lakshmi, and S. K. Pati, *Phys. Rev. B* **2008**, *77*, 073412.
161. S. Dutta and S. K. Pati, *J. Phys. Chem. B* **2008**, *112*, 1333.
162. S. Dutta, A. K. Manna, and S. K. Pati, *Phys. Rev. Lett.* **2009**, *102*, 096601.
163. Y. H. Lu, R. Q. Wu, L. Shen, M. Yang, Z. D. Sha, Y. Q. Cai, P. M. He, and Y. P. Feng, *Appl. Phys. Lett.* **2009**, *94*, 122111.

CHAPTER 2

Theoretical background

He who loves practice without ***theory***
is like the sailor who boards ship
without a rudder and compass
and never knows where to be cast.
-Leonardo da Vinci

In this chapter we outline the theoretical framework behind the methodology used in most part of the work presented in this thesis. We begin in Section 2.1 with a brief introduction to the many-body problem by discussing the Born-Oppenheimer approximation, Hartree approximation, Hartree-Fock theory, and methods beyond Hartree-Fock. In Section 2.2 we provide a summary of density functional theory which is as an alternative route for performing such calculations. Special attention is given to the Hohenberg-Kohn theorems, Kohn-Sham equations, and the different exchange-correlations functionals. In Section 2.3 a description of the concepts of molecular dynamics is given while the foundations of *ab initio* molecular dynamics are laid in Section 2.4. In Section 2.4 we explain and compare the ideas and algorithms behind Born-Oppenheimer molecular dynamics and Car-Parrinello molecular dynamics. Lastly, the implementation of the abovementioned methods via the plane wave-pseudopotential approach employed in Vienna *ab initio* simulations package (VASP) for performing solid-state calculations is discussed in section 2.5.

2.1
The many-body problem

Any given system composed of N electrons and M nuclei can be determined by solving the Schrödinger equation. The *time-independent Schrödinger equation* [1] has the form

$$H\boldsymbol{\Psi} = E\boldsymbol{\Psi} \tag{2.1.1}$$

where $\boldsymbol{\Psi}$ is the wavefunction of the system, E is the energy eigenvalue and H is the Hamiltonian operator. H is the sum of the kinetic energy T and potential energy V operators and can be written as

$$H = -\sum_{i=1}^{N} \frac{\hbar^2}{2m}\nabla_i^2 - \sum_{A=1}^{M} \frac{\hbar^2}{2M_A}\nabla_A^2 + \frac{1}{2}\sum_{i\neq j}^{N} \frac{e^2}{r_{ij}} + \frac{1}{2}\sum_{A\neq B}^{M} \frac{Z_A Z_B e^2}{R_{AB}} - \sum_{i=1}^{N}\sum_{A=1}^{M} \frac{Z_A e^2}{r_{iA}} \tag{2.1.2}$$

In the above equation the first two terms are the kinetic energies of N electrons with masses m and M nuclei with masses M_A, the third term is the electrostatic repulsion between electrons separated by r_{ij}, fourth term is the electrostatic repulsion between nuclei separated by R_{AB} and the last term is the Coulombic attraction between electrons and nuclei r_{iA} distance apart.

2.1.1
Born-Oppenheimer approximation

Since nuclei have much larger masses their velocities are consequently smaller compared to electrons. The *Born-Oppenheimer approximation* [2] assumes that the nuclei are fixed which amounts to removing the second term in Equation (2.1.2). Further, the fourth term is a constant and is included in the total energy after calculating the wavefunction. These simplifications result in the electronic Hamiltonian operator:

$$H_e = -\sum_{i=1}^{N} \frac{1}{2}\nabla_i^2 + \sum_{i \neq j}^{N} \frac{1}{r_{ij}} - \sum_{i=1}^{N}\sum_{A=1}^{M} \frac{Z_A e^2}{r_{iA}} \tag{2.1.3}$$

The conceptual and numerical problems related to the electron-electron interactions in Equation (2.1.3) are the most challenging to deal with. An elementary scheme would be to set the corresponding terms to zero implying that the N electrons move completely independent of each other. Then the total wavefunction **Ψ**

$$\Psi = \psi_1(r_1)\psi_2(r_2)\dots\psi_N(r_N) \tag{2.1.4}$$

becomes a product of N one-electron wavefunctions ψ_i. However such a Hamiltonian is very archaic and hence electron-electron interactions must be calculated.

2.1.2
Hartree approximation

Under the Hartree approximation each electron is thought of as moving in a field built by all other electrons. The electron-electron interactions then depend only on the positions of the electron under consideration which moves in an electronic sea made by the rest of the electrons. The second term in Equation (2.1.3) can therefore be approximated as a sum of one-electron potentials v_i

$$\sum_{i \neq j}^{N} \frac{1}{r_{ij}} \approx \sum_{i=1}^{N} v_i(r_i) = \sum_{i=1}^{N} \int \frac{\rho(r_j) - |\psi_i(r_j)|^2}{|r_i - r_j|} dr_j \tag{2.1.5}$$

where ψ_i is the orbital for the i^{th} electron. The solution of Hartree approximation needs to be derived self-consistently because calculation of ψ_i depends on $\Sigma(1/r_{ij})$ which in turn is defined in terms of ψ_i. The total wavefunction is still expressed as the

Hartree product as given in Equation (2.1.4). However it is not antisymmetric with respect to exchange of electrons and does not account for the Pauli exclusion principle. In order to bring in the Pauli exclusion principle one has to go beyond the Hartree method.

2.1.3
Hartree-Fock approximation

The many electron wavefunction **Ψ** may be approximated in the form of a *Slater determinant* composed of an antisymmetrized product of *N* orthonormal spin orbitals $\psi_i(x)$ for all the electrons, where each $\psi_i(x)$ is a product of a spatial orbital $\varphi_k(r)$ and a spin function $\sigma(s) = \alpha(s)$ *or* $\beta(s)$.

$$\Psi_{HF} = \frac{1}{\sqrt{N!}} \begin{vmatrix} \psi_1(x_1)...\psi_2(x_1)............\psi_N(x_1) \\ \psi_1(x_2)...\psi_2(x_2)...........\psi_N(x_2) \\ .... \\ .... \\ \psi_1(x_N)...\psi_2(x_N)........\psi_N(x_N) \end{vmatrix} \equiv \frac{1}{\sqrt{N!}} \det[\psi_1\psi_2....\psi_N]$$

(2.1.6)

In the *Hartree-Fock (HF) approximation* [3] the orthonormal spin orbitals that minimize the total energy given by

$$E[\Psi] = \frac{\langle \Psi | H | \Psi \rangle}{\langle \Psi | \Psi \rangle} \tag{2.1.7}$$

for the above determinant form of Ψ_{HF} are found. The normalization integral $\langle \Psi_{HF} | \Psi_{HF} \rangle$ is equal to 1 and energy is given by the formula

$$E_{HF} = \langle \Psi_{HF} | H | \Psi_{HF} \rangle = \sum_{i=1}^{N} H_i + \frac{1}{2}\sum_{i,j=1}^{N} (J_{ij} - K_{ij}) \tag{2.1.8}$$

where $$H_i = \int \psi_i^*(x)\left[-\frac{1}{2}\nabla^2 + v(x)\right]\psi_i(x)dx \tag{2.1.9}$$

$$J_{ij} = \iint \psi_i(x_1)\psi_i^*(x_1)\frac{1}{r_{12}}\psi_j^*(x_2)\psi_j(x_2)dx_1dx_2 \tag{2.1.10}$$

$$K_{ij} = \iint \psi_i^*(x_1)\psi_j(x_1)\frac{1}{r_{12}}\psi_i(x_2)\psi_j^*(x_2)dx_1dx_2 \tag{2.1.11}$$

The J_{ij} are called C*oulomb integrals* and K_{ij} are called *exchange integrals*. Minimization of Equation (2.1.8) subject to the orthogonalization conditions gives the HF differential equations

$$F\Psi_i(x) = \sum_{j=1}^{N} \varepsilon_{ij}\psi_j(x) \tag{2.1.12}$$

where $$F = -\frac{1}{2}\nabla^2 + v + g = -\frac{1}{2}\nabla^2 + v + j - k \tag{2.1.13}$$

and *j* and *k* are the Coulomb and exchange operators respectively. In the HF scheme the one-electron effective potential has the form $v + g$, where v is the potential of an electron in the external field and g is equal to sum of Coulomb potential, taking into account the repulsion of the other electrons, and the exchange potential, which has no classical interpretation and is caused by the antisymmetrization of the one-electron functions in the expressions for ψ. The Coulomb and exchange potentials for each ψ_i depend on the solutions ψ_j of all the other equations with j≠i. Therefore the HF equations form a system of interrelated equations that is solved by the *self-consistency method*.

Even if the HF equations are correctly solved, the method eventually turns out to be theoretically incomplete. Despite the correct treatment of electronic exchange within the HF theory, electronic correlation is totally missing. Consequently the *correlation energy* may be defined as the difference between the correct energy and that of the HF solution i.e. $E_{corr} \equiv E - E_{HF}$. Therefore, for including correlation one has to go beyond the HF theory.

2.1.4
Beyond Hartree-Fock

Some instances of the different methods that take correlation effects into account are the Møller-Plesset (MP) perturbation theory [4], configuration interaction (CI) [5] and coupled cluster (CC) [6]. In MP perturbation theory the difference between the exact Hamiltonian and sum of one electron operators is introduced as a perturbation to the unperturbed HF solution. Correlation corrections can be derived to a chosen order. Another way to include correlation is to work with a multi-determinant wavefunction instead of the single-determinant wavefunction. This approach is used in CI and CC methods. Treatment of exchange and correlation follows another route in the density functional theory which is covered in the next section.

2.2
Density functional theory

The *density functional theory* (DFT) [7] allows one to move away from the *N*-electron wavefunction $\mathbf{\Psi}$ and its associated Schrödinger equation and replace them by the much simpler electron density $\rho(r)$ and its corresponding calculation scheme. The history of using electron density as the basic variable began with the pioneering work of Thomas and Fermi.

2.2.1
Thomas-Fermi theory

Thomas [8] and Fermi [9] proposed in 1927 that statistical considerations can be used to estimate the distribution of electrons in an atom. In this method the kinetic energy is approximated as an explicit functional of density, idealized as non-interacting electrons in a homogeneous gas with a density equal to the local density at the given point. Neglecting the exchange and correlation terms, the *Thomas-Fermi (TF) total energy* of an atom with a nuclear charge Z in terms of electron density is given by

$$E_{TF}[\rho(r)] = C_F \int \rho^{5/3}(r)dr - Z\int \frac{\rho(r)}{r}dr + \frac{1}{2}\iint \frac{\rho(r)\rho(r')}{|r-r'|}drdr' \qquad (2.2.1)$$

where the Fermi coefficient C_F = 2.871. Assuming that for the ground state of an atom the electron density minimizes the energy functional $E_{TF}[\rho(r)]$ under the constraint

$$N = N[\rho(r)] = \int \rho(r)dr \qquad (2.2.2)$$

Applying the method of Lagrange multipliers to incorporate the constraint, the ground-state electron density must satisfy the variational principle

$$\delta\left\{E_{TF}[\rho] - \mu_{TF}\left(\int \rho(r)dr - N\right)\right\} = 0 \qquad (2.2.3)$$

which yields

$$\mu_{TF} = \frac{\delta E_{TF}[\rho]}{\delta\rho(r)} = \frac{5}{3}C_F\rho^{2/3}(r) - -\left[\frac{Z}{r} - \int \frac{\rho(r_2)}{|r-r_2|}dr_2\right] \qquad (2.2.4)$$

Hence, the TF theory involves solving the Equation (2.2.4) under the constraint (2.2.2) and inserting the resulting electron density in Equation (2.2.1) to yield the total energy.

The TF theory though allows the explicit calculation of an atom's total energy, its accuracy is low. The errors for the total energies of atoms are relatively large and still more for molecules which are unstable within the TF theory. Due to these reasons, this method was considered as an oversimplified model.

2.2.2
Hohenberg-Kohn theorems

The modern formulation of density functional theory originated with the fundamental theorems of Hohenberg and Kohn [10]. The *first Hohenberg-Kohn (HK) theorem* states that: *The external potential v(r) is determined, within a trivial additive constant, by the electron density ρ(r).* Since *ρ(r)* determines the number of electrons, it follows that *ρ(r)* also determines the ground-state wavefunction **Ψ** and all other properties such as kinetic energy $T[\rho]$, potential energy $V[\rho]$ and total energy $E[\rho]$ of the system. Hence the ground state expectation value of any observable, including the total energy, is a unique functional of the ground-state electron density *ρ(r)*.

$$E_v[\rho] = T[\rho] + V_{ne}[\rho] + V_{ee}[\rho] = \int \rho(r)v(r)dr + F_{HK}[\rho] \qquad (2.2.5)$$

where

$$F_{HK}[\rho] = T[\rho] + V_{ee}[\rho] \qquad (2.2.6)$$

The *second HK theorem* states that: *For a trial density* $\tilde{\rho}(r)$ *such that* $\tilde{\rho}(r) \geq 0$ *and* $\int \tilde{\rho}(r)dr = N$,

$$E_0 \leq E_v[\tilde{\rho}] \qquad (2.2.7)$$

This provides a variational principle such that the search for the lowest-energy wavefunction $\mathbf{\Psi_0(r)}$ can be replaced by a search for the lowest energy electron density $\rho_0(r)$ and the ground-state energy E_0 is given as the minimum of the functional $E_v[\rho(r)]$.

The classical part of the electron-electron interaction $V_{ee}[\rho]$ in Equation (2.2.6) is the Coulomb potential energy

$$J[\rho] = \frac{1}{2}\iint \frac{\rho(r_1)\rho(r_2)}{|r_2 - r_1|} dr_1 dr_2 \qquad (2.2.8)$$

In the TF theory $V_{ee}[\rho]$ is replaced by $J[\rho]$ and kinetic energy $T[\rho]$ is taken from the theory of a non-interacting uniform electron gas. This constitutes a direct approach for calculating $T[\rho]$ and therefore the total energy if the electron density is known but only approximately. It would however be preferable to correctly calculate $T[\rho]$ as it forms the leading part of the total energy. Kohn and Sham proposed introducing orbitals into the problem allowing more accurate computation of $T[\rho]$ with a small residual correction that is handled separately.

2.2.3
Kohn-Sham equations

For a system of noninteracting electrons the kinetic energy is

$$T_0 = \sum_{i=1}^{N} n_i \langle \psi_i | -\frac{1}{2}\nabla^2 | \psi_i \rangle \tag{2.2.9}$$

and the electron density is

$$\rho(r) = \sum_{i=1}^{N} n_i \, | \psi_i(x) |^2 \tag{2.2.10}$$

with x including both space and spin coordinates. Here ψ_i and n_i are the natural spin orbitals and their occupation numbers respectively. Using orbitals to calculate the kinetic energy is an indirect though accurate approach.

Kohn and Sham [11] replaced the interacting many-body problem by a corresponding noninteracting particle system with the same density in an appropriate external potential. The total energy functional is then expressed in atomic units as

$$E[\rho(r)] = T_0[\rho(r)] + \frac{1}{2}\iint \frac{\rho(r)\rho(r')}{|r-r'|} dr dr' + E_{XC}[\rho(r)] + \int \rho(r) v(r) dr \tag{2.2.11}$$

In the above equation the first term is the kinetic energy functional of the system of noninteracting electrons with the same density, the second term is the classical Coulomb energy for the electron-electron interaction, the third term is energy functional incorporating all the many-body effects of exchange and correlation and the last term is the attractive Coulomb potential provided by the fixed nuclei.

The construction of the *Kohn-Sham (KS) functional* is based on the assumption that the exact ground state density can be represented by the ground state density of an auxiliary system of noninteracting particles. The solution of the KS auxiliary system can be viewed as the minimization problem of the KS functional with respect to the density. This leads to N KS equations

$$\left[-\frac{1}{2}\nabla^2 + v_{eff}(r)\right]\psi_i(r) = \varepsilon_i\psi_i(r) \tag{2.2.12}$$

and

$$\rho(r) = \sum_i^N \sum_s |\psi_i(r,s)|^2 \tag{2.2.13}$$

Here ε_i are eigenvalues, ψ_i are KS orbitals and v_{eff} is the effective potential

$$v_{eff}(r) = v(r) + \int \frac{\rho(r^{'})}{|r - r^{'}|} dr^{'} + v_{XC}(r) \tag{2.2.14}$$

that is the sum of potential from the nuclei, a Hartree-style potential and the potential for exchange and correlation. The latter is defined as

$$v_{XC}(r) = \frac{\partial E_{XC}[\rho(r)]}{\partial \rho(r)} \tag{2.2.15}$$

In Equation (2.2.15) v_{eff} depends on $\rho(r)$. Hence the KS Equations (2.2.12), (2.2.13) and (2.2.14) have to be solved self-consistently. Therefore, in a DFT calculation one begins with a guess for $\rho(r)$ for constructing v_{eff} from Equation (2.2.14). After the first iteration we get a new electron density from which the Hartree and exchange-correlation potentials are generated to yield a new potential. This process is repeated until self-consistency is achieved.

2.2.4
Exchange-correlation functionals

In the KS equations while the kinetic energy is incorporated correctly, a challenge in DFT is the search for a good approximation of the exchange-correlation functional $E_{XC}[\rho]$. One of the many approaches is the *local density approximation (LDA)* [11]. The LDA exchange-correlation energy functional is given as

$$E_{XC}^{LDA}[\rho] = \int \rho(r)\varepsilon_{XC}[\rho(r)]dr \tag{2.2.16}$$

where $\varepsilon_{XC}[\rho]$ is the exchange-correlation energy per particle of a uniform electron gas of density $\rho(r)$. The exchange part of $\varepsilon_{XC}[\rho]$ can be expressed analytically by that of a homogeneous electron gas.

$$\varepsilon_X[\rho(r)] = -C_X\rho(r)^{1/3}, \quad C_X = \frac{3}{4}\left(\frac{3}{\pi}\right)^{1/3} \tag{2.2.17}$$

The correlation part may be obtained from perturbation theory or from Quantum Monte Carlo method. The corresponding exchange-correlation potential and KS equation then become

$$v_{XC}^{LDA}(r) = \frac{\delta E_{XC}^{LDA}}{\delta\rho(r)} = \varepsilon_{XC}[\rho(r)] + \rho(r)\frac{\partial\varepsilon_{XC}[\rho(r)]}{\partial\rho} \tag{2.2.18}$$

$$\left[-\frac{1}{2}\nabla^2 + v(r) + \int\frac{\rho(r^{'})}{|r-r^{'}|}dr^{'} + v_{XC}^{LDA}(r)\right]\psi_i(r) = \varepsilon_i\psi_i(r) \tag{2.2.19}$$

The self-consistent solution of Equation (2.2.19) defines the *LDA method*. Application of LDA amounts to assuming that the exchange-correlation energy for a nonuniform system can be obtained by applying uniform electron gas results to infinitesimal portions of the nonuniform electron distribution and then summing over all individual contributions.

LDA is expected to work for systems with slowly varying electron densities. However it was successful for even semiconductors and insulators due to large cancellations in the exchange part. Hence further improvements are called for. A route to bring about this improvement is to take into account the gradient of the electron density. The idea is to include ∂ρ(r)/∂r as well as ρ(r) to describe the exchange hole. This is implemented via the method of *generalized gradient approximation* (GGA) in which the exchange-correlation energy functional is written as

$$E_{XC}^{GGA}[\rho(r)] = \int \rho(r) F[\rho(r), \nabla\rho(r)] dr \qquad (2.2.20)$$

In 1986 the exchange part of $E_{XC}^{GGA}[\rho(r)]$ was proposed by Perdew and Wang (PW86) [12] and another correction was developed by Becke in 1988 (B88) [13]. Gradient corrections to the correlation part were proposed in 1986 by Perdew (P86) [14], in 1991 by Perdew and Wang (PW91) [15], in 1988 by Lee, Yang and Parr (LYP) [16] and in 1996 by Perdew, Burke and Ernzerhof (PBE) [17]. In all our density functional calculations the PW91 GGA functional has been employed.

2.3
Molecular dynamics

The aim of *molecular dynamics* (MD) is to model the detailed microscopic dynamical behavior of many different types of systems as found in chemistry, physics or biology. In such a scenario, the motions of nuclei must be taken care from the beginning.

In the MD method, nuclear motion of the particles is described using the laws of Newton's mechanics whereby every new distribution is derived from the previous one by using the interactions between the particles. For an i^{th} particle of the system, the total potential energy at time $t_0=0$ is computed as a sum of all pair interactions u_{ij}

$$u(\vec{r}_i) = \sum_j u_{ij}(\vec{r}_i, \vec{r}_j) \tag{2.3.1}$$

Once this is obtained the force acting on the particle can be calculated as

$$\vec{f}_i = -\nabla u(\vec{r}_i) \tag{2.3.2}$$

which causes an acceleration

$$\vec{a}_i = \frac{\vec{f}_i}{m} \tag{2.3.3}$$

This in turn modifies the initial velocity $\vec{v}_i$ to $\vec{v}_i^{'}$ and then every particle is allowed to move with that velocity over a short period of time Δt. This produces new positions $\vec{r}_i^{'}$ for all the particles at time $t_1 = t_0 + \Delta t$. Next the potential energies $u_i^{'}$, forces $\vec{f}_i^{'}$ and velocities $\vec{v}_i^{''}$ are calculated for this new distribution. This procedure is repeated for a large number of times. Therefore MD simulations can describe systems that evolve in time. The new positions are derived from the Newtonian laws of motion and are therefore deterministic.

2.3.1
Equations of motion

The Hamiltonian for a system of N particles moving under the influence of a potential function $U(R^N)$ is given by

$$H(R^N, P^N) = \sum_{I=1}^{N} \frac{P_I^2}{2M_I} + U(R^N) \qquad (2.3.4)$$

where R^N and P^N are the sets containing all the positions and momenta respectively. The forces are derived from the potential

$$F_I(R^N) = -\frac{\partial U(R^N)}{\partial R_I} \qquad (2.3.5)$$

The equations of motion are according to Hamilton's equations

$$\dot{R}_I = \frac{\partial H}{\partial P_I} = \frac{P_I}{M_I} \; ; \; \dot{P}_I = -\frac{\partial H}{\partial R_I} = -\frac{\partial U}{\partial R_I} = F_I(R^N) \qquad (2.3.6)$$

From which the Newton's second law is obtained

$$M_I \ddot{R}_I = F_I(R^N) \qquad (2.3.7)$$

The equations of motion are integrated and atomic trajectories are followed on the potential energy surface.

2.3.2
Numerical integration

The numerical integration techniques are based on a discretization of time and a repeated calculation of the forces on the particles. These methods must have the properties of (a) long time energy conservation to ensure that we stay on the constant energy hypersurface and short time reversibility and (b) short time reversibility so that the discrete equation still exhibit the time reversible symmetry of the original differential equations.

A computationally efficient scheme is the *Verlet algorithm* [18]. To derive it $\vec{r}_i(t)$ is expanded forward and backward in time in the third order of Taylor expansion.

$$\vec{r}_i(t+\delta t) = \vec{r}_i(t) + \vec{v}_i(t)\delta t + \frac{1}{2m_i}\vec{f}_i(t)(\delta t)^2 + \frac{1}{6}\vec{b}_i(t)(\delta t)^3 + O((\delta t)^4) \quad (2.3.8)$$

$$\vec{r}_i(t-\delta t) = \vec{r}_i(t) - \vec{v}_i(t)\delta t + \frac{1}{2m_i}\vec{f}_i(t)(\delta t)^2 - \frac{1}{6}\vec{b}_i(t)(\delta t)^3 + O((\delta t)^4) \quad (2.3.9)$$

Adding we get, $$\vec{r}_i(t+\delta t) = 2\vec{r}_i(t) - \vec{r}_i(t-\delta t) + \frac{1}{m_i}\vec{f}_i(t)(\delta t)^2 + O((\delta t)^4) \quad (2.3.10)$$

Subtraction yields $$\vec{v}_i(t) = \frac{1}{2(\delta t)}[\vec{r}_i(t+\delta t) - \vec{r}_i(t-\delta t)] + O((\delta t)^3) \quad (2.3.11)$$

A MD simulation is usually performed for a fixed number of particles N inside a fixed volume. The initial values for positions and velocities are chosen together with an appropriate time step. The first part of the simulation is the equilibration phase in which strong fluctuations may occur. Once all the important quantities are sufficiently equilibrated, the actual simulation is performed. The time evolution of such a microcanonical ensemble is accumulated over many time steps. Finally observables are calculated from the trajectory as time averages which are thought of as being comparable to experimentally observed ensemble averages.

2.4
Ab initio molecular dynamics

The basic idea underlying every *ab intio molecular dynamics* (AIMD) method is to compute the forces acting on the nuclei from electronic structure calculations that are performed on-the-fly as the MD trajectory is generated. In this way the electronic variables are not generated beforehand, but are considered as active degrees of freedom. This implies, that given a suitable approximate solution of the many-electron problem, chemically complex systems can also be handled by MD. This implies that now, one has to select a particular approximation for solving the Schrödinger equation.

2.4.1
Born-Oppenheimer molecular dynamics

The most commonly employed approach to AIMD is the *Born-Oppenheimer molecular dynamics* (BOMD) in which the electronic problem is solved using DFT for obtaining the ground state eigenvalue. For an interacting system of electrons with classical nuclei fixed at positions $\{R^N\}$, the total ground state energy can be found by minimizing the KS energy functional (as defined in Equation 2.2.11)

$$\min_{\Psi_0}\left\{\left\langle \Psi_0 \mid H_e \mid \Psi_0 \right\rangle\right\} = \min_{\{\phi_i\}} E^{KS}\left[\{\phi_i\}, R^N\right] \tag{2.4.1}$$

with respect to orbitals which are subject to the orthonormality constraint

$$\left\langle \phi_i \middle| \phi_j \right\rangle = \delta_{ij} \tag{2.4.2}$$

The corresponding Lagrangian for BOMD is therefore

$$L_{BO}(R^N, \dot{R}^N) = \sum_{I=1}^{N} \frac{1}{2} M_I \dot{R}_I^2 - \min_{(\phi_i\}} E^{KS}[\{\phi_i\}, R^N] \tag{2.4.3}$$

and the equations of motion are

$$M_I \ddot{R}_I = -\nabla_I \left[\min_{(\phi_i\}} E^{KS}[\{\phi_i\}, R^N] \right] \tag{2.4.4}$$

The forces between nuclei needed for the implementation of BOMD are

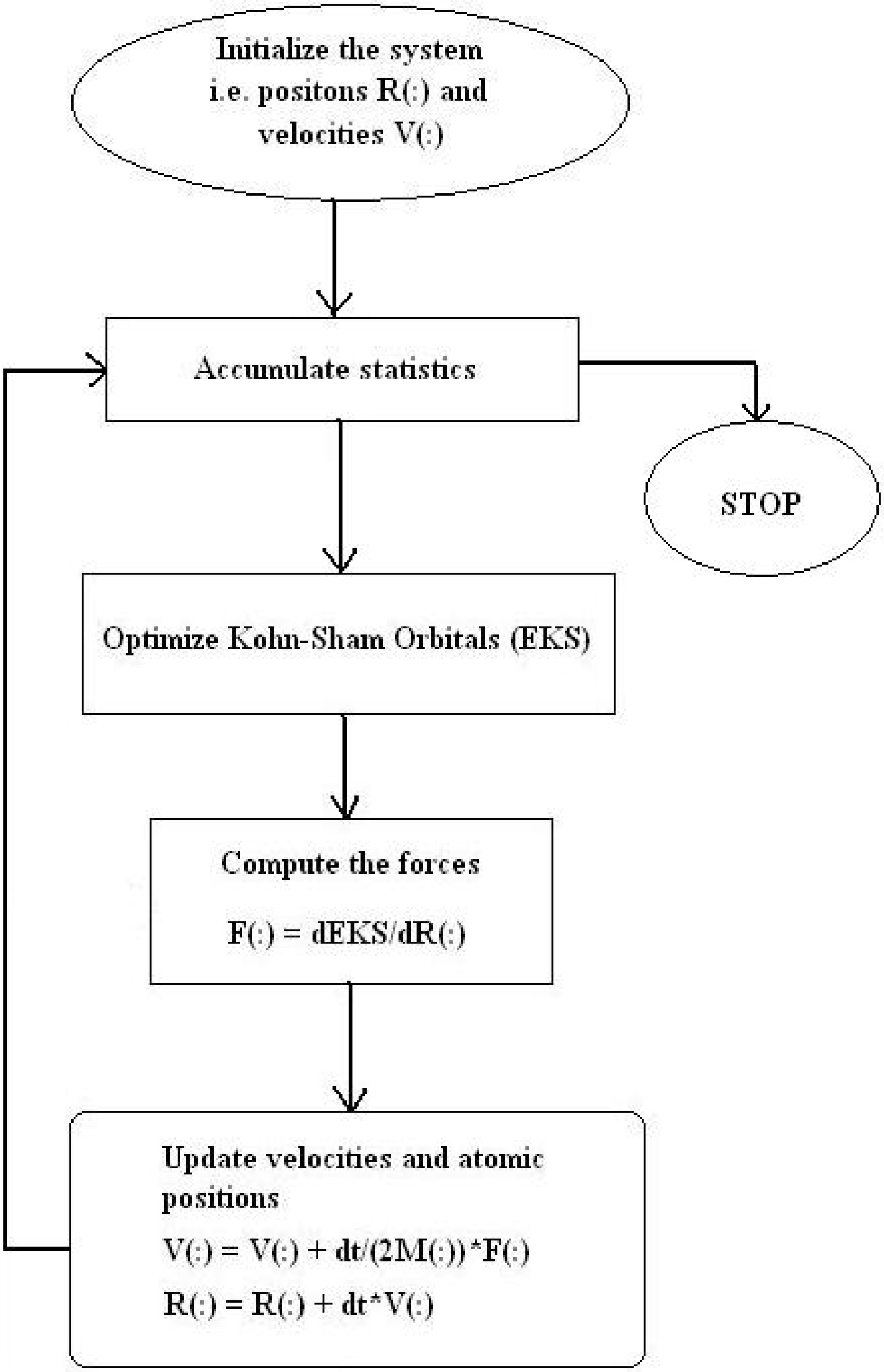

Figure 2.1 Flowchart displaying the steps involved in the Born-Oppenheimer Molecular Dynamics algorithm.

$$\frac{d}{dR_I}\left[\min_{\{\phi_i\}} E^{KS}[\{\phi_i\}, R^N]\right] \tag{2.4.5}$$

Once the initial forces are calculated they are next fed into a numerical integration procedure together with a set of initial velocities for the nuclei, and a step of molecular dynamics is carried out, yielding a new set of positions and velocities. At the new nuclear positions, the energy functional is minimized again and a new set of forces is obtained and used to perform another step of MD propagation. This procedure is repeated until an entire trajectory has been generated.

These steps involved in BOMD are displayed in the form of a flowchart presented in Fig. 2.1 which tells that BOMD requires a full self-consistent density functional minimization of energy and its derivative at each point. For cutting down computational expenses it would therefore be appealing to have an approach that does not require exact calculation of ground state energy at every step. An elegant alternative to BOMD was proposed by Car and Parrinello [24].

2.4.2
Car-Parrinello molelcular dynamics

Car-Parrinello molecular dynamics (CPMD) [19] is an efficient way to combine a quantum chemical description of electron dynamics and a classical description of nuclei dynamics in a unique framework. The Car-Parinello approach exploits the time-scale separation of fast electronic and slow nuclear motion. This is achieved by mapping the two-component quantum/classical problem onto a two-component purely classical problem with two separate energy scales.

In CPMD the extended energy functional ε^{KS} is considered to be dependent on $\{\Phi_i\}$ and R^N. In classical mechanics the force of the nuclei is obtained as the derivative of a Lagrangian with respect to the nuclear positions. Similarly, a functional derivative with respect to the orbitals, which if also interpreted as classical fields, would yield the force on the orbitals. Car and Parinello postulated the following Lagrangian using ε^{KS}

$$L_{CP}(R^N,\dot{R}^N,\{\phi_i\},\{\dot{\phi}_i\})=\sum_{I=1}^{N}\frac{1}{2}M_I\dot{R}_I^2+\sum_i\frac{1}{2}\mu\langle\dot{\phi}_i|\dot{\phi}_i\rangle-\varepsilon^{KS}[\{\phi_i\},R^N] \qquad (2.4.9)$$

and the equations of motion are

$$M_I\ddot{R}_I(t)=-\frac{\partial E^{KS}}{\partial R_I}+\sum_{ij}\Lambda_{ij}\frac{\partial}{\partial R_I}\langle\phi_i|\phi_j\rangle \qquad (2.4.10)$$

$$\mu\ddot{\phi}_i(t)=-\frac{\delta E^{KS}}{\delta\langle\phi_i|}+\sum_j\Lambda_{ij}|\phi_j\rangle \qquad (2.4.11)$$

where μ is the "fictitious mass" or inertia parameter assigned to the degrees of freedom. The forces needed for the implementation of CPMD can be obtained as the partial derivatives of the KS energy functional with respect to both the nuclear positions and the KS orbitals

$$F(\Phi_i)=-f_iH^{KS}\phi_i \qquad (2.4.12)$$

$$F(R_I)=-\frac{\partial E^{KS}}{\partial R_I} \qquad (2.4.13)$$

The forces in Equation (2.4.13) are the same forces as in BOMD but in BOMD these were derived under the condition that the wavefunctions are optimized and are therefore are only correct up to the accuracy achieved in the wavefunction optimization. In CPMD these are the correct forces and calculated from analytic energy expressions are correct to machine precision.

In CPMD we begin with a starting configuration for which the KS equation is solved for the electrons. Next the forces are evaluated as the derivative of E^{KS} with respect to nuclear positions as given in Equation (2.4.13). In the same nuclear step the fictitious forces acting on the orbitals are calculated as the functional derivative of E^{KS} with respect to orbitals (see Equation (2.4.12)). This is followed by an update of

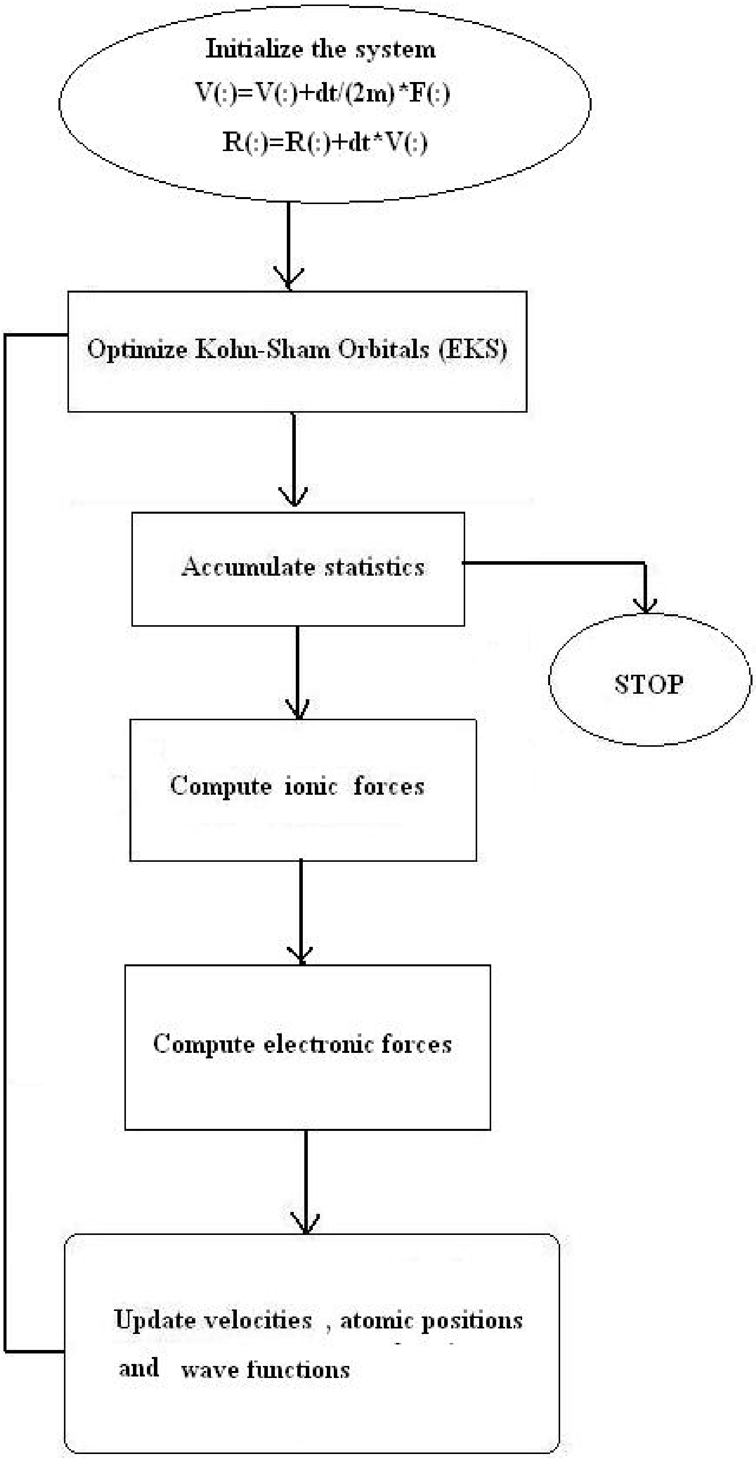

Figure 2.2 Flowchart displaying the steps involved in the Car-Parrinello Molecular Dynamics algorithm.

the nuclear and electronic configurations and another step of MD is performed. For generating a trajectory these steps are continuously repeated.

The flowchart of the above CPMD algorithm is shown in Fig. 2.2. It is noticeable that only one electronic step is performed for all the nuclear steps and hence the computationally demanding full electronic minimization is executed only for the starting configuration. If μ is small then the new electronic configuration corresponding to the new nuclear configuration will be already near enough to the exact ground state. On the other hand if μ is large then it ensures the use of reasonably large time steps, in order to have a fast integration of the equations.

2.5
Plane wave-pseudopotential method

This section discusses the implementation of the *plane wave-pseudopotential method* within the program code VASP [20,21] used during the course of this work for calculating properties of solids. In an extended solid-state material the number of nuclei and electrons is of the order one mole. The computational problem of solving Schrödinger's equation involves diagonalization of large matrices of the order of one mole X one mole. This challenging task is simplified by exploiting the translational symmetry properties of the crystal in question.

2.5.1
Bloch's theorem and plane wave basis

In an infinite crystal which is translationally invariant under a lattice translation T, the effective KS potential v_{eff} as defined in Equation (2.2.14) possesses the periodicity of the lattice

$$v_{eff}(r + T) \equiv v_{eff}(r) \qquad (2.5.1)$$

Further, in order to satisfy the KS equations one must have

$$\psi_i(k, r+T) = e^{ikT}\psi_i(k,r) \tag{2.5.2}$$

This results in the *Bloch's theorem* [22] for the KS orbitals according to which ψ_i(k,r) can be written as a product of a function $u_i(k,r)$ that has the periodicity of the lattice and a *plane wave* $e^{ik.r}$ with k being a vector in the first *Brillouin zone* (BZ), i.e.

$$\psi_i(k,r) = e^{ikr}u_i(k,r) \tag{2.5.3}$$

The periodic function can be expanded in the plane wave basis as

$$u_i(r,k) = \frac{1}{\sqrt{\Omega_{cell}}}\sum_G c_i(G,k)\exp[iG.r] \tag{2.5.4}$$

where Ω_{cell} is the volume of the primitive cell and G are the reciprocal lattice vectors. In the above form the $\psi_i(k,r)$'s are k-dependent. The complete set of G vectors is infinite and evaluating sums over all such vectors would be computationally expensive. Since orbitals and densities tend to become smooth at small scales, i.e. the plane wave components become negligible for large G vectors, therefore during calculations the infinite sums over G vectors and cells can be truncated.

2.5.2
Pseudopotentials

The most common *pseudopotential* (PP) approach is the *frozen core approximation* which is based on the fact that physical and chemical properties of crystals mostly depend on the distribution of the valence electrons. Hence the core electrons can be considered to be "frozen" while keeping intact the core electron distribution of the isolated atom in the crystal environment. In turn, the long range interactions of the core are accounted for by PPs.

Conventionally the PP is constructed by satisfying four general criteria:

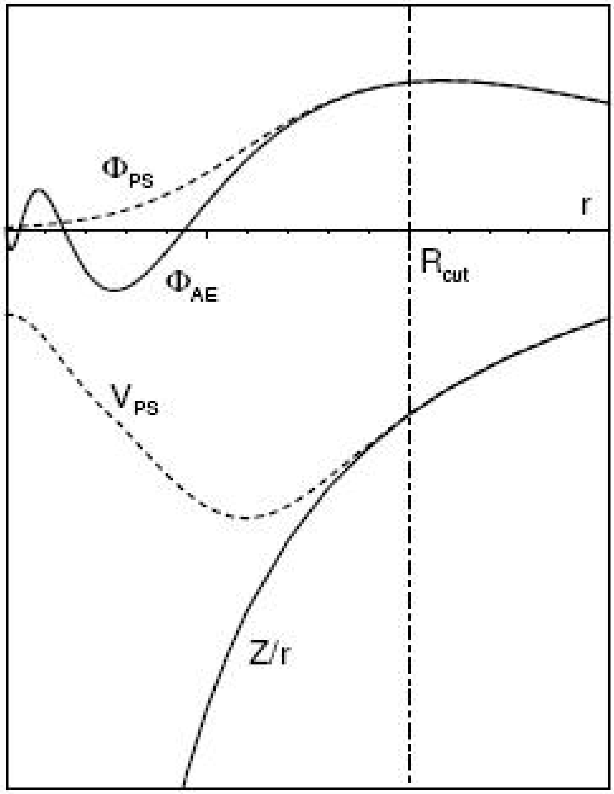

Figure 2.3 A schematic diagram of an atomic all-electronic wavefunction (solid line) and the corresponding atomic pseudo wavefunction (dashed line) together with the respective external Coulomb potential (solid line) and pseudopotential (dashed line).

(a) the valence pseudo-wavefunction Φ_l^{PS} must be the same as the all-electron (AE) wavefunction Φ_l^{AE} outside a given cut-off radius R_{cut},

(b) the charge enclosed within R_{cut} must be equal for the two wavefunctions, i.e.

$$\int_0^{R_{cut}} \left|\Phi_l^{PS}(r)\right|^2 dr = \int_0^{R_{cut}} \left|\Phi_l^{AE}(r)\right|^2 dr \qquad (2.5.7)$$

and is normalized such that

$$\int_0^{\infty} \left|\Phi_l^{PS}(r)\right|^2 dr = \int_0^{\infty} \left|\Phi_l^{AE}(r)\right|^2 dr = 1 \qquad (2.5.8)$$

This is commonly referred to as *norm-conservation*,

(c) Φ_{PS} must not have any radial nodes within the core region and,

(d) the valence AE and PP eigenvalues must be equal. These features are illustrated in Fig. 2.3.

Application of PPs has various advantages. It leads to a reduction in the number of electrons in the system and thereby allows for faster calculations and a simplified treatment of bigger systems. PPs also allow for a considerable reduction of the basis set size. The pseudized valence wavefunctions are nodeless functions and therefore require less basis functions for an accurate description. Furthermore the relativistic effects connected to the core electrons are incorporated into the PPs without complicating the calculations of the final system. Most importantly, PPs are transferable which implies that the same PP would be adequate for an atom in all possible chemical environments. This proves particularly useful during a simulation in which a change of environment is expected, such as in case of chemical reactions and phase transitions.

.

References

1. E. Schrödinger, *Ann. Phys.* **1926**, *79*, 361.
2. M. Born and J. R. Oppenheimer, *Ann. Phys.* **1927**, *84,* 457.
3. C. C. J. Roothaan, *Rev. Mod. Phys.* **1951**, *23*, 69.
4. C. Møller and M. S. Plesset, *Phys. Rev.* **1934**, *46*, 618.
5. C. D. Sherrill and H. F. Schaefer, *Adv. Quantum Chem.* **1999**, *34*, 143.
6. R. J. Bartlett, *J. Phys. Chem.* **1989**, *93*, 1697.
7. R. G. Parr and W. Yang, *Density functional theory of atoms and molecules*, Clarendon Press, New York **1989**.
8. L. H. Thomas, *Proc. Cambr. Phil. Soc.* **1927**, *23*, 542.
9. E. Fermi, *Z. Phys.* **1928**, *48*, 73.
10. P. Hohenberg and W. Kohn, *Phys. Rev.* **1964**, *136*, 864.
11. W. Kohn and L. J. Sham, *Phys. Rev.* **1965**, *140*, 1133.
12. J. P. Perdew and Y. Wang, *Phys. Rev. B* **1986**, *33*, 8800.
13. A. D. Becke, *Phys. Rev. A* **1988**, *38*, 3098.

14. J. P. Perdew, *Phys. Rev. B* **1986**, *33*, 8822.
15. J. P. Perdew and Y. Wang, *Phys. Rev. B* **1992**, *45*, 13244.
16. C. Lee, W. Yang, and R. G. Parr, *Phys. Rev. B* **1988**, *37*, 785.
17. J. P. Perdew, S. Burke, and M. Ernzerhof, *Phys. Rev. Lett.* **1996**, *77*, 3865.
18. L. Verlet, *Phys. Rev.* **1969**, *57*, 98; *Phys. Rev.* **1967**, *165*, 201.
19. R. Car and M. Parrinello, *Phys. Rev. Lett.* **1985**, *55*, 2471.
20. G. Kresse and J. Hafner, *Phys. Rev. B* **1993**, *47*, 558.
21. G. Kresse and J. Furthmüller, *Phys. Rev. B* **1996**, *54*, 11169.
22. F. Bloch, *Z. Phys.* **1928**, *52*, 555.

CHAPTER 3

Electronic structure

Love one another;
but make not a ***bond*** *of love:*
Let it rather be a moving sea
between the shores of your souls.
-Khalil Gibran

The term electronic structure refers to the energy levels of electrons and their distributions in space and momentum. Their characterization, calculation, and experimental investigations are central goals of condensed matter physics, materials science and chemistry. In this chapter we begin with a discussion of the different tools available for studying electronic structure of solids in Section 3.1. This is followed with a brief description of the computational methodology used in the work presented herein in Section 3.2. In Section 3.3 we discuss the results of our charge density, band structure, and density of states calculations of pure and Al- and Si-substituted α-, γ-, and β-MgH_2 reported in Paper II and Paper IV. Finally, the conclusions are presented in the last section.

3.1
Introduction

The key to solving the hydrogen (H_2) storage problem lies in modifying known materials in order to improve their properties and in discovering and designing new materials with specific properties. This requires a fundamental understanding of the properties of H_2 storage materials. But properties of materials, whether electrical, magnetic, or optical, are determined by their composition and structure. The structure and strength of materials are in turn governed by the type of chemical bonding existing between the atoms which can be evaluated directly from the fundamental equations for the electrons. With the advent of new algorithms and rapid advances in theory and computational technologies, electronic structure calculations can be used to model complex materials and to gain insights regarding the complex physical and chemical processes associated with the material under study.

Density functional theory (DFT) [1] which is by far the most widely used method for calculating the ground state properties of solids, surfaces, and nanostructures, has been already discussed in Chapter 2. These calculations provide detailed information regarding the electron density, band structure and density of states (DOS) which can be used as analysis tools for studying the electronic structure of solids.

The nature of a chemical bond, that is if it is ionic or covalent, can be understood from an analysis of the *charge density distribution* in real space. In an ionic bond electrons are transferred from one atom to the other depending upon the electronegativity difference between the two atoms, while in a covalent bond the atoms share electrons because of their similar electron affinities. When the total charge density is concentrated around the atoms without any interaction between the atoms, it gives rise to a picture of ionic bonding. In the scenario where there is concentration of electrons in the regions between nearest neighbour atoms, it can be interpreted as a covalent bond.

The electrons of a single isolated atom occupy atomic orbitals, which form a discrete set of energy levels. If several atoms are brought together into a molecule,

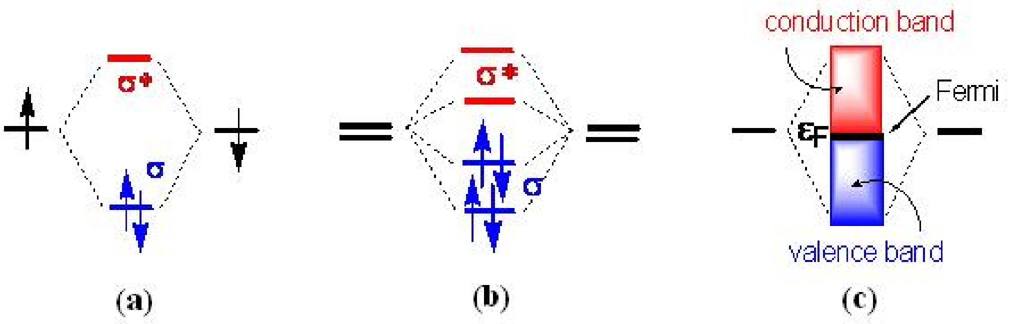

Figure 3.1 Electronic structures of (a) Li_2 molecule, (b) Li_4 cluster, and (c) solid containing N_A Li atoms.

their atomic orbitals split producing a number of molecular orbitals proportional to the number of atoms. The electronic structure of solids can also be described by molecular orbital theory where the solid can be considered as a supermolecule with N_A Avogadro number of atoms. As a result the number of orbitals now becomes very large, and the difference in energy between them becomes very small, so the levels may be considered to form continuous *bands* of energy rather than discrete energy levels of the atoms in isolation. However, some intervals of energy contain no orbitals, no matter how many atoms are aggregated, forming band gaps. See Figs. 3.1 (a)-(c) for the evolution of the electronic band structure of a solid.

For a one-dimensional crystal consisting of equally spaced n = 1 to N hydrogen atoms, the crystal orbitals are described as Bloch sums going over all atomic orbitals,

$$\psi(k) = \sum_{n=1}^{N} e^{ikna}\phi_n \quad \text{with} \quad 0 \le |k| \le \frac{\pi}{a} \tag{3.1.1}$$

At k = 0, 2π/a, 4π/a...

$$\psi(0) = \sum_{n=1}^{N} \phi_n = \phi_1 + \phi_2 + \phi_3 + \phi_4 + \phi_5 \cdots \tag{3.1.2}$$

and for k = π/a, 3π/a, 5π/a....

$$\psi(\frac{\pi}{a}) = \sum_{n=1}^{N} e^{i\pi n}\phi_n = -\phi_1 + \phi_2 - \phi_3 + \phi_4 - \phi_5 \ldots \qquad (3.1.3)$$

Energies of these crystal orbitals, that is, the *band structure*, can be evaluated as follows by using the Hamiltonian

$$E(k) = \frac{\langle \psi(k)|H|\psi(k)\rangle}{\langle \psi(k)|\psi(k)\rangle} \qquad (3.1.4)$$

The above band structure is displayed in Fig. 3.2 for different H-H distances. As there is only one atomic orbital per unit cell, there is only one band. It can be seen that as the H-H distance decreases the band becomes steeper. This is so because band dispersion is proportional to the atom-atom interaction between unit cells, which in turn is proportional to the overlap integral and the overlap integral approximately decreases with interatomic distance.

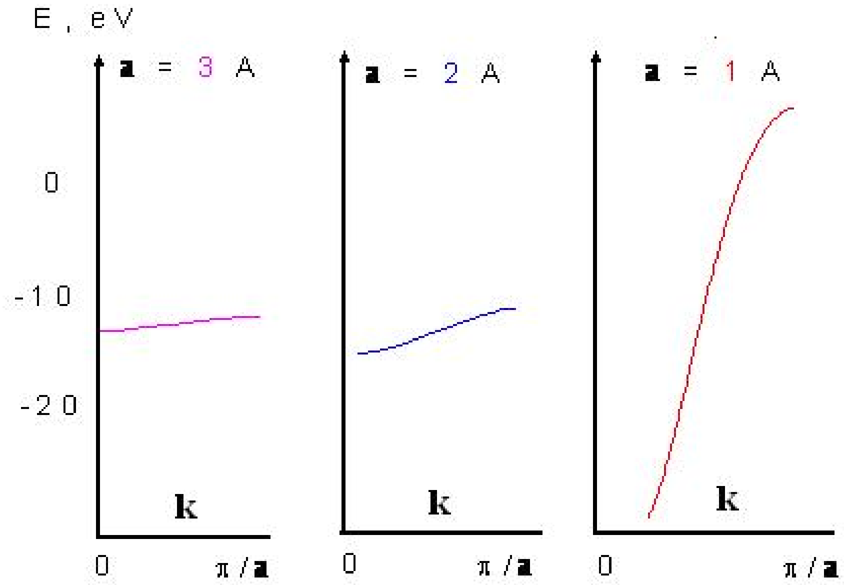

Figure 3.2 Band structures of a one-dimensional chain of hydrogen atoms with H-H distances of 3 Å, 2 Å, and 1 Å, respectively.

As one moves to more complex systems and higher dimensions, band structure calculations and their analysis becomes increasingly challenging due to the **k**-dependence of the crystal orbitals ψ(**k**) which keeps us in the reciprocal space. There can be several band structures depending upon the route followed through the *Brillouin zone (BZ)*. Furthermore, as ψ(**k**) can assume complex values, constructing real linear combinations from sets of degenerate ψ(**k**)s to sketch the band structure in terms of orbital icons is technically difficult. Hence, a tool which brings us back into the real space and one which averages over the entire system is needed for being able to appropriately study the electronic structure of solids.

Density of states (DOS) is one such approach. DOS is simply the reciprocal gradient of the band structure. For a one-dimensional case, it is defined as

$$P(E) \sim \left(\frac{dE}{dk}\right)^{-1} \sim v(k)^{-1} \qquad (3.1.5)$$

This implies that the steeper a band, wider will be the DOS. DOS is also inversely proportional to the velocity v of an electron in a band. Thus, a wide DOS is suggestive of a rapidly moving electron due to strong coupling between the atoms.

To sketch the DOS plots Schrödinger's k-dependent equation is evaluated for all representative **k** points in the three-dimensional BZ. In the tetrahedron method [2], used in the work presented in this chapter, the entire BZ is divided into a number of small tetradehra and then the energy eigenvalues are obtained as a histogram for all the **k** points. Once the DOS is plotted graphically, insights into the electrical and optical properties of the material under investigation can be easily gained. A vanishing band gap and finite DOS implies metallic conduction, a small band gap (~1.0 eV) is indicative of semiconducting behaviour and a large band gap of many eV tells that the material will act as an insulator. The magnitude of the band gap will also tell whether the material will be transparent or not.

Stimulated by the usefulness of the analytical tools described so far, we performed in Papers II and IV charge density, band structure and DOS calculations for pure and Al- and Si-doped α-, γ-, and β-MgH_2 in order to develop an understanding of the effect of these dopants on the stability and dehydrogenation reactions of these three phases of MgH_2.

3.2
Computational details

For our calculations we used periodic DFT within the generalized gradient approximation (GGA) [3] as implemented in the Vienna *ab initio* simulations package (VASP). [4,5] Projector augmented waves (PAWs) [6,7] and plane-wave basis sets as provided with VASP were employed. We used a cut-off energy of 440 eV for the plane-wave basis set.

α-MgH_2 is known to crystallize with TiO_2-rutile type structure at ambient pressure and low temperature [8,9]. At higher temperatures and pressures, it transforms into orthorhombic γ-MgH_2. [10] In 2006 experiments were able to confirm the occurrence of the subsequent γ to β phase transition at still higher pressures. [11] β-MgH_2 has a modified CaF_2 structure. To simulate the Al- and Si-substituted systems, we considered 4 x 2 x 2 and 2 x 2 x 2 supercells of α-MgH_2 and 2 x 2 x2 supercells of γ- and β-MgH_2. The 2 x 2 x 2 supercells have lattice constants that are double those of the corresponding unit cells. The 4 x 2 x 2 supercell of α-MgH_2 was built by further stacking the 2 x 2 x 2 supercell along the *a*-axis. These pure hydride supercells will be referred to as α-$Mg_{16}H_{32}$, α-$Mg_{32}H_{64}$, γ-$Mg_{32}H_{64}$, and β-$Mg_{32}H_{64}$, respectively. Fractions $x = 0.0625$ and 0.03125 of Al and Si were introduced in α-MgH_2 by replacing one Mg atom out of a total 16 and 32 Mg atoms in the 2 x 2 x 2 and 4 x 2 x 2 supercells by one Al or Si atom. These substituted α-MgH_2 supercells are represented as α-$Mg_{15}H_{32}X$ and α-$Mg_{31}H_{64}X$ respectively. Similarly fraction $x = 0.03125$ of Al and Si is generated in γ- and β-MgH_2 by replacing one Mg atom out of the total 32 Mg atoms in their 2 x 2 x 2 supercells with one X = Al or Si atom and these doped phases will be referred to as γ-$Mg_{31}H_{64}X$ and β-$Mg_{31}H_{64}X$, respectively.

The above resulting geometries were subsequently optimized by force and stress minimization. Ionic relaxation was performed until the force on each atom became less than 0.5 meV $Å^{-1}$. A criterion of 0.1 meV was placed on the self-consistent convergence of the total energy. The reciprocal space sampling for the supercells was done with a 4 x 4 x 4 Monkhorst–Pack **k**-point grid [12]. The optimized structures of α-$Mg_{31}H_{64}X$, γ-$Mg_{31}H_{64}X$ and β-$Mg_{31}H_{64}X$ corresponding to the fraction x = 0.03125 of doping are shown in Figs. 3.3 (a)-(c).The total charge density isosurfaces were generated using Vaspview [13] and the difference total charge density contour plots were produced using XcrySDen [14]. The band structures of the pure and Al- and Si-doped α-MgH_2 were plotted along the G-X-M-G-Z-R-A-Z path [15,16] in the first brillouin zone. For obtaining the DOS we the tetrahedron method [2] was employed along with a 6 x 6 x 6 **k**-point grid.

3.3
Results and discussion

3.3.1
Charge density

In this section we discuss the charge distribution in both pure and Al- and Si-substituted α-, γ-, and β-MgH_2. On the Pauling scale, H has a high electronegativity of 2.20 and Mg has a comparatively low electronegativity of 1.3. This implies atomic H has a better ability to attract electrons than atomic Mg. We therefore expect Mg to be present as Mg^{2+} ions and H as H^- ions in the pure MgH_2 phases. The iso-surface total charge densities of α-$Mg_{32}H_{64}$, γ-$Mg_{32}H_{64}$ and β-$Mg_{32}H_{64}$ plotted at an iso-value which is at least 1/10th of the maximum charge density are displayed in Figs. 3.4 (a)-(c). The figures clearly show that even at such small iso-values, the charge density is localized around H atoms only, while all the Mg atoms are left completely bare. This picture reaffirms the suspected ionic character of the three pure MgH_2 phases.

Hydrides of Al and Si (AlH_3 and SiH_4) are well-known covalent compounds. Even in complex metal aluminium hydrides, such as Li_3AlH_6 and Na_3AlH_6, the Al-H

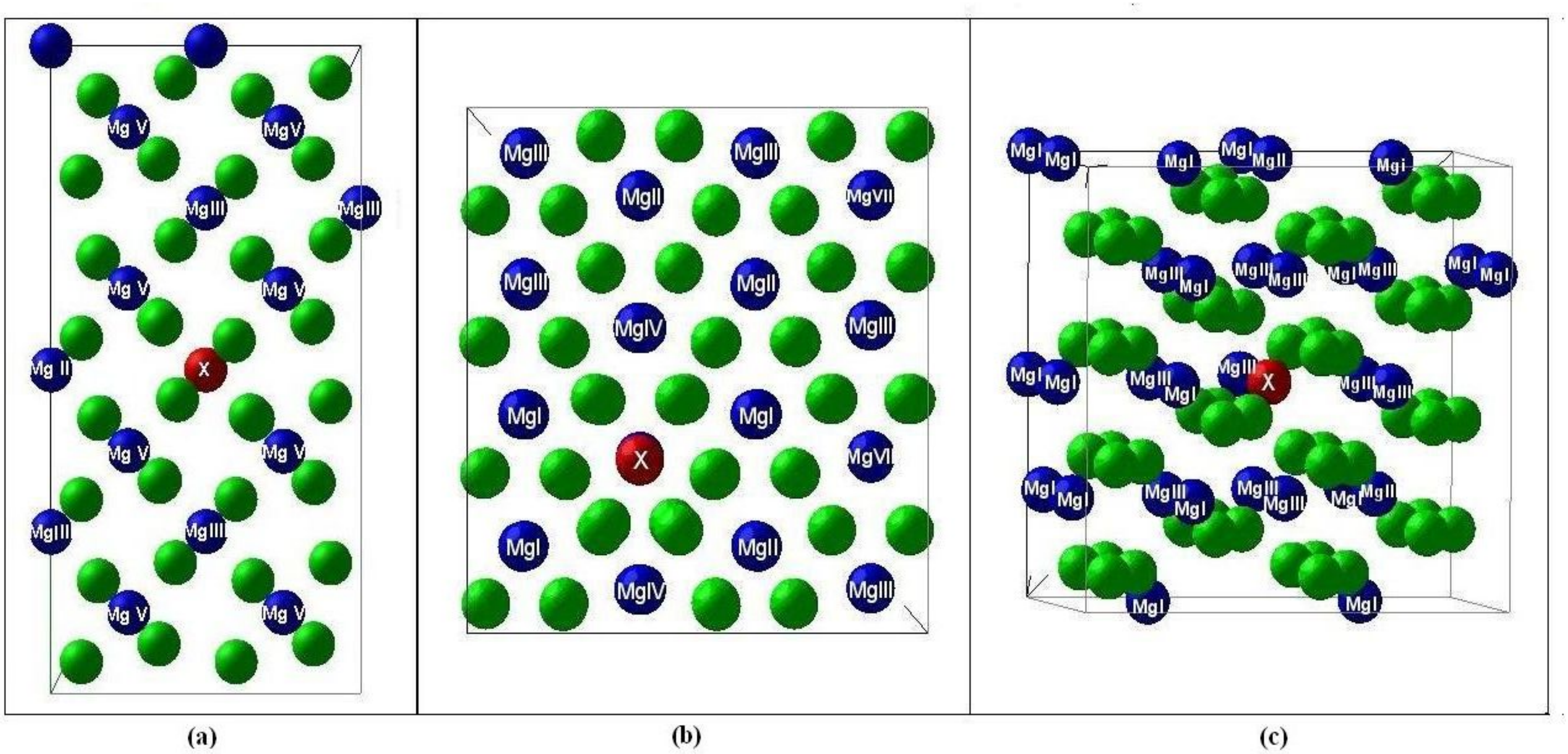

(a) (b) (c)

Figure 3.3 Structures of the optimized geometries of (a) α-$Mg_{31}H_{64}X$, (b) γ-$Mg_{31}H_{64}X$, and (c) $Mg_{31}H_{64}X$, where X = Al or Si, and the inequivalent Mg atoms therein. The green spheres are H atoms.

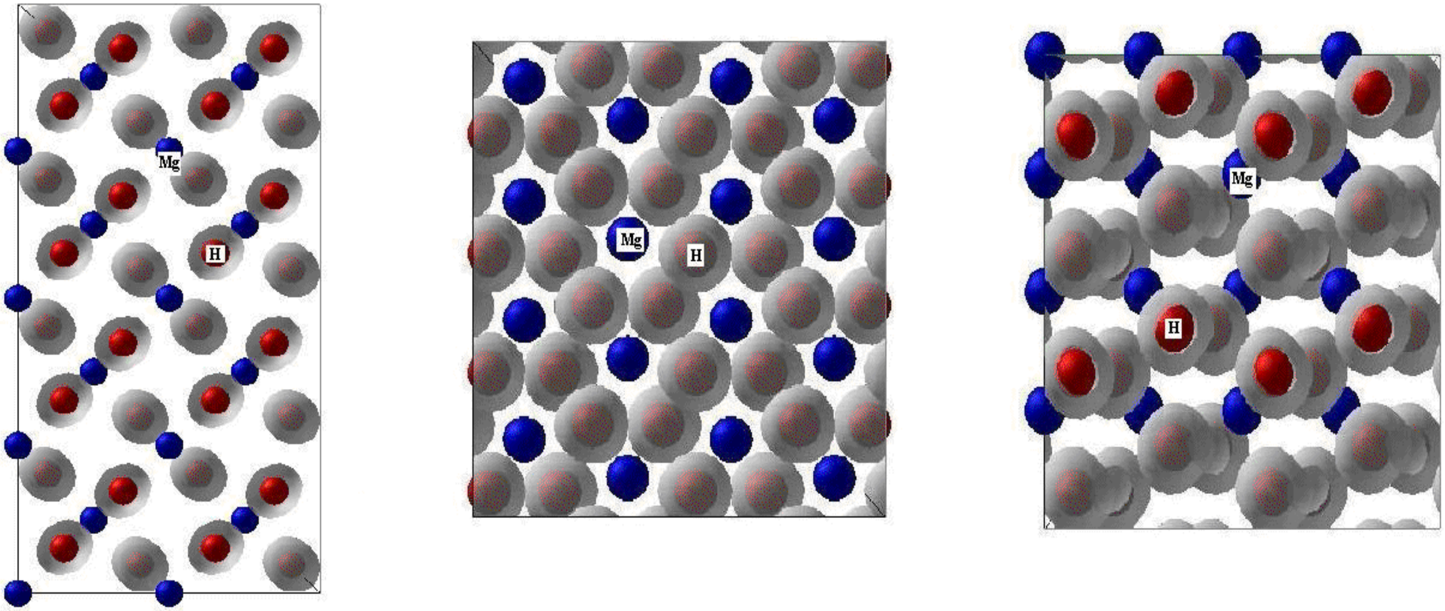

(a) α-$Mg_{32}H_{64}$ (b) γ-$Mg_{32}H_{64}$ (c) β-$Mg_{32}H_{64}$

Figure 3.4 Total charge density iso-surface plots of (a) α-$Mg_{32}H_{64}$ at iso-value = 82.5, (b) γ-$Mg_{32}H_{64}$ at iso-value = 165.4, (c) β-$Mg_{32}H_{64}$ at iso-value = 140.6. All iso-values are ~ 1/10 maximum charge density.

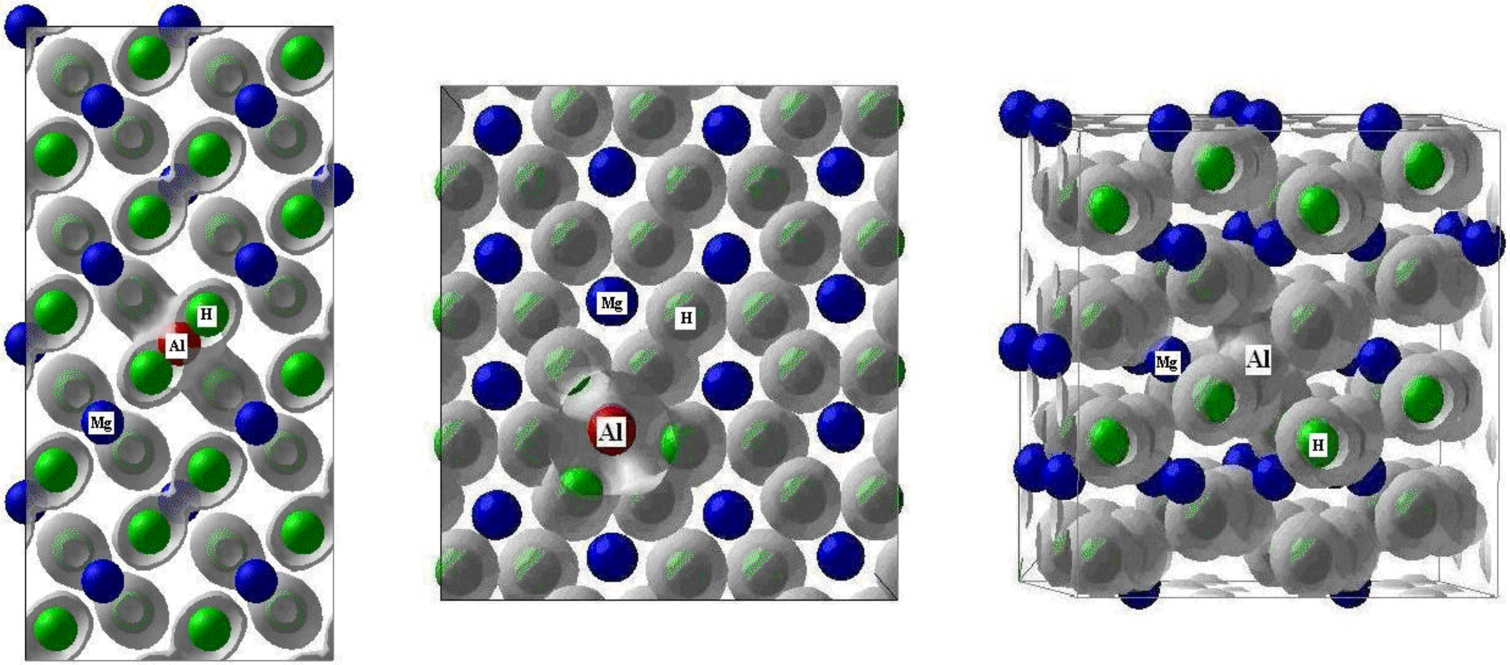

(a) α -$Mg_{31}H_{64}Al$ (b) γ -$Mg_{31}H_{64}Al$ (c) β -$Mg_{31}H_{64}Al$

Figure 3.5 Total charge density iso-surface plots of (a) α-$Mg_{31}H_{64}Al$ at iso-value = 70.13, (b) γ-$Mg_{31}H_{64}Al$ at iso-value = 170.5, and (c) β-$Mg_{31}H_{64}Al$ at iso-value = 134.5. All iso-values are ~ 1/10 maximum charge density.

bonds in the octahedral $[AlH_6]^{3-}$ units exhibit covalent interaction. [17,18] Further, the electronegativity values of Al and Si (1.61 and 1.90 on the Pauling scale) are greater than that of Mg, but less than that of H. Thus, we anticipate that like H, Al and Si will have an affinity for electrons and we envisage bonding between Al or Si and H to be covalent rather than ionic.

The iso-surface total charge density plots of Al-substituted phases represented as α-$Mg_{31}H_{64}Al$, γ-$Mg_{31}H_{64}Al$, and β-$Mg_{31}H_{64}Al$ at iso-values 1/10th of maximum charge density are illustrated in Figs. 3.5 (a)-(c). The figures show that, while Mg continues to be bereft of charge density, there is a strong directional electron density along the neighbouring Al-H bonds. This exhibits that the interaction between Mg and H continues to remains ionic but the bonding between Al and H atoms is covalent in nature. The iso-surface total charge density plots of α-$Mg_{31}H_{32}Si$, γ-$Mg_{31}H_{64}Si$, and β-$Mg_{31}H_{64}Si$ exhibit similar features and so are not displayed here.

In order to develop a greater insight regarding the effect of Al and Si insertion in MgH_2, we calculated the difference between total charge densities of α-$Mg_{15}H_{32}X$ (X=Al, Si) and α-$Mg_{16}H_{32}$ which were then plotted in the form of contours in the range -0.1 to +0.15 in a plane parallel to the (001) surface. These contours are displayed in Figs. 3.6 (a) and (b), where the white areas correspond to regions of

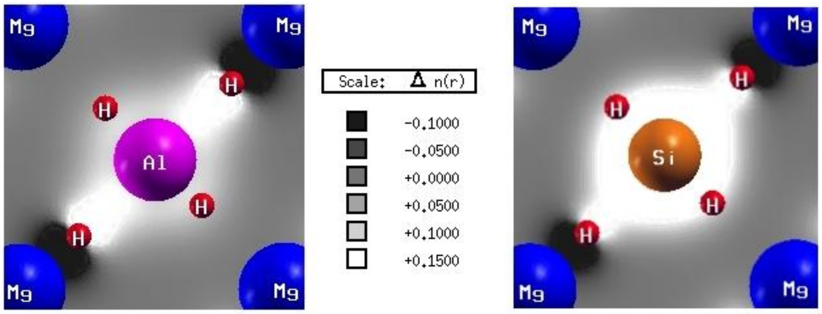

(a) (b)

Figure 3.6 Contour plots of the difference between total charge densities of a) α-$Mg_{15}H_{32}Al$ and α-$Mg_{16}H_{32}$, and b) α-$Mg_{15}H_{32}Si$ and α-$Mg_{16}H_{32}$ in the range -0.1 to 0.15 plotted in a cross-section parallel to the (001) plane. The Mg atoms at the corners belong to the (001) plane.

electron gain, and the black areas imply regions of electron loss relative to the pure α-MgH_2 phase. It can be seen that there is a substantial increase in electron density along the Al-H and Si-H bonds. There is, however, a difference in the way in which electron density is directed in the two contour plots. The electron gain around Al is much less than around Si, with the concomitant increase in electron density occurring to a greater extent around the H atoms of the Al-H bonds than around those of the Si-H bonds. This indicates that the sharing of electron density along the X-H bonds is equal between Si and H and unequal between Al and H.

3.3.2
Band structure

To understand the effect of the inclusion of Al and Si on the electronic structure of α-MgH_2 we analyzed their band structures. The overall band structure of α-$Mg_{16}H_{32}$ is shown in Fig. 3.7 (a). α-$Mg_{16}H_{32}$ contains 64 valence electrons which occupy the 32 valence bands (VBs) completely, leaving the conduction bands (CBs) empty. The band structure shows that the VB has a width of about 6.5 eV and exhibits two major peaks at about 1.5 and 2.5 eV. The CB is at an energy gap of 3.9 eV from the VB. This calculated band gap agrees well with earlier theoretical studies reporting it as 4.2 eV [19] and 3.78 eV [20]. The large band gap implies that α-MgH_2 is an insulator. However, a so-called band gap problem is associated with DFT–GGA calculations. In this, the band gap calculated from GGA eigenvalues in the Kohn–Sham theory always underestimates the true band gap due to the discontinuity of exchange-correlation potentials. Most of this difference between Kohn–Sham eigenvalues and true excitation energies can be amended by a rigid shift of the conduction band with respect to the valence band. This upward shift would bring the calculated band gap closer to the experimental band gap (5.6±0.1 eV [21] and 5.16 eV [22]).

The band structure of α-$Mg_{15}H_{32}Al$ is displayed in Fig. 3.7 (b). The pattern of both VB and CB is similar to that of α-$Mg_{16}H_{32}$. Unlike $Mg_{16}H_{32}$, the calculated energy gap is zero. This is probably because α-$Mg_{15}H_{32}Al$ contains 65 valence electrons, of which 64 occupy the 32 VBs, while the last electron goes into the CB minimum thus making Al-substituted α-MgH_2 metallic. Due to the easy transfer-

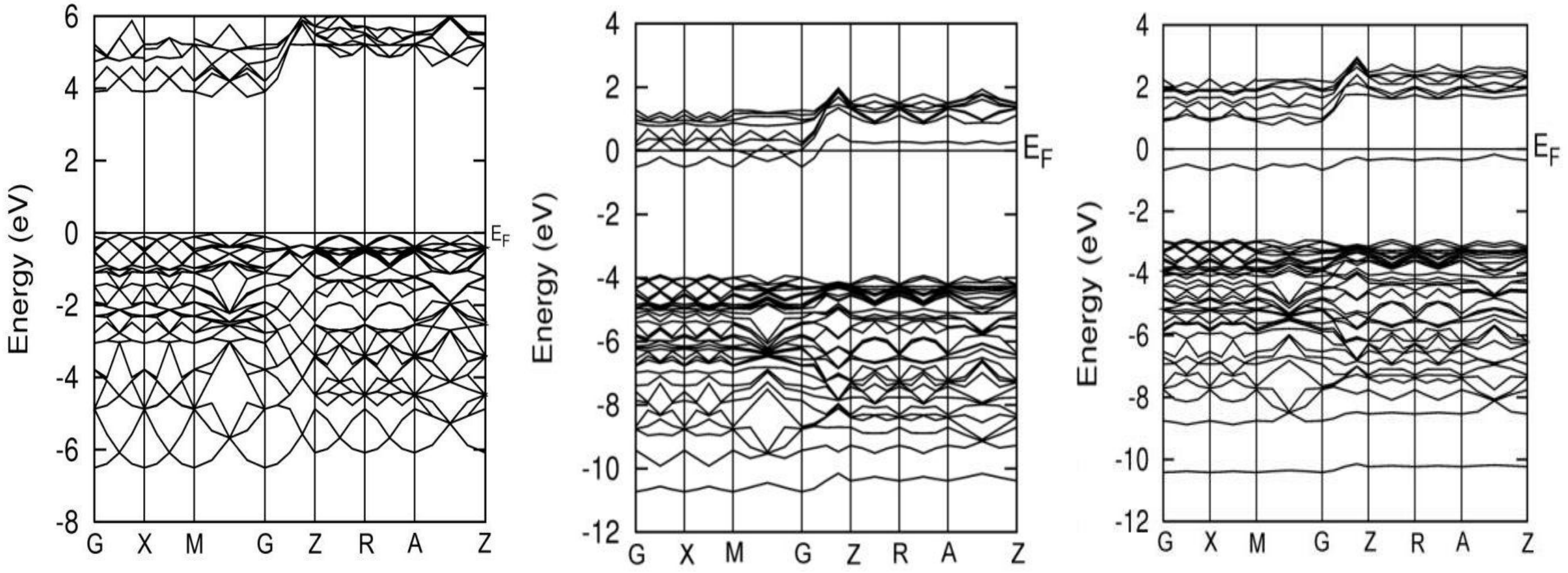

(a)

(b)

(c)

Figure 3.7 Band structures of (a) α-$Mg_{16}H_{32}$, (b) α-$Mg_{15}H_{32}Al$, and (c) α-$Mg_{15}H_{32}Si$ plotted along the G-X-M-G-Z-R-A-Z path in the first Brillouin zone. The zero line corresponds to E_F.

ability and mobility of the valence electrons in the CB, we expect the Mg-H bond to be more susceptible to dissociation in the presence of Al.

Figure 3.7 (c) shows the band structure of α-$Mg_{15}H_{32}Si$. It can be seen that an additional band is generated inside the band gap of pure α-MgH_2. As a result, the band gap decreases from 3.9 eV to 0.9 eV, making α-$Mg_{15}H_{32}Si$ conducting. However, it will not exhibit metallic conduction, because in contrast to α-$Mg_{15}H_{32}Al$, the valence electrons are not found in the CB.

Due to the band gap problem, an upward shift of the conduction band may be required to obtain the true band gaps of α-$Mg_{15}H_{32}Al$ and α-$Mg_{15}H_{32}Si$. This would then place both Al- and Si-substituted α-MgH_2 in the semiconductor category. However, their band gaps would still be smaller in magnitude compared to that of the pure hydride and, hence, would cause the substituted systems to be more susceptible to Mg-H bond dissociation.

3.3.3
Density of states

Herein we present a detailed DOS analysis of the pure and Al- and Si-doped α-, γ-, and β-MgH_2. The total DOS of the three pure MgH_2 phases: α-$Mg_{32}H_{64}$, γ-$Mg_{32}H_{64}$ and β-$Mg_{32}H_{64}$ are displayed in Figs. 3.8 (a)-(c). From these figures it is noticeable that the valence band (VB) and the conduction band (CB) in α-, γ-, and β-MgH_2 are separated by a band gap of 3.9 eV, 3.8 eV, and 2.5 eV respectively. Thus all the three phases are correctly predicted to behave as insulators. The following order of band gaps exists: pure β-MgH_2 < pure γ-MgH_2 ~ pure α-MgH_2. Hence we expect pure β-MgH_2 to be require less energy for H_2 removal than pure α- or γ-MgH_2 as its corresponding energy needed to excite an electron into the CB for destabilizing the Mg-H bond will be least due to the small magnitude of its band gap.

The partial DOS of pure α-, γ-, and β-MgH_2, which are also presented in Figs. 3.8 (a)-(c), illustrate that in the three hydrides the VB arises from *s, p* and *d* electrons of Mg and *s* electrons of H, while the CB is a purely Mg state formed from the empty *s*, *p* and *d* states of Mg alone.

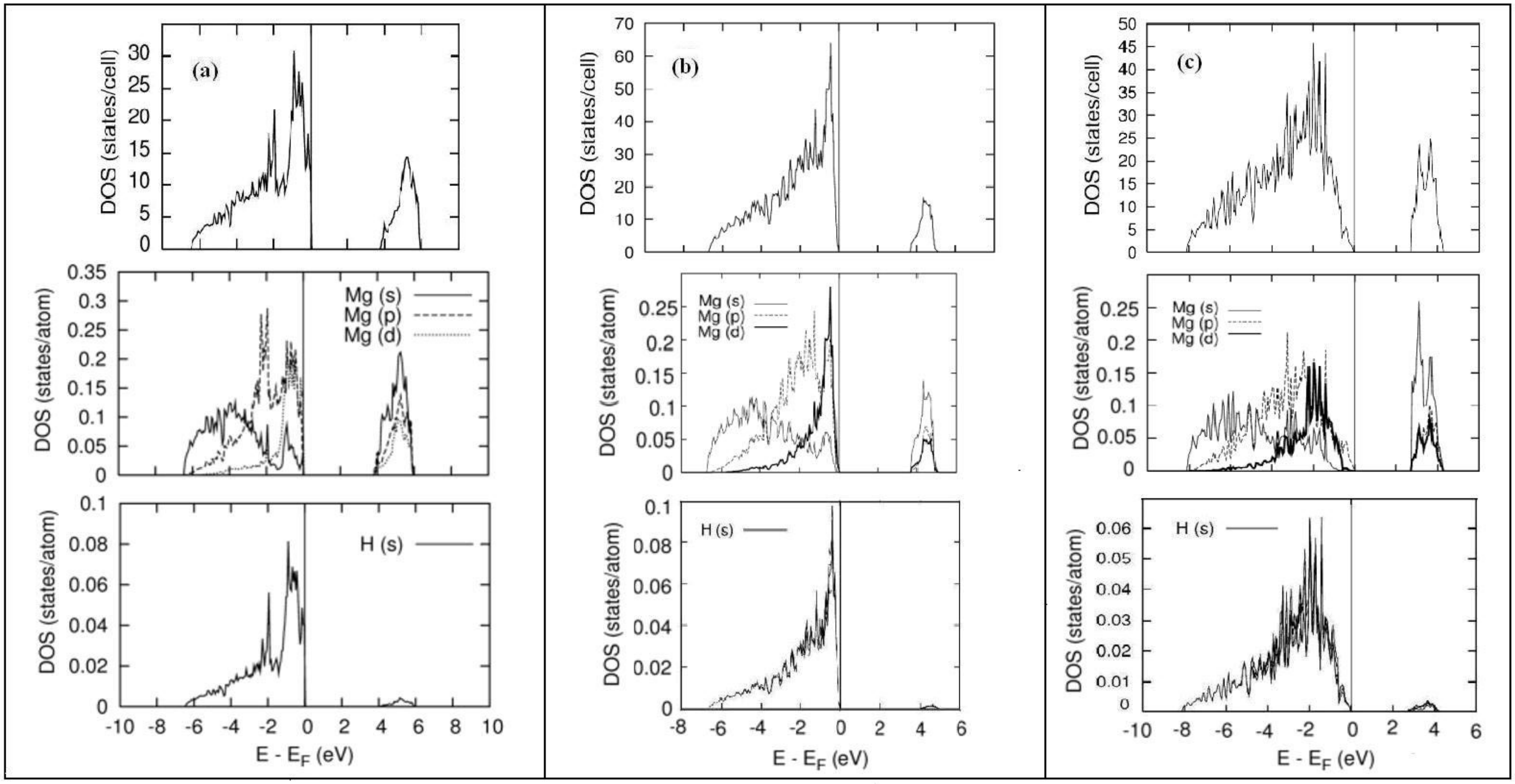

Figure 3.8 Total and partial density of states plots of pure (a) α-$Mg_{32}H_{64}$, (b) γ-$Mg_{32}H_{64}$, and (c) β- $Mg_{32}H_{64}$. Here the energy is set to zero at E_F.

In the supercells of pure α-, γ-, and β-MgH_2 by virtue of symmetry all Mg atoms and all H atoms exhibit similar DOS. This symmetry is disturbed on insertion of an Al or Si atom in place of a Mg atom. Significantly different DOS are generated as a result of the loss of equivalency. These five sets of inequivalent Mg atoms in α-$Mg_{31}H_{64}X$, six sets of inequivalent Mg atoms in γ-$Mg_{31}H_{64}X$ Mg atoms, and three sets of inequivalent Mg atoms in β-$Mg_{31}H_{64}X$ (where X = Al or Si) identified on the basis of DOS plots have been labelled using Roman numerals in Figs. 3.3 (a)-(c).

The total DOS of α-$Mg_{31}H_{64}Al$, γ-$Mg_{31}H_{64}Al$, and β-$Mg_{31}H_{64}Al$ are displayed in Figs. 3.9, 3.11, and 3.13, respectively. It is clearly seen from these figures that a zero band gap is predicted for all the Al-doped MgH_2 phases. α-$Mg_{31}H_{64}Al$, γ-$Mg_{31}H_{64}Al$, and β-$Mg_{31}H_{64}Al$ have a total of 129 valence electrons, each having one additional valence electron than its undoped counterpart. The VB of these systems remain doubly occupied as in case of the corresponding pure hydride phases, with the 129th electron entering the CB minimum causing band gaps to become zero. Hence, we expect a shift from insulating properties to metallic conduction in α-, γ-, and β-MgH_2 due to Al doping. Furthermore due to the easy mobility of the valence electron in the CB we anticipate that breaking the Mg-H bond would be much easier in these Al-doped MgH_2 phases.

The partial DOS of Al and selected Mg atoms of α-$Mg_{31}H_{64}Al$, γ-$Mg_{31}H_{64}Al$, and β-$Mg_{31}H_{64}Al$ are also presented in Figs. 3.9, 3.11, and 3.13 (a), respectively. In α-$Mg_{31}H_{64}Al$, the bottom region of VB from -10.0 eV to -12.0 eV is formed from *s* electrons of Al and s and *p* electrons of Mg-IV. As earlier in case of pure α-MgH_2 the VB region extending from -4.0 eV to -10.0 eV is formed from *s*, *p* and *d* electrons of all Mg and *s* electrons of H. But now it also has contributions from *s*, *p* and *d* electrons of Al. The occupied states extending from the Fermi level E_F to -0.5 eV arise from both *s* electrons of Al and Mg-IV atoms. The empty *s*, *p* and *d* states of all Mg atoms and empty *s* and *p* states of Al contribute to the CB region (2.0 eV to E_F). In γ-$Mg_{31}H_{64}Al$ (β-$Mg_{31}H_{64}Al$) the bottom region of VB from -10.5 eV to -11.0 eV is formed from *s* electrons of Al and of Mg-I and Mg-IV (Mg-II and Mg-IV) atoms. The VB region extending from -3.8 eV to -10.2 eV (-2.8 eV to-10.4 eV) is formed from *s* electrons of H, *s*, *p* and *d* electrons of Mg and *s*, *p* and *d* electrons of Al. The occupied

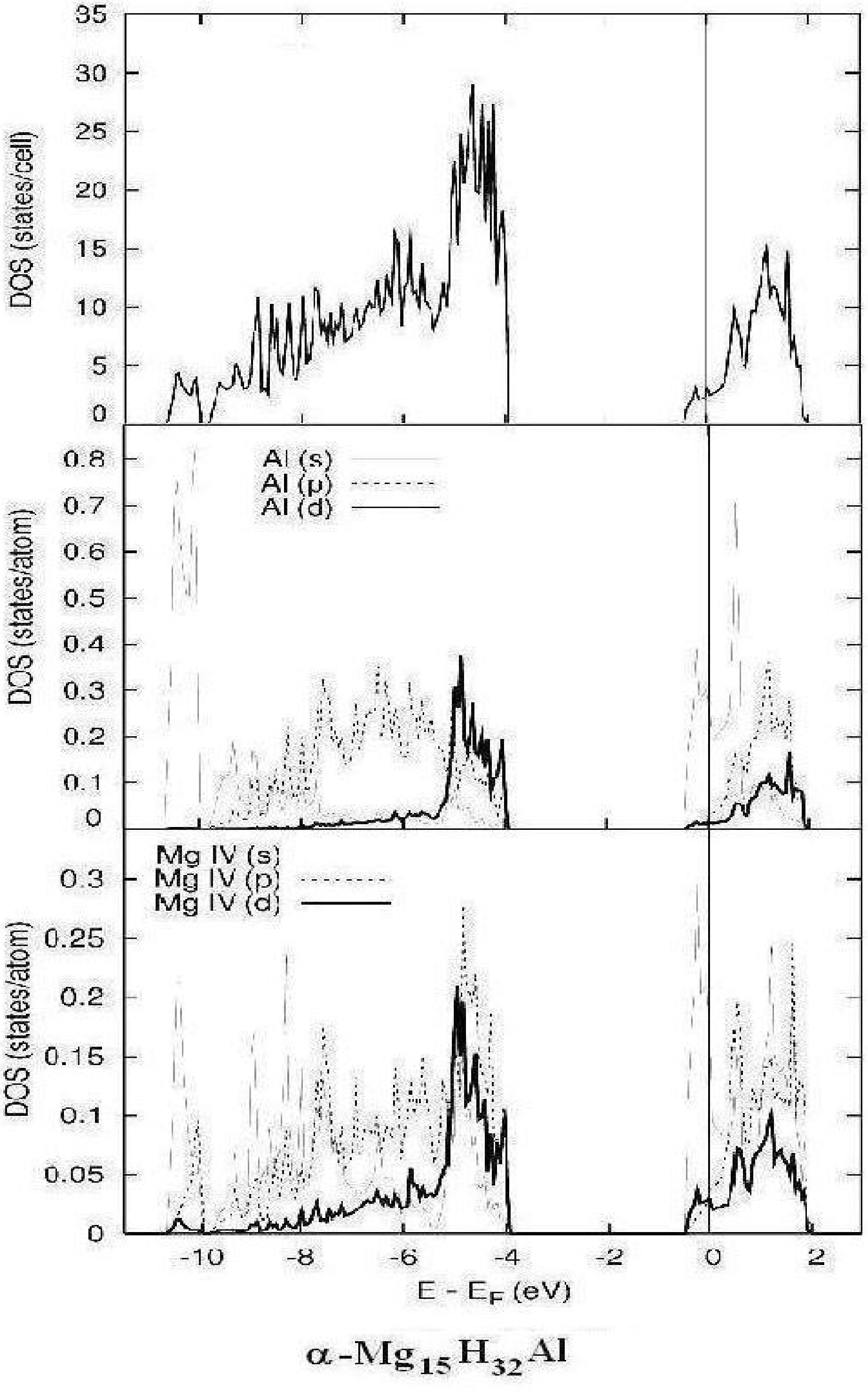

Figure 3.9 Total and partial density of states plots of α-$Mg_{31}H_{64}Al$. The energy is set to zero at E_F.

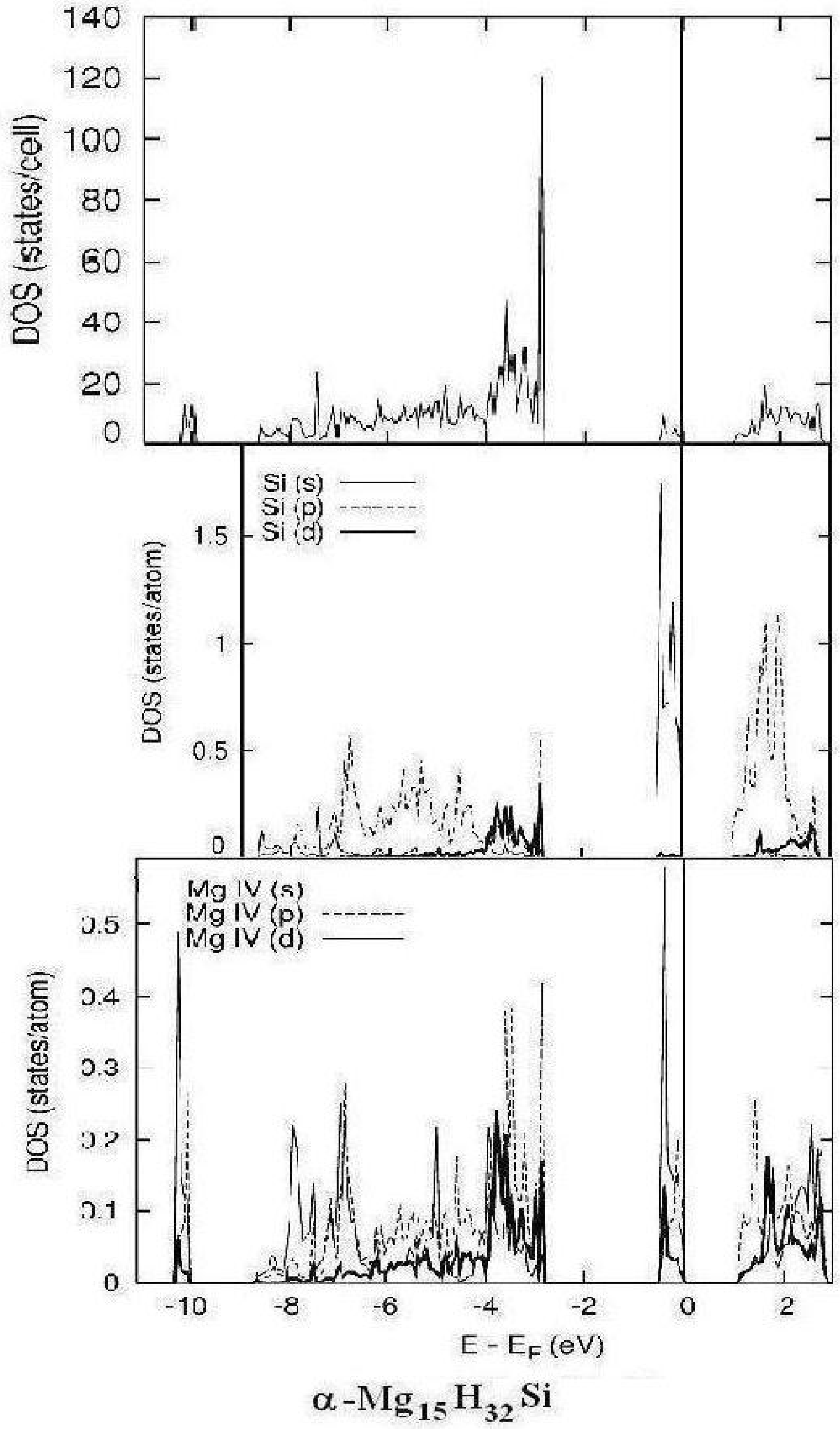

Figure 3.10 Total and partial density of states plots of α-$Mg_{31}H_{64}Si$. The energy is set to zero at E_F.

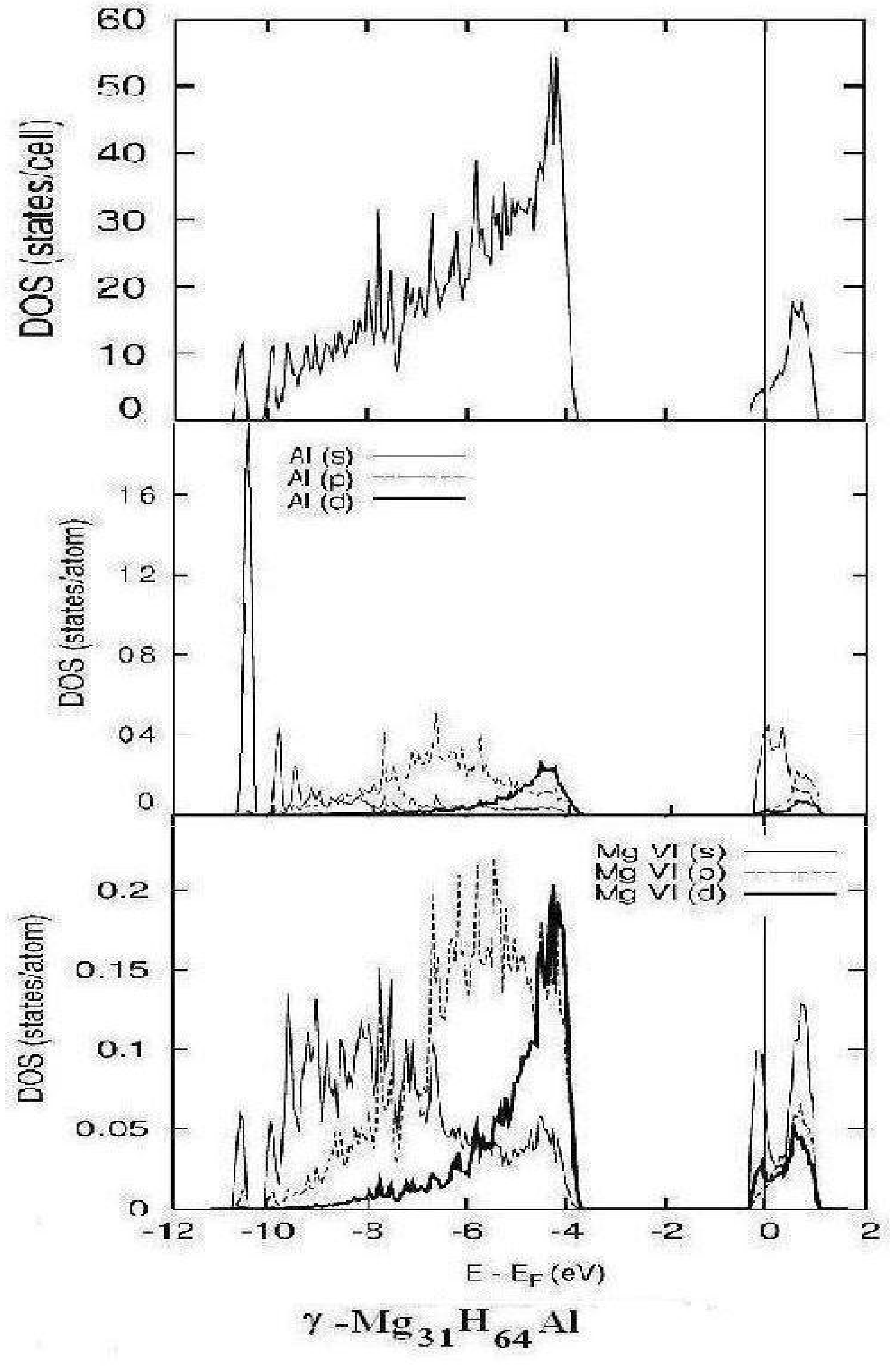

Figure 3.11 Total and partial density of states plots of γ-$Mg_{31}H_{64}Al$. The energy is set to zero at E_F.

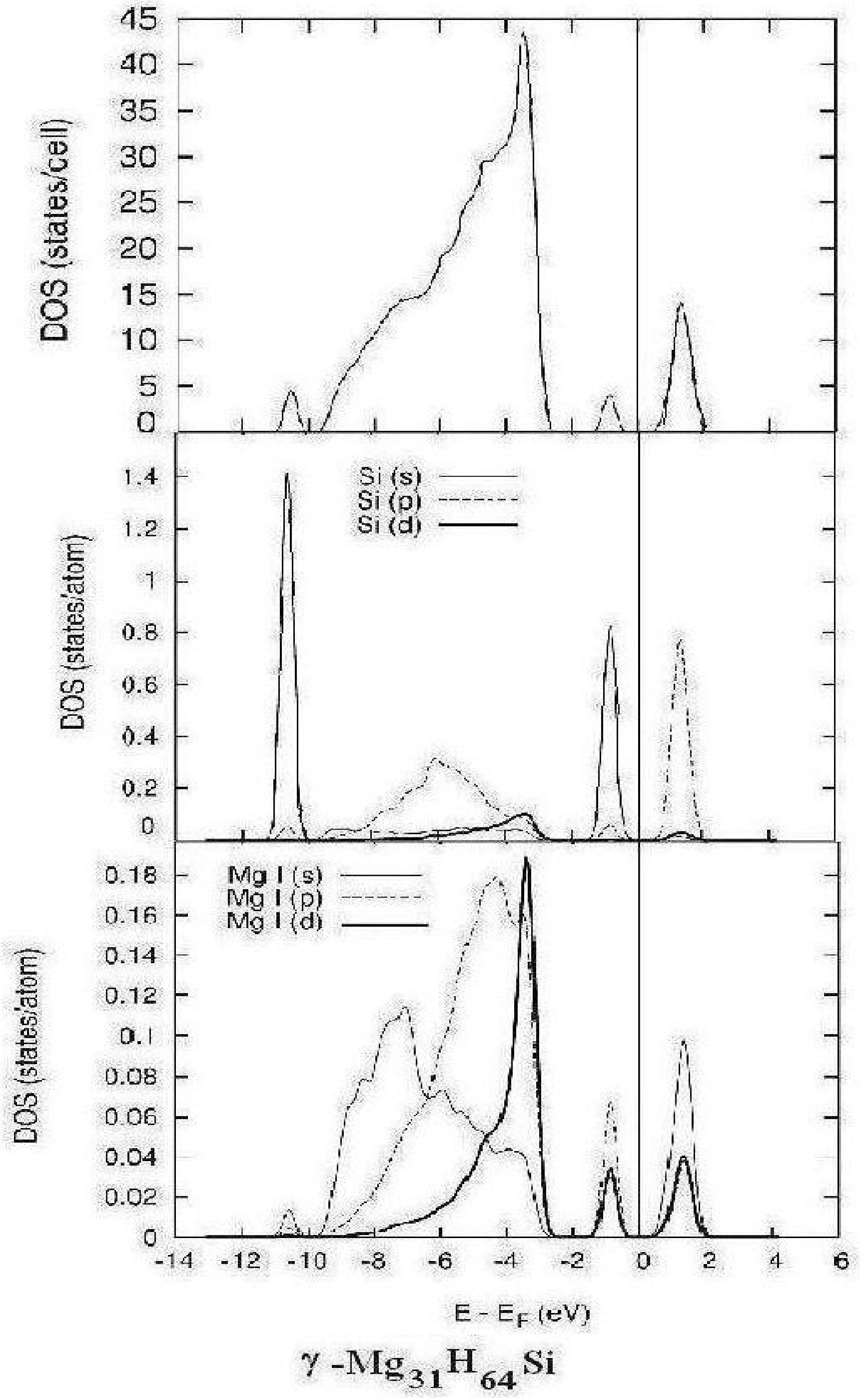

Figure 3.12 Total and partial density of states plots of γ-$Mg_{31}H_{64}Si$. The energy is set to zero at E_F.

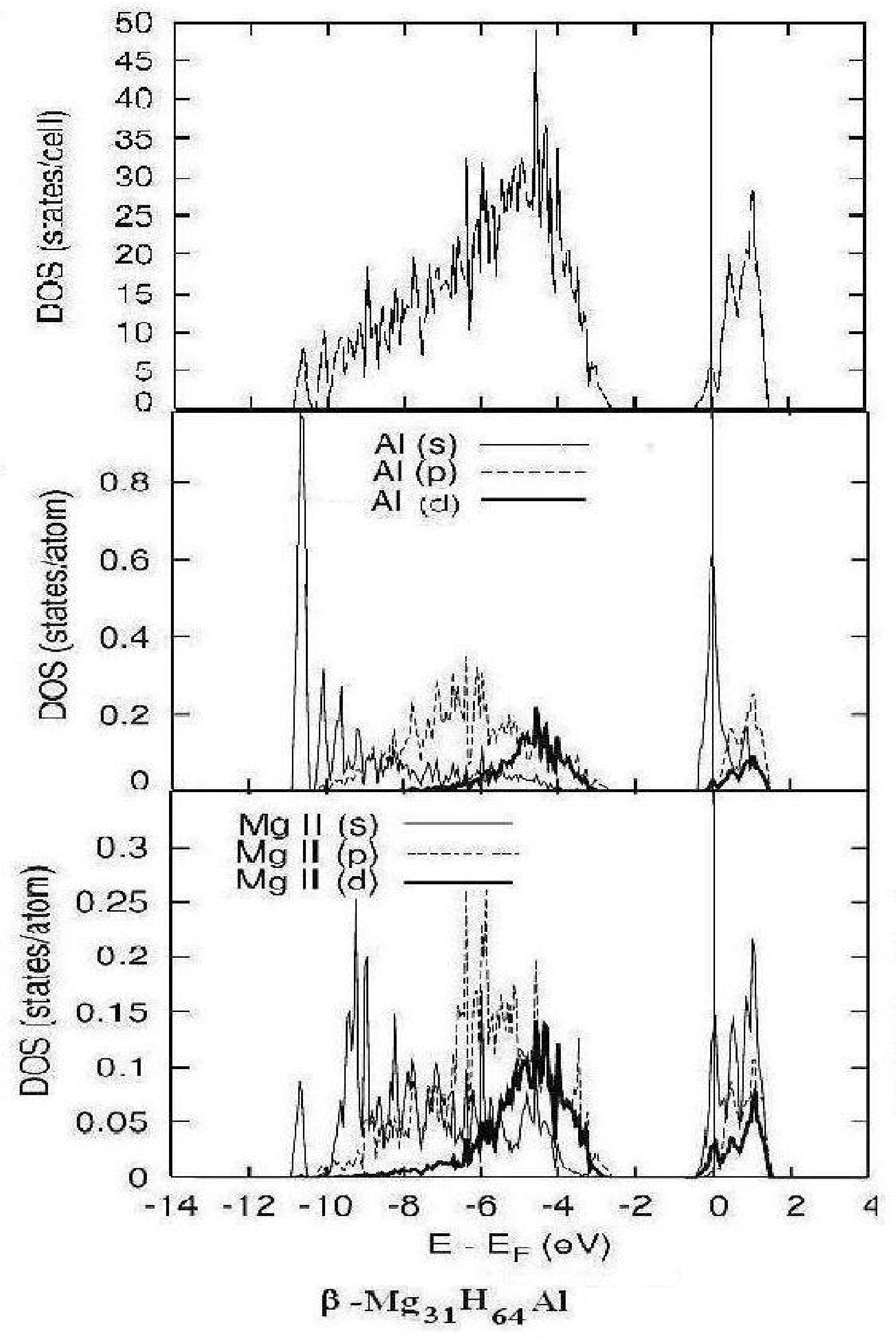

Figure 3.13 Total and partial density of plots of β-$Mg_{31}H_{64}Al$.
The energy is set to zero at E_F.

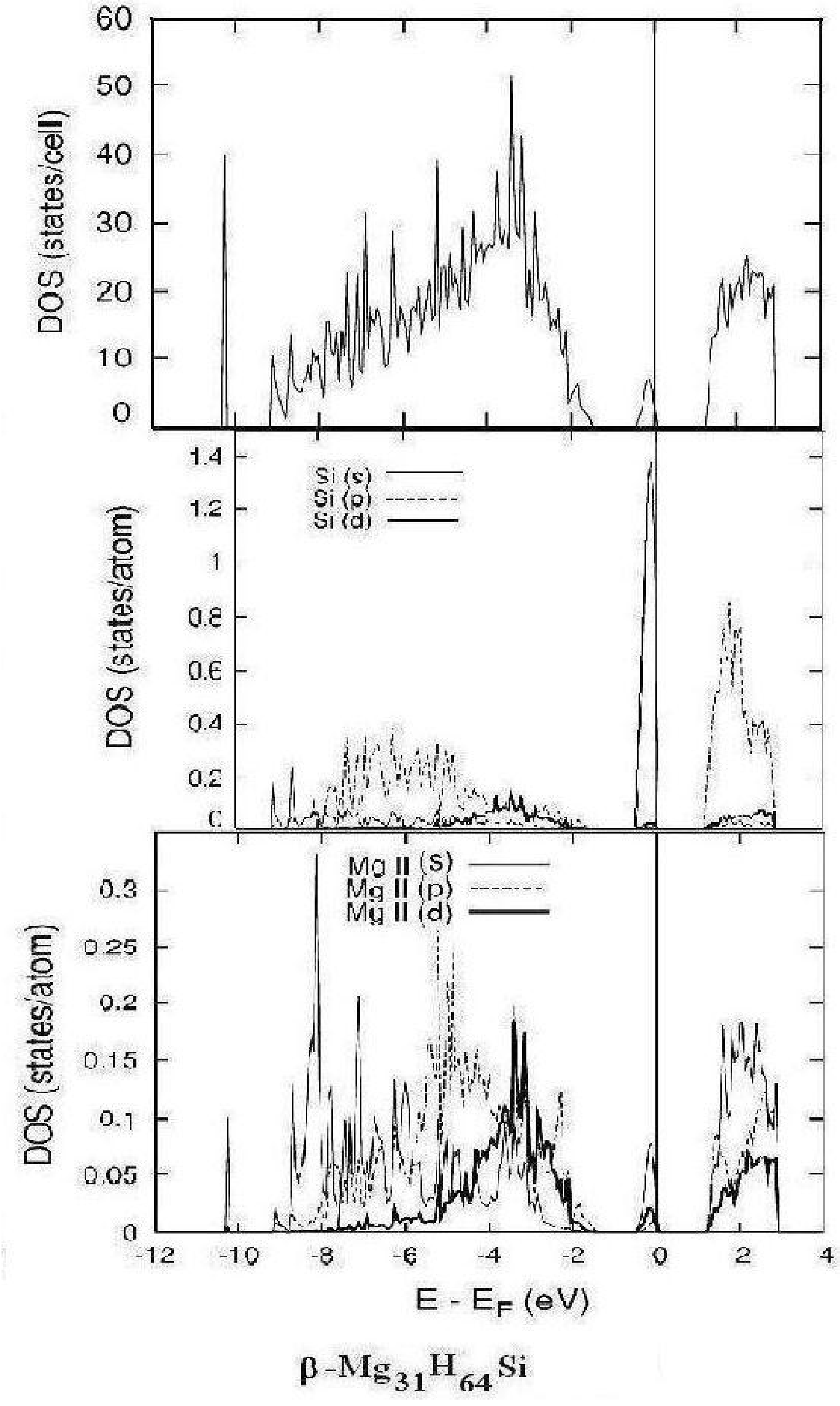

Figure 3.14 Total and partial density of states plots of β-$Mg_{31}H_{64}Si$. The energy is set to zero at E_F.

region from E_F to -0.5 eV arises from both *s* electrons of Al and Mg-I and Mg-VI (Mg-II and Mg-III) atoms.

For the Si-doped MgH_2 phases (α-$Mg_{31}H_{64}Si$, γ-$Mg_{31}H_{64}Si$, and β-$Mg_{31}H_{64}Si$) the total DOS plots are significantly different from those for Al doping. From the total DOS of these systems presented Figs. 3.10, 3.12, and 3.14 it can be clearly seen that while the band gaps are not zero, their values are drastically reduced from 3.9 eV in α-$Mg_{32}H_{64}$ to 0.9 eV in α-$Mg_{31}H_{64}Si$, from 3.8 eV in γ-$Mg_{32}H_{64}$ to 0.5 eV in γ-$Mg_{31}H_{64}Si$, and from 2.5 eV in β-$Mg_{32}H_{64}$ to 1.2 eV in β-$Mg_{31}H_{64}Si$. From the magnitude of these band gaps it is evident that Si-doped α-, γ-, and β-MgH_2 will behave as semiconductors.

The partial DOS plots of the Si-doped MgH_2 phases also shown in Figs. 3.10, 3.12, and 3.14 exhibit that the VB regions extending from -2.8 eV to -8.8 eV in α-$Mg_{31}H_{64}Si$, -2.6 eV to -9.6 eV in γ-$Mg_{31}H_{64}Si$, and -1.5 eV to -9.2 eV in β-$Mg_{31}H_{64}Si$ are formed from s electrons of all H atoms and *s*, *p* and *d* electrons of Si atom and all Mg atoms, while the empty *s*, *p* and *d* states of all Mg atoms and empty *p* states of Si atoms contribute to the CB. A comparison of the total DOS picture of α-$Mg_{31}H_{64}Si$, γ-$Mg_{31}H_{64}Si$, and β-$Mg_{31}H_{64}Si$ (in Figs. 3.8 (b), 3.9 (b), and 3.10 (b)) with that of α-$Mg_{32}H_{64}$, γ-$Mg_{32}H_{64}$, and β-$Mg_{32}H_{64}$ (in Figs. 3.7 (a)-(c)) demonstrates that the decrease in band gaps is an artefact of the generation of additional bands inside the original band gaps of the pure MgH_2 phases. The partial DOS exemplify that these additional states are formed from *s* electrons of Si and (i) *s*, *p* and *d* electrons of Mg-IV atoms in α-$Mg_{31}H_{64}Si$, (ii) *p* electrons of Mg-I atoms in γ-$Mg_{31}H_{64}Si$, and (iii) *s* electrons of Mg-II in β-$Mg_{31}H_{64}Si$.

3.4
Conclusions

A detailed electronic structure analysis of pure and Al- and Si-doped α-, γ-, and β-MgH_2 was carried out. The total charge density surfaces showed that the bonding between Mg and H atoms is ionic and that between Al/Si and the neighbouring H atoms octahedrally arranged around them is covalent. The band structure calculations displayed that a α-MgH_2 is a wide band gap insulator. It was further predicted that substitution of Mg by Al and Si impurities would lead to a significant decrease in the band gaps and cause α-MgH_2 to exhibit metallic conduction and insulating behavior respectively. From DOS plots, Al and Si dopants were envisaged to have a similar effect on the γ and β phases of MgH_2. Examination of the partial DOS illustrated that the above mentioned reduction in band gaps was an artefact of generation of additional bands arising from Al and Si atoms in the original band gap of the pure hydrides. It was also concluded that due to the decrease in band gaps and the consequent destabilization of α-, γ-, and β-MgH_2 caused by Al and Si doping, the Mg-H bond in these will become more susceptible to dissociation as a result of which less energy would be needed to remove H_2 from these hydrides.

References

1. P. Hohenberg and W. Kohn, *Phys. Rev.* **1964**, *136*, 864.
2. P. E. Blöchl, O. Jepsen and O. K. Andersen, *Phys. Rev. B*, 1994, **49**, 16223.
3. J. P. Perdew, J. A. Chevary, S. H. Vosko, K. A. Jackson, M. R. Pederson, D. J. Singh, and C. Fiolhais, *Phys. Rev. B* **1992**, *46*, 6671.
4. G. Kresse and J. Hafner, *Phys. Rev. B* **1993**, *47*, 558.
5. G. Kresse and J. Furthmüller, *Phys. Rev. B* **1996**, *54*, 11169.
6. P. E. Blöchl, *Phys. Rev. B* **1994**, *50*, 17953.
7. G. Kresse and J. Furthmüller, *Comput. Mater. Sci.* **1996**, *6*, 15.
8. J. P. Bastide, B. Bonnetot, J.M. Letoffe, and P. Claudy, *Mater. Res. Bull.* **1980**, *15*, 1215.
9. W. H. Zachariasen, C. E. Holley, Jr., and J. F. Stamper, Jr., *Acta Crystallogr.* **1963**, *A16*, 352.
10. M. Bortz, B. Bertheville, G. Bøttger, and K. Yvon, *J. Alloys Compd.* **1999**, 287, L4.
11. P. Vajeeston, P. Ravindran, B. C. Hauback, H. Fjellvåg, A. Kjekshus, S. Furuseth and M. Hanfland, *Phys. Rev. B* **2006**, *73*, 224102.
12. H. J. Monkhorst and J. D. Pack, *Phys. Rev. B* **1976**, *13*, 5188.

13. http://vaspview.sourceforge.net/
14. A. Kokalj, *Comput. Mater. Sci.* **2003**, *28*, 155.
15. M. I. Aroyo, C. Kirov, C. Capillas, J. M. Perez-Mato, and H. Wondratschek, *Acta Crystallogr. Sect. A* **2006**, *62*, 115.
16. M. I. Aroyo, J. M. Perez-Mato, C. Capillas, E. Kroumova, S. Ivantchev, A. Madariaga, A. Kirov, and H. Wondratschek, *Z. Kristallogr.* **2006**, *221*, 15.
17. P. Vajeeston, P. Ravindran, A. Kjekshus, H. Fjellvåg, *Phys. Rev. B* **2004**, *69*, 020104.
18. A. Peles, J. A. Alford, Z. Ma, L. Yang, and M. Y. Chou, *Phys. Rev. B* **2004**, *70*, 165105.
19. P. Vajeeston, P. Ravindran, A. Kjekshus, and H. Fjellvåg, *Phys. Rev. Lett.* **2002**, *89*, 175506.
20. U. Häussermann, H. Blomqvist, and D. Noréus, *Inorg. Chem.* **2002**, *41*, 3684.
21. J. Isidorsson, I. A. M. E. Giebels, H. Arwin, and R. Griessen, *Phys. Rev. B* **2003**, *68*, 115112.
22. G. Krasko, *Metal-Hydrogen Systems*, Pergamon, NewYork, **1982**.

CHAPTER 4

Thermodynamics and kinetics Of hydrogen desorption

There is really no insurmountable
***barrier** save your own*
inherent weakness of purpose.
-Ralph Waldo Emerson

Some of the fundamental questions that need to be asked for any potential solid-state hydrogen storage material are: What is the energy requirement for removal of hydrogen? What are the activation barriers for hydrogen desorption? How do additives help in reducing the operating temperature and pressure for hydrogen uptake and release? What is the importance of the high pressure metastable phases which occur as by-products during synthesis of materials?

A comprehensive understanding of the abovementioned properties is imperative for designing new hydrogen storage materials as well for finding ways to significantly improve current technologies. In this chapter a summary of our studies on the complex metal hydrides α- and β-$LiAlH_4$ and $LiBH_4$ with reference to Paper I and on Al- and Si-doped magnesium hydride in its different phases in Papers II and IV, is presented. In the first section we provide the relating general background information. The computational methodology that was employed is briefly described in Section 4.2. The results and discussion are divided into two parts with Section 4.3.1 pertaining to the dehydrogenation reaction energies and Section 4.3.2 focusing on the activation energy barriers. Finally the conclusions are presented in the last section.

4.1
Introduction

Magnesium-based hydrides and alkali metal complex hydrides have continued to generate great interest as hydrogen (H_2) storage compounds due to their high gravimetric storage capacities. Magnesium hydride (MgH_2) can store up to 7.6 wt.% H_2. The maximum available weight percentage offered by lithium aluminium hydride ($LiAlH_4$) is 10.6 wt.% H_2 and by lithium borohydride ($LiBH_4$) is 18.0 wt.% H_2. However, practical use of these three hydrides in fuel cell transportation applications is limited because of their thermodynamic and kinetic deficiencies. MgH_2 has a high thermodynamic stability and it releases H_2 at a high temperature of ~300°C. [1] Furthermore, it has a slow H_2 sorption kinetics which limits its application for on-board H_2 storage. [2] Upon rapid heating $LiAlH_4$ first endothermically melts from 165-175°C, before decomposing and exothermically crystallizing to form lithium aluminium hexahydride (Li_3AlH_6) over the range of 175-220°C. [3] The second decomposition step occurs during an endothermic melt reaction over the range of 220-270°C to form LiH. Decomposition of $LiBH_4$ which takes place according to:

$$LiBH_4 \rightarrow LiH + B + 3/2\ H_2 \qquad (4.1.1)$$

has a standard reaction enthalpy of ~67.0 kJ/mol H_2, resulting in a thermodynamic desorption temperature of 410°C at 1 bar. [4]

Several first-principles calculations have focused on studying the crystal structure, electronic structure, and thermodynamic stability of various alanates [5-8] and borohydrides [9, 10]. Vajeeston et al. [11] have systematically investigated using an *ab initio* projected augmented plane-wave method entire series of alkali aluminum and alkali gallium tetrahydrides of the form ABH_4 where A= Li, Na, K, Rb, or Cs and B=Al or Ga. From the structural stability studies they were able to successfully reproduce the equilibrium structures for the known phases $LiAlH_4$, $NaAlH_4$, $KAlH_4$, and $NaGaH_4$ as well as of the unknown members of this series. However, these materials typically have heats of formation that are too high to be used for hydrogen storage in fuel cells.

Reilly and Wiswall [12, 13] through their pioneering work showed that the hydrogenation/dehydrogenation thermodynamics of metal hydrides can be modified by using additives that form alloys or compounds with the metal in the dehydrogenated state that are energetically favorable to the products of the reaction without additives. For example, MgH_2 to $LiBH_4$ led to reversible hydrogenation and dehydrogenation of $LiBH_4$ with a considerable decrease in heat of formation. [13] The MgB_2 formed during the reaction stabilized the dehydrogenated state and thereby destabilized $LiBH_4$. Destabilization of $LiBH_4$ with a series of metals M = Mg, Al, Ti, V, Cr, or Sc or metal hydrides MH_2 = MgH_2, TiH_2, or CaH_2 have been experimentally investigated. [14] Of these the thermodynamically predicted products for reaction of $LiBH_4$ with Mg, Al, MgH_2, and CaH_2 were observed experimentally while the reactions with Ti, Sc, V, Cr, and TiH_2 were kinetically prohibited. Destabilization of the $LiBH_4$ using $LiNH_2$ lead to a release of 11.9 wt.% H_2 on completion. [15, 16] It was further reported that this reaction lead to the formation of an intermediate hydride, $Li_3BN_2H_8$ (later corrected to $Li_4BN_3H_{10}$) [17] whose dehydrogenation is exothermic at room temperature.

Aluminum has been found to destabilize MgH_2 by forming a Mg/Al alloy upon dehydrogenation. [18] The reaction is reversible with MgH_2 and Al reforming and segregating during hydrogenation. Silicon when used for alloying LiH and MgH_2 destabilizes these strongly bound hydrides by forming relatively strongly bound compounds with Li and Mg which reduce dehydrogenation enthalpies and increase equilibrium hydrogen pressures. [19] The Calculation of phase diagrams (CALPHAD) method involves assessment of the thermodynamic properties of all the phases in a system for reliably predicting the phase diagrams in regions for which no experimental information is available. By applying the abovementioned thermodynamic CALPHAD approach to numerous combinations of metal hydrides such as LiH, MgH_2, $LiBH_4$, and $NaBH_4$ with light elements Al and Si, Cho et al. [20] predicted that the pairs of MgH_2+Si and $LiBH_4$+Al would undergo a significant decrease in decomposition temperature.

Alapati et al. [21] have used density functional theory (DFT) [22] to calculate the reaction enthalpies of a series of potential destabilized metal hydride schemes. On the basis of these calculations the authors identified five new destabilized reactions with high gravimetric and volumetric H_2 storage densities and with reaction enthalpies close to the range necessary for reversibility at mild conditions. These reaction schemes were: $3LiNH_2 + 2LiH + Si \rightarrow Li_5N_3Si + 4H_2$, $4LiBH_4 + MgH_2 \rightarrow 4LiH + MgB_4 + 7H_2$, $7LiBH_4 + MgH_2 \rightarrow 7LiH + MgB_7 + 11.5H_2$, $CaH_2 + 6LiBH_4 \rightarrow CaB_6 + 6LiH + 10H_2$, and $LiNH_2 + MgH_2 \rightarrow LiMgN + 2H_2$. Using the same computational methodology, Alapati and co-workers [23] have also carried out thermodynamic calculations with first-principles DFT for the destabilized metal hydride reactions of the form:

$$X_{1-x}Y_xH_2 + 2\ LiBH_4 \rightarrow X_{1-x}Y_xB_2 + 2\ LiH + 4\ H_2 \qquad (4.1.2)$$

where X, Y = Mg, Sc, or Ti.

Doping metal hydrides with fractions of transition metals may be another route for tuning the thermodynamics of their dehydrogenation reactions. Following Bogdanovic and Schwickardi's [24] discovery of $NaAlH_4$ exhibiting reversible dehydrogenation with significantly improved H_2 desorption kinetics in the presence of titanium catalysts, several theoretical studies on Ti-catalyzed sodium alanates have been performed. [25-28] Various experimental and DFT calculations based studies have shown that transition metals have a similar effect on both the thermodynamics and kinetics of H_2 removal from MgH_2. [29-32]. It has been reported that catalytic effect of different intermetallics [33], metal oxides and chlorides [34-37], and transition metal oxides [38-40] can also enhance the H_2 sorption kinetics of MgH_2.

Recently, a computational study by Liang [41] showed that substitution of two Mg atoms of MgH_2 by a Li and an Al atom may improve its hydrogen storage processes by lowering both its reaction energies and the H_2 desorption activation barriers.

It has been known for some time that when subjected to high-pressure and high-temperature conditions the low-pressure tetragonal form α-MgH_2 transforms into a high-pressure orthorhomic modification γ-MgH_2. [42] γ-MgH_2 has also been known to occur as a by-product during high-pressure synthesis of magnesium based ternary metal hydrides. [43] [36] In 1999 Bortz et al. determined accurate structures of α- and γ-MgH_2 from X-ray and powder neutron diffraction. [44] Owing to the difficulties associated with establishing hydrogen position in a metal matrix by X-ray diffraction, limited high-pressure information on MgH_2 was available at first. To remedy this situation Vajeeston et al. [45] examined MgH_2 theoretically at high pressure in 11 closely related structural configurations by density functional calculations. It was predicted that on application of pressure the ground state α-MgH_2 became unstable to undergo transformations into four modifications γ, β, δ, and ε. These theoretical findings motivated a high-pressure synchrotron X-ray diffraction study of phase transitions associated with MgH_2 recently. [46] Owing to the close structural similarity between α and γ modifications, the high-pressure γ form was found to be stabilized as a metastable phase after pressure release. However, instead of the theoretical δ phase a δ' modification was established while the ε phase could not be identified at all.

Song and Guo have reported a first-principles prediction of a metastable phase of MgH_2 that is characterized by tetragonal symmetry $I4_1/amd$ (group 141) with the lattice parameters a = 0.3813 nm and c = 0.9416 nm. [47] This phase was able to meet all the mechanical stability criteria and has a heat of formation (−58.03 kJ/mol H_2) which is much less negative than that of the ground state α-MgH_2 phase (−76 kJ/mol H_2). The authors thus suggest that this tetragonal structure would be more desirable than the α phase for practical hydrogen storage applications. Similarly DFT calculations have predicted that certain high pressure phases of AlH_3 [48] and SiH_4 [49] could result in more favourable hydrogen desorption kinetics of these materials leading to a possibility of feasible hydrogen storage.

The H_2 desorption properties of commercial nanocrystalline MgH_2 processed by controlled mechanical milling was investigated by Varin et al. [50] wherein through quantitative evidence it was concluded that coexistence of the metastable γ-MgH_2 with the stable nanocrystalline β-MgH_2 within the powder particles was one of the factors responsible for the substantial reduction of the H_2 desorption temperature of MgH_2.

For theoretical modeling of $LiAlH_4$ seven closely related potential structure types were considered by Vajeeston et al. [51]: α-$LiAlH_4$ (~monoclinic; $P2_1/c$), α-$NaAlH_4$ (~tetragonal; $I4_1/a$), β-$LiBH_4$ (~hexagonal; $P63mc$), $NaGaH_4$ (~orthorhombic; *Cmcm*), $NaBH_4$ (~cubic, $Fm3m$), $SrMgH_4$ (~orthorhombic; $Cmc21$), and $KGaH_4$ (~orthorhombic; *Pnma*). On application of high pressure two phase transformations were identified one at 2.6 GPa from α-$LiAlH_4$ the prototype structure to β-$LiAlH_4$ (α-$NaAlH_4$ type) and subsequently at 33.8 GPa from β- to γ-$LiAlH_4$ ($KGaH_4$ type). The former was associated with a huge volume collapse of 17%. This observation along with the low energy difference between α- and β-$LiAlH_4$, low transition pressure, and the high weight content of hydrogen of the β phase suggest β-$LiAlH_4$ as a promising candidate for hydrogen storage.

In the light of the importance of high pressure phases in Paper I we study the thermodynamics of α- and β-$LiAlH_4$ and $LiBH_4$. We exemplify the destabilization of MgH_2 caused by light metals in Paper II by investigating the effect of Al and Si doping on the dehydrogenation reaction of α-MgH_2. In Paper IV we examine the influence of Al and Si doping on the thermodynamics as well as kinetics of H_2 desorption associated with α-, γ-, and β-MgH_2.

4.2
Computational details

All the calculations presented herein were performed using DFT [22] within GGA [52] as implemented in VASP [53, 54]. In Paper I already available experimentally established structural data of $LiAlH_4$ and $LiBH_4$ was used as input for the calculations, all of which are carried out at the gamma point. The interactions between ions and electrons were described by using Vanderbilt's USPPs [55] provided with VASP as they allow for a considerable reduction in the number of plane waves per atom. Atoms were relaxed to equilibrium until the forces became less than 0.005 eV/Å during all relaxations. At least 0.01 meV/atom was placed as a criterion on the self-consistent convergence of the total energy.

In Papers II and IV we employed a plane wave basis set cut-off of 440 eV and used PAW pseudopotentials [56, 57]. To simulate the Al- and Si-doped magnesium hydrides we have considered 4 x 2 x 2, 2 x 2 x 2, 3 x 1 x 1 and 5 x 1 x 1 supercells of α-MgH_2 and 2 x 2 x 2 supercells of γ- and β-MgH_2. These pure hydride supercells will be referred to as α-$Mg_{32}H_{64}$, α-$Mg_{16}H_{32}$, α-Mg_6H_{12}, α-$Mg_{10}H_{20}$, γ-$Mg_{32}H_{64}$, and β-$Mg_{32}H_{64}$, respectively. Fractions x = 0.03125, 0.0625, 0.1 and 0.167 of Al and Si are introduced in α-MgH_2 by replacing one Mg atom out of a total 32, 16, 10 and 6 Mg atoms in its 4 x 2 x 2, 2 x 2 x 2, 5 x 1 x 1 and 3 x 1 x 1 supercells respectively, by one Al or Si atom. These substituted α-MgH_2 supercells are represented as α-$Mg_{31}H_{64}X$, α-$Mg_{15}H_{32}X$, α-$Mg_9H_{20}X$, and α-$Mg_5H_{12}X$, respectively. The fraction x = 0.03125 of Al and Si doping was generated in γ- and β-MgH_2 by replacing one Mg atom out of the total 32 Mg atoms in their 2 x 2 x 2 supercells with one Al or Si atom and these doped phases will be referred to as γ-$Mg_{31}H_{64}X$ and β-$Mg_{31}H_{64}X$, respectively.

The resulting geometries were then optimized by force and stress minimization. Relaxation was performed until the forces on each atom became less than 0.5 meV/Å. A criterion of 0.1 meV was placed on the self-consistent convergence of the total energy. The reciprocal space sampling for the 4 x 2 x 2, 2 x 2 x 2, 5 x 1 x 1 and 3 x 1 x 1 2 x 2 x 2 supercells of α-MgH_2 was done with a 4 x 4 x 4, 6 x 6 x 6, 12 x 4 x 4, and 12 x 4 x 4 Monkhorst-Pack [58] **k**-point grid respectively and for the 2 x 2 x 2 supercells of γ- and β-MgH_2 a 4 x 4 x 4 **k**-point mesh was applied.

In Paper IV, 2 x 2 x 2 slabs with a vacuum space of at least 10 Å, kept to maintain a sufficient separation between periodic images, were used for describing the (001) surfaces of the pure and the Al- and Si-doped α-, γ-, and β-MgH_2. Within the slabs the adsorbed H atoms and atoms in the top three layers were allowed to relax while atomic positions of the atoms in the bottom layers were kept fixed. As large supercells containing 96 atoms are employed, calculations involving the slabs were carried out only at the gamma point. For gaining a preliminary understanding about the effect of Al and Si impurities on the dehydrogenation kinetics of MgH_2 we chose to look at the one-step direct dehydriding path associated with the (001) surfaces. In this one-step direct dehydriding path two H atoms bound to different Mg atoms were simultaneously desorbed from the surface to form molecular hydrogen. To model this path (i) the initial states (IS) were chosen as the relaxed equilibrium configurations of these pure and doped surfaces with the dopant Al and Si atoms residing in the bulk as in case of ΔH_f calculations, (ii) the final states (FS) were prepared by removing a pair of H atoms from the surfaces and reintroducing them as H_2 molecules at a distance of 5.0 Å or more from the topmost layer. These preliminary FS were then relaxed, and (iii) a chain of images lying in between the IS and FS geometries was built and ionic relaxation was performed for each of the images. In each of the relaxations the z-coordinates of the two H atoms were kept fixed. The total energies of these successive configurations were calculated and plotted as a function of the perpendicular distance of the two desorbed H atoms from the top layer to determine the activation energy barriers (E_{act}). The E_{act} thereby calculated can thus be considered as upper limits as the two desorbing H atoms are not allowed to reorient themselves.

4.3
Results and discussion

4.3.1
Dehydrogenation reaction energies

α- and β-$LiAlH_4$ and $LiBH_4$: The enthalpies of formation (ΔH_f) of $LiAlH_4$ and $LiBH_4$ in both α and β phases were evaluated with respect to their standard state elemental constituents as defined by the reaction:

$$Li\,(s) + M\,(s) + 2\,H_2\,(g) \rightarrow LiMH_4\,(s) \tag{4.3.1}$$

The enthalpies of reaction (ΔH_{reac}) have been calculated for the following overall dehydrogenation reaction:

$$LiMH_4\ (s) \rightarrow LiH\ (s) + M\ (s) + 3/2\ H_2\ (g) \tag{4.3.2}$$

In Equations (4.3.1) and (4.3.2) M = Al or B. The predicted ΔH_f and ΔH_{reac} for α- and β-$LiAlH_4$ and $LiBH_4$ are listed in Table 4.1. Our calculated ΔH_f values of -102.02 $kJmol^{-1}$ and -146.99 $kJmol^{-1}$ for α-$LiAlH_4$ and $LiBH_4$ respectively agree well with the previously reported values of -107 $kJmol^{-1}$ determined experimentally at 298 K for $LiAlH_4$ by Dymova et al. [59] and of -160 $kJmol^{-1}$ for $LiBH_4$ obtained using first-principles calculations by Miwa and co-workers [60].

It is noticeable from the Table 4.1 that all the ΔH_f are negative implying that the complex metal hydrides under investigation are thermodynamically stable with respect to the complete decomposition into the constituent elements. This stability is greatly reduced when $LiAlH_4$ and $LiBH_4$ undergo a transition from their ground state

Table 4.1 Enthalpies of formation and enthalpies of reaction of $LiAlH_4$ and $LiBH_4$ in α- and β-phases in kJ mol^{-1}. The energies of the reactants are referenced to their constituent atoms.

Reaction and energies of reactants and products (kJ mol^{-1})	***ΔH (kJ mol^{-1})***
Li (s) + Al (s) + 2 H_2 (g) → $LiAlH_4$ (s) -146.51 -284.27 -876.04 -1408.84 (α), -1361.23(β)	-102.02 (α), -54.41 (β)
$LiAlH_4$ (s) → LiH (s) + Al (s) + 3/2 H_2 (g) -1408.84 (α), -1361.23 (β) -388.62 -284.27 -657.03	78.92(α), 31.31 (β)
Li (s) + B (s) + 2 H_2 (g) → $LiBH_4$ (s) -146.51 -662.96 -876.04 -1832.50 (α), -1741.59 (β)	-146.99 (α), -56.08 (β)
$LiBH_4$ (s) → LiH (s) + B (s) + 3/2 H_2 (g) -1832.50 (α), -1741.59 (β) -388.62 -662.96 -657.03	123.89(α), 32.98 (β)

α to β phase as reflected by the much increased ΔH_f of the β modifications. Furthermore, amongst the two hydrides $LiBH_4$ is thermodynamically more stable than $LiAlH_4$. In comparison, the ΔH_{reac} are positive illustrating that releasing H_2 from these hydrides is an endothermic process. The table shows ΔH_{reac} follows the same trends as ΔH_f: (i) β phase < α phase, (ii) α-$LiAlH_4$ < α-$LiBH_4$ and (iii) β-$LiAlH_4$ ≈ β-$LiBH_4$. As the equilibrium volume of $LiBH_4$ is much less than that of $LiAlH_4$, it will have a much higher volumetric hydrogen storage capacity. This coupled with the fact that dehydrogenation from its β form requires much less energy and will therefore have a greatly reduced dehydrogenation temperature, suggests that from the four complex metal hydrides studied β-$LiBH_4$ is the most potential hydrogen storage material.

α-MgH_2: From the electronic structure analysis in Chapter 3 it is evident that inclusion of Al and Si would affect the Mg-H bond dissociation of the ground state MgH_2. To this end in Paper II our first approach was to study a possible scenario of H_2 dissociation in which Al and Si are not ejected out but retained with Mg as an alloy of the form $Mg_{1-x}X_x$ (X = Al or Si). For this purpose we randomly removed different numbers of H_2 molecules at a time from the pure and Al- and Si-substituted α-MgH_2 supercells. The resulting structures were geometry optimized and used to calculate energies for following reactions:

$$Mg_iH_{2i} \rightarrow Mg_iH_{2i-2n} + n\,H_2 \qquad (4.3.3)$$

$$Mg_{i-1}XH_{2i} \rightarrow Mg_{i-1}XH_{2i-2n} + n\,H_2 \qquad (4.3.4)$$

where i = 6, 10 and 16 for 3 x 1 x 1, 5 x 1 x 1 and 2 x 2 x 2 supercells and n = 1, 2, 3, and 2i. These reactions while very simplistic in nature provide a means for developing a fundamental understanding regarding a possible route for H_2 dissociation which may be more preferable as compared to complete dissociation of MgH_2 because here energy would not be needed to substitute Mg by Al or Si during the reverse hydriding reaction.

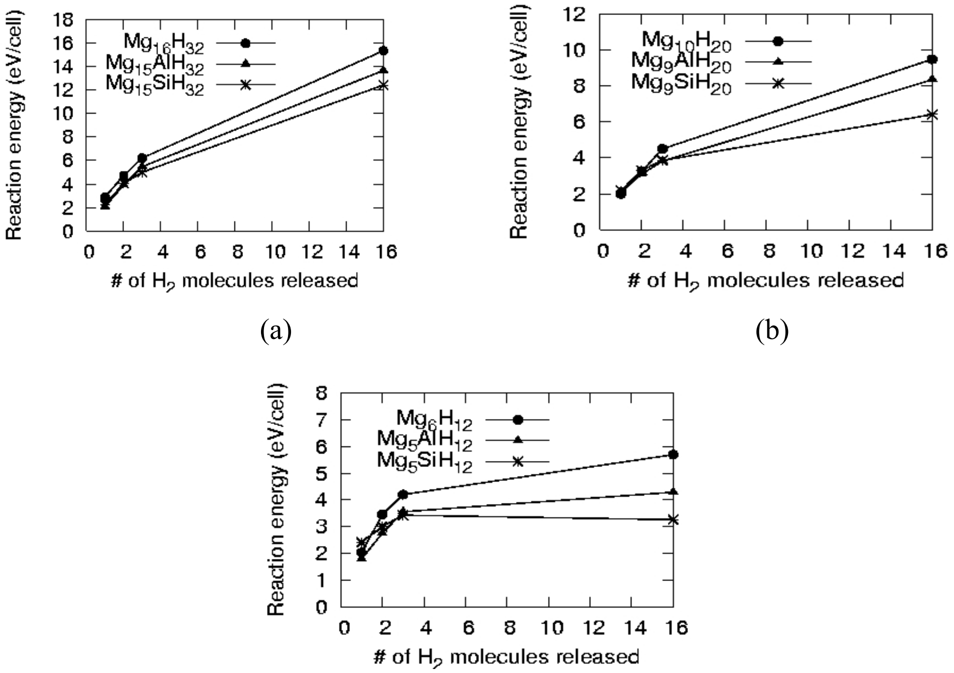

(a) (b)

(c)

Figure 4.1 Reaction energies for stepwise removal of H_2 molecules from the pure and substituted (a) 2 x 2 x 2, (b) 5 x 1 x 1 and (c) 3 x 1 x 1 α-MgH_2 supercells.

The reaction energies thus obtained were then plotted as a function of number of H_2 molecules released and are displayed in Figs. 4.1(a)-(c). The following ensuing trends are noticeable for the three supercells considered: (a) reaction energy increases with increase in number of H_2 molecules released, and (b) reaction energy of pure MgH_2 > Al-substituted MgH_2 > Si-substituted MgH_2. Thus as Mg is swapped by Al and Si there is a reduction in the energy required for bringing out dehydrogenation of MgH_2.

The second set of dehydriding reactions that were also considered are given below:

$$(1-x)\,Mg + H_2 + x\,X \rightarrow Mg_{1-x}\,X_xH_2 \qquad (4.3.5)$$

Table 4.2 Calculated heats of formation ΔH_f for $Mg_{1-x}X_xH_2$. where X = Al or Si and x = 0.0, 0.0625, 0.1, 0.167, and 0.2.

Fraction	**ΔH_f (kJ/mol H_2)**		
	Al	**Si (FCC)**	**Si (Diamond)**
0.0	-69.61 (-0.721 eV/f.u.)		
0.0625	-58.93	-52.94	-49.32
0.1	-59.89	-44.16	-38.36
0.167	-45.13	-27.14	-17.47

where X = Al or Si and the fraction x = 0.0625, 0.1, and 0.167. The heats of formation ΔH_f for these reactions were computed by using the formula:

$$\Delta H_f(Mg_{1-x}X_xH_2) = E_{tot}(Mg_{1-x}X_xH_2) - (1-x)\,E_{tot}(Mg) - x\,E_{tot}(X) - E_{tot}(H_2) \qquad (4.3.6)$$

We have calculated the energies for Si in both FCC and diamond phase.

The calculated ΔH_f values are listed in Table 4.2. In the absence of impurity ΔH_f is -0.721 eV/H_2 which lies within the range of -0.67 and -0.76 eV/H_2 defined by the values calculated computationally by Setten et al. [61] and by extrapolating the experimental results to 0 K [62, 63]. It is known that compounds with H_2 binding energies $\geq$ -20 kJ/mol H_2 are unable able to survive ambient conditions while those with energies $\leq$ -50 kJ/mol H_2 require high temperatures or pressures to produce H_2. Thus if the ΔH_f of MgH_2 could be brought in the -20 to -50 kJ/mol H_2 range it would make it a better hydrogen storage material.

It can be seen from Table 4.2 that as fraction x of Al and Si increases ΔH_f decreases and for each x Si causes a greater reduction than Al. Recalling -20 to -50 kJ/mol H_2 as the energy region of interest, the fractions of impurity that will prove beneficial are: Al for x = 0.167, Si (FCC) x = 0.1, 0.167 and Si (diamond) x = 0.0625, 0.1. The ΔH_f for these particular cases are even lower than ΔH_f (-51.614 kJ/mol H_2)

calculated by Song et al. [31] for MgH_2 substituted by a fraction 0.2 of Ti. Thus, in comparison to Ti from a point of view of the energy requirement as well as the amount of impurity to be added, both Al and Si are better agents for improving the dehydrogenation characteristics of MgH_2. Hence substitution of Mg by Al or Si can be used in place of Ti as a route for reducing the dehydrogenation reaction energy and consequently lowering the dehydrogenation temperature of MgH_2 for enhancing its hydrogen storage properties.

α-, γ- and β-MgH_2: In Paper IV in order to avoid the Pulay stress problem arising from the fact that the plane wave basis set in not complete with respect to the changes in volume, we performed cell shape and ionic relaxations of the pure and Al- and Si-doped α-, γ-, and β-MgH_2 at fixed volumes and at a constant energy cut-off of 440 eV rather than at constant pressures. The final energies of the pure and doped phases were then fit to the Murnaghan equation of state (EOS) [64],

$$F(V) = F(V_0) + \frac{K_0 V}{K_0'(K_0' - 1)}\left[K_0' - 1 + \left(\frac{V_0}{V}\right)^{K_0'}\right] - \frac{K_0 V_0}{K_0' - 1} \qquad (4.3.7)$$

to yield the following bulk material quantities: equilibrium cell volume V_0, isothermal bulk modulus K_0 and its pressure derivative K_0', and the ground state total energy $E_0(V_0)$. Table 4.3 lists for all the three pure MgH_2 phases and for α-$Mg_{15}H_{32}X$, γ-$Mg_{31}H_{64}X$ and β-$Mg_{31}H_{64}X$ where X = Al or Si their corresponding V_0, K_0, K_0’, and $E_{rel}(V_0)$ which is $E_0(V_0)$ relative to those of the undoped α-MgH_2.

Most solids are known to be elastic solids while the volume only Murnaghan EOS is isotropic. The appropriateness of its application as an approximation is exemplified from the excellent agreement of the EOS parameters derived herein for the rutile α-MgH_2, the orthorhombic γ-MgH_2, and the fluorite β-MgH_2 with previously reported theoretical [45] and experimental [46] results. A comparison of the V_0 values suggests that formation of the β phase would lead to a volume reduction of 9.1% relative to the most stable α phase. This volumetric advantage however may be diminished due to a simultaneous increase in K_0 of 8.3% of β-MgH_2 which would deteriorate its compressibility. Doping the above mentioned α, γ, and β phases by fractions of

Table 4.3 Calculated EOS parameters, namely, ground state cell volume V_0, bulk modulus K_0 and its pressure derivative K_0', and total energy of the system at V_0 relative to pure α-MgH_2 $E_{rel}(V_0)$ of pure and Al- and Si-doped α-, γ-, and β-MgH_2. Previously reported theoretical [45] and experimental [46] values are presented in (..) and in [..] respectively.

System	*Fraction x*	*V_0 (Å^3/f.u.)*	*K_0 (GPa)*	*K_0'*	*$E_{rel}(V_0)$ (eV/f.u.)*
α-MgH_2	0.0	30.419 (30.17) [30.82]	51.963 (51) [45±2]	3.591 (3.45) [3.35±.3]	0.0
γ-MgH_2	0.0	29.895 (29.69) [30.35]	47.833 (48) [44.03±2]	3.224 (3.07) [3.17±.4]	0.004
β-MgH_2	0.0	27.659 (27.48) [25.39]	56.260 (56) [47.41±4]	3.489 (3.52) [3.49±.4]	0.096
α-MgH_2Al	0.0625	30.348	51.112	3.613	-0.024
γ-MgH_2Al	0.03125	29.826	46.991	3.177	-0.006
β-MgH_2Al	0.03125	27.651	55.619	3.567	0.083
α-MgH_2Si	0.0625	30.652	51.299	3.485	-0.033
γ-MgH_2Si	0.03125	30.050	45.510	3.473	-0.013
β-MgH_2Si	0.03125	27.722	55.969	3.476	0.074

Al and Si decreases their bulk moduli. Between the two impurities Al causes a relatively greater decrease in K_0 and also reduces the V_0. On the other hand replacement of one Mg atom in the supercell by a Si atom increased the cell volumes.

The ground state total energies $E_0(V_0)$ of all the hydrides under investigation, presented in Table 4.3, obtained after EOS fitting were then used for calculating the heats of formation ΔH_f using Equation (4.3.6) of the dehydrogenation reactions for the pure and Al- and Si-doped α-, γ-, and β-MgH_2 as depicted by Equation (4.3.5). The evaluated values for α-MgH_2 for the fractions x = 0, 0.03125, 0.0625 and for γ- and β-MgH_2 for the fractions x = 0, 0.03125 dopants are recorded in Table 4.4. It is noticeable from Table 4.4 that ΔH_f of α- and γ-MgH_2 differ only by 0.441 $kJmol^{-1}$ H_2 or 0.004 eVH_2^{-1}. This is understandable considering their total energies are nearly the same at equilibrium cell volume. The order of the calculated ΔH_f for the three phases in pure form is: β-MgH_2 << γ-MgH_2 ~ α-MgH_2. This is in accordance to our prediction made in the Chapter 3 on the basis of the sizes of band gaps, of β-MgH_2 requiring the least energy for H_2 removal. As β-MgH_2 has the smallest ΔH_f we therefore expect it to also have the lowest dehydrogenation temperature.

On substitution of Mg by fractions x = 0.03125 Al or Si, ΔH_f of α, γ, and β phases of MgH_2 decreases considerably. We evaluated the percentage decrease in heats of formation $\Delta^{\downarrow}H_f(\%)$ using the formula:

$$\Delta^{\downarrow}H_f(\%) = \frac{\Delta H_f(Mg_{1-x}X_xH_2) - \Delta H_f(MgH_2)}{\Delta H_f(MgH_2)} x100\% \qquad (4.3.6)$$

According to the above relation $\Delta^{\downarrow}H_f(\%)$ of a particular doped phase of MgH_2 is evaluated with respect to ΔH_f of its corresponding pure phase. The values thus obtained are also presented in Table 4.4. Within the Al-doped MgH_2 and Si-doped MgH_2 series at fraction x = 0.03125 of substitution, $\Delta^{\downarrow}H_f(\%)$ is maximum for the β phase. Furthermore, for each phase and at the same doping fraction x = 0.03125, $\Delta^{\downarrow}H_f(\%)$ of the Si-substituted hydrides is nearly double the $\Delta^{\downarrow}H_f(\%)$ of the Al-substituted MgH_2 modification. It can be inferred that while doping with Al and Si

Table 4.4 Calculated heats of formation ΔH_f and percentage decrease in heats of formation $\Delta^{\downarrow}H_f(\%)$ of pure and Al- and Si-doped α-, γ-, and β-MgH_2.

System	*Fraction* *x*	*ΔH_f (kJ/mol H_2)*		*$\Delta^{\downarrow}H_f(\%)$*	
		Al	***Si***	***Al***	***Si***
α-MgH_2	0.0	69.636	69.636	0.0	0.0
	0.03125	64.290	59.456	7.7	14.6
	0.0625	58.926	49.316	15.4	29.2
γ-MgH_2	0.0	69.195	69.195	0.0	0.0
	0.03125	63.578	59.069	8.1	14.6
β-MgH_2	0.0	60.321	60.321	0.0	0.0
	0.03125	55.058	50.678	8.7	16.0

influences the dehydrogenation reaction energies of all the hydrides, it is ΔH_f of β-MgH_2 that is reduced the most and it is Si which is more effective at this task.

In contrast to our results which predict that it is the pure and Al- or Si-doped β-MgH_2 which would get decomposed most easily, Varin et al. [50] had found that appearance of the γ phase with β-MgH_2 resulted in a drastic decrease of its H_2 desorption temperature. These differences in trends could probably be a manifestation of the fact that while in our theoretical calculations effect of particle size has not been investigated, in the experimental work mentioned above hydrogen desorption properties of nanostructured MgH_2 powders with a wide range of hydride particle sizes were studied. The authors concluded that the decrease in H_2 desorption temperature was actually a result of phase duality as well as a decrease in mean hydride particle size (ECD). The decrease in ECD was explained in terms of an increase in the finer particle content which occurred in powders containing both β- and γ-MgH_2 phases as opposed to those with only β-MgH_2.

4.3.2
Activation energy barriers

In this section we discuss the effect of Al and Si doping on the kinetics of H_2 desorption from α-, γ-, and β-MgH_2 (001) surfaces as reported in Paper IV. For determining the activation energy barriers E_{act}, we considered a one-step direct dehydriding path in which two H atoms bound to different Mg atoms on the surface simultaneously desorb to form molecular hydrogen. The total energy is calculated as a function of the reaction coordinate which is the distance of the two desorbing H atoms from the surface. The corresponding E_{act} obtained in this manner are listed in Table 4.5.

For the pure α-MgH_2 (001) surface we derived an E_{act} of 2.86 $eVmol^{-1}$ H_2 or 273.2 $kJmol^{-1}$ H_2 (i.e. 1.431 $eVmol^{-1}$ H or 138.1 $kJmol^{-1}$ H). This shows excellent agreement with the desorption barrier of 2.86 eV calculated for the MgH_2 (001) surface in an earlier *ab intio* DFT study. [65] Using thermal desorption spectroscopy and differential calorimetry Fernańdez and Sańchez [66] obtained the activation energy for H (atom)-desorption process of MgH_2 as 166±4 kJ/mol H. For MgH_2 prepared by ball milling the reported activation energy is 323±40 $kJmol^{-1}$ H_2. [67] A possible reason for the disagreement between the experimental and theoretical results is that in case of the former several processes such as diffusion and nucleation may be

Table 4.5 The activation energy barriers E_{act} for H_2 desorption from pure and Al- and Si-doped α-, γ-, and β-MgH_2 (001) surfaces.

System	***E_{act} ($eVmol^{-1}$ H_2)***		
	α-MgH_2	***γ- MgH_2***	***β-MgH_2***
Pure	2.86	2.43	0.15
Al-doped	1.99	2.77	0.94
Si-doped	2.90	2.05	1.92

occurring along with H_2 desorption. Furthermore the experimental values are averaged over the different surfaces and crystal orientations. In comparison our density functional based calculations are centered on the MgH_2 (001) surface only. In addition we have examined only those cases in which the Al and Si impurities are present in the bulk. Hence, while it may not adequate to use the our results for quantitative conclusions, nevertheless they can help in arriving at qualitative generalizations about the effect of Al and Si doping on the kinetics of H_2 desorption from MgH_2 for improving its hydrogen storage characteristics.

From Table 4.5 the following orders of E_{act} are perceptible: (i) Al-doped α-MgH_2 < pure α-MgH_2 < Si-doped α-MgH_2 (ii) Si-doped γ-MgH_2 < pure MgH_2 < Al-doped γ-MgH_2 and (iii) pure β-MgH_2 < Al-doped β-MgH_2 < Si-doped β-MgH_2. For α phase Al doping decreases the H_2 desorption barrier the most by 30.5%. In the γ phase series the Si-doped MgH_2 (001) surface has the least E_{act} corresponding to a percentage decrease of 15.5%. In contrast doping β-MgH_2 causes a drastic increase in E_{act} from a value of 0.15 eV to 0.94 eV in case of Al doping and to 1.92 eV when doped with Si. Thus as opposed to the scenario of heats of formation, where Si doping consistently decreased ΔH_f of α, γ, and β phases, no particular trends are realized for E_{act}.

The difference in the effect of Al and Si doping on E_{act} and ΔH_f of α-MgH_2 necessitates tradeoffs. If the interest is in lowering ΔH_f then Si doping should be applied whereas if a much faster kinetics is desired then Al doping is the route to it. For γ-MgH_2 it is easily inferred that in order to improve its hydrogen storage properties Si should be the preferred choice of dopant as it lowers both the dehydrogenation reaction energy and activation energy barriers for H_2 removal. As Al and Si doping adversely affect the E_{act} of β-MgH_2, better results may thus be obtained by dehydrogenating it in pure form. Hence, for recognizing the true potential of dopants for enhancing the hydrogen storage properties of materials a combined study of their effect on the dehydrogenation reaction energies and the H_2 desorption kinetics is imperative.

4.4
Conclusions

Herein, we first performed a theoretical *ab initio* study of the dehydrogenation reaction energies of α- and β-$LiAlH_4$ and $LiBH_4$, α-, γ-, and β-MgH_2 and Al- and Si-substituted α-, γ-, and β-MgH_2. The enthalpies of formation of α- and β-$LiAlH_4$ and $LiBH_4$ calculated at 0 K conformed to the values known from experiments for the same reactions at 298 K. These enthalpies indicate that the α phases are more stable than the β phases and that substitution of B by Al decreases the stability of the complex metal hydride. The decreased reaction energies along with the smaller volume conclude that β-$LiBH_4$ is the complex metal hydride with most potential for hydrogen storage from the systems that we studied.

From the heats of formation (ΔH_f) calculated for the Al- and Si-substituted systems than for pure α-MgH_2 it was shown that the fractions $x = 0.167$ of Al, $x = 0.1, 0.167$ of Si (FCC) and $x = 0.0625, 0.1$ of Si (diamond) substitution cause an even greater destabilization of α-MgH_2 than Ti doping at a fraction of $x = 0.2$ This implies that Al and Si would result in a larger reduction of the its dehydrogenation temperature. Thus, Al and Si will be better substituents than Ti for enhancing the hydrogen storage properties of α-MgH_2.

Al and Si doping was also shown to decrease the ΔH_f of γ-and β-MgH_2. Amongst all the magnesium hydrides studied maximum lowering in ΔH_f was found for Si substitution of Mg in β-MgH_2. Futhermore we investigated the influence of doping Al and Si on the kinetics of these three phases of MgH_2 by density functional calculations using the plane wave-pseudopotential method. Activation energy barriers (E_{act}) for H_2 desorption from the (001) surfaces of unsubstituted and doped α-, γ-, and β-MgH_2 were computed. We found that the E_{act} did not exhibit any consistent trends with respect to doping with Al and Si. For α-MgH_2 trade-offs between lowering ΔH_f and faster kinetics might have to be made for choosing amidst Al and Si. In comparison γ-MgH_2 would benefit on both counts when doped with Si while β-MgH_2 would work best as a hydrogen storage material without any doping. It should be emphasized that a direct quantitative comparison between calculated E_{act} and the experimentally obtained barriers cannot be established due to the intricacy of the experimental kinetics. However, our calculated results do provide a simplistic approach for qualitatively analyzing the impact of Al and Si substitution on the thermodynamics as well as kinetics of H_2 release from MgH_2.

References

1. IEA/DOE/SNL Hydride Databases available at Hydride Information Center, Sandia National Laboratories Home Page. http://hydpark.ca.sandia.gov/
2. B. Bogdanovic, H. T. Hartwig and B. Spliethoff, *Int. J. Hydrogen Energy,* 1993, **18**, 575.
3. T. N. Dymova, D. P. Aleksandrov, V. N. Konoplev, T. A. Silina, and A. S. Sizareva, *Russ. J. Coord. Chem.* **1994**, *20*, 263.
4. J. J. Vajo, S. L. Skeith and F. Mertens, *J. Phys. Chem. B* **2005**, *109*, 3719.
5. O. Løvvik and O. Shang, *J. Alloys Compd.* **2004**, *404-406*, 757.
6. S. M. Opalka and D. L. Anton, *J. Alloys Compd.* **2003**, *356-357*, 486.
7. S. –C. Chung and H. Morioka, *J. Alloys Compd.* **2004**, *372*, 92.
8. O. Løvvik, S. M. Opalka, H. W. Brinks, and B. C. Hauback, *Phys. Rev. B* **2004**, *69*, 134117.
9. K. Miwa, N. Ohba, S. Towata, Y. Nakamori, and S. Orimo, *Phys. Rev. B* **2004**, *69*, 245120.
10. Y. Nakamori, K. Miwa, A. Ninomiya, H. Li, N. Ohba, S. Towata, A. Züttel, and S. Orimo, *Phys. Rev. B* **2006**, *74*, 045126.
11. P. Vajeeston, P. Ravindran, R. Vidya, H. Fjellvåg, and A. Kjekshus, *Cryst. Growth Des.* **2004**, *4*, 471.
12. J. J. Reilly and R. H. Wisall, *Inorg. Chem.* **1967**, *6*, 2220.
13. J. J. Reilly and R. H. Wisall, *Inorg. Chem.* **1968**, *7*, 2254.
14. J. Yang, A, Sudik, and C. Wolverton, *J. Phys. Chem. C* **2007**, *111*, 19134.
15. F. E. Pinkerton, G. P. Meisner, M. S. Meyer, M. P. Balogh, and M. D. Kundrat, *J. Phys. Chem. B* **2005**, *109*, 6.
16. M. Aoki, K. Miwa, T. Noritake, G. Kitahara, Y. Nakamori, S. Orimo, and S. Towata, *Appl. Phys. A* **2005**, *80*, 1409.

17. Y. E. Filinchuk, K. Yvon, G. P. Meisner, F. E. Pinkerton, and M. P. Balogh, *Inorg. Chem.* **2006**, *45*, 1433.
18. A. Zaluska, L. Zaluski, and J. O. Stro¨m-Olsen, *Appl. Phys. A* **2001**, *72*, 157.
19. J. J. Vajo, F. Mertens, C. C. Ahn, R. C. Bowman, Jr., and B. Fultz, *J. Phys. Chem. B* **2004**, *108*, 13977.
20. Y. W. Cho, J. Shim, and B. Lee, *CALPHAD: Comput. Coupling Phase Diagrams Thermochem.* **2006**, *30*, 65.
21. S. V. Alapati, J. K. Johnson, and D. S. Sholl, *J. Phys. Chem. B* **2006**, *110*, 8769.
22. W. Kohn and L. J Sham, *Phys. Rev.* **1965**, *140*, A1133.
23. S. V. Alapati, J. K. Johnson, and D. S. Sholl, *Phys. Rev. B* **2007**, *76*, 104108.
24. B. Bogdanović and M. Schwickardi, *J. Alloys Compd.* **1997**, *253*, 1.
25. J. Íñiguez, T. Yildrim, T. J. Udovic, M. Sulic, and C. M. Jensen, *Phys. Rev. B* **2004**, *70*, 060101(R).
26. C. M. Araújo, R. Ahuja, J. M. O. Guillén, and P. Jena, *Appl. Phys. Lett.* **2005**, *86*, 251913.
27. C. M. Araújo, S. Li, R. Ahuja, and P. Jena, *Phys. Rev. B.* **2005**, *72*, 165101.
28. S. Chaudhari, J. Graetz, A. Igantov, J. J. Reilly, and J. T. Muckerman, *J. Am. Chem. Soc.* **2006**, *128*, 11404.
29. G. Liang, J. Huot, S. Boily, A.van Neste, and R. Schultz, *J. Alloys Compd.* **1999**, *292*, 247.
30. N. Hanada, T. Ichikawa, and H. Fujii, *J. Phys. Chem. B* **2005**, *109*, 7188.
31. Y. Song, Z. X. Guo, and R.Yang, *Mater. Sci. Eng., A* **2004**, *365*, 73.
32. Y. Song, Z. X. Guo, and R.Yang, *Phys. Rev. B* **2004**, *69*, 094205.
33. P. Wang, A.M. Wang, B.Z. Ding, and Z.Q. Hu, *J. Alloys Compd.* **2002**, *334*, 243.
34. W. Oelerich, T. Klassen, and R. Bormann, *J. Alloys Compd.* **2002**, *322*, L5.
35. E. Ivanov, I. Konstanchuk, B. Bokhonov, and V. Boldyrev, *J. Alloys Compd.* **2003**, *359*, 320.
36. G. Barkhordarian, T. Klassen, and R. Bormann, *J. Alloys Compd.* **2004**, *364*, 242.

37. M. Güvendiren, E. Bayböru̇, and T. Öztürk, *Int. J. Hydrogen Energy* **2004**, *29*, 491.
38. M. Y. Song, J. -L. Bobet and B. Darriet, *J. Alloys Compd.* **2002***,* *340*, 256.
39. G. Barkhordarian, T. Klassen and R. Bormann, *Scr. Mater.* **2003**, *49*, 213.
40. M. Polanski, J. Bystrzycki and T. Plocinski, *Int. J. Hydrogen Energy* **2008**, *33*, 1859.
41. J. –j. Liang, *J. Alloys Compd.* **2007**, *446-447*, 72.
42. J. -P. Bastide, B. Bonnetot, J. -M. Létoffé and P. Claudy, *Mater. Res. Bull.* **1980**, *15*, 1215.
43. M. Bortz, B. Bertheville, K. Yvon, E. A. Movlaev, V. N. Verbetsky and F.Fauth, *J. Alloys Compd.* **1998**, *279*, L8.
44. M. Bortz, B. Bertheville, G. Böttger and K. Yvon, *J. Alloys Compd.* **1999**, *287*, L4.
45. P. Vajeeston, P. Ravindran, A. Kjekshus and H. Fjellvåg, *Phys. Rev. Lett*, **2002**, *89*, 1755061.
46. P. Vajeeston, P. Ravindran, B. C. Hauback, H. Fjellvåg, A. Kjekshus, S. Furuseth and M. Hanfland, *Phys. Rev. B* **2006**, *73*, 224102.
47. Y. Song and Z. X. Guo, *Appl. Phys. Lett.* **2006**, *89*, 111911.
48. R. H. Scheicher, D. Y. Kim, S. Lebègue, B. Arnaud, M. Alouani, and R. Ahuja, *Appl. Phys. Lett.* **2008**, *92*, 201903.
49. D. Y. Kim, R. H. Scheicher, S. Lebègue, J. Prasongkit, B. Arnaud, M. Alouani, and R. Ahuja, *Proc. Nalt. Acad. Sci. U.S.A.* **2008**, *105*, 16454.
50. R. A. Varin, T. Czujko and Z. Wronski, *Nanotech.* **2006**, *17*, 3856.
51. P. Vajeeston, P. Ravindran, H. Fjellvåg, and A. Kjekshus, *Phys. Rev. B* **2003**, *68*, 212101.
52. J. P. Perdew, J. A. Chevary, S. H. Vosko, K. A. Jackson, M. R. Pederson, D. J. Singh, and C. Fiolhais, *Phys. Rev. B* **1992**, *46*, 6671.
53. G. Kresse and J. Hafner, *Phys. Rev. B* **1993**, *47*, 558.
54. G. Kresse and J. Furthmüller, *Phys. Rev. B* **1996**, *54*, 11169.
55. D. Vanderbilt, *Phys. Rev. B* **1990**, *41*, 7892.
56. P. E. Blöchl, *Phys. Rev. B* **1994**, *50*, 17953.

57. G. Kresse and J. Furthmüller, *Comput. Mater. Sci.* **1996**, *6*, 15.
58. H. J. Monkhorst and J. D. Pack, *Phys. Rev. B* **1976**, *13*, 5188.
59. T. N. Dymova, D. P. Aleksandrov, V. N. Konoplev, T. A. Silina, and A. S. Sizareva, *Russ. J. Coord. Chem.* **1994**, *20*, 263.
60. K. Miwa, N. Ohba, S. Towata, Y. Nakamori, and S. Orimo, *Phys. Rev. B* **2004**, *69*, 245120.
61. M. J. van Setten, G. A. de Wijs, V. A. Popa, and G. Brocks, *Phys. Rev. B* **2005**, *72*, 073107.
62. K. Bohmhammel, U. Wolf, G. Wolf, and E. Königsberger, *Thermochim. Acta* **1999**, *337*, 195.
63. R. Griessen and A. Driessen, *Phys. Rev. B* **1984**, *30*, 4372.
64. F. D. Murnaghan, *Proc. Natl. Acad. Sci. U.S.A.* **1944**, *30*, 244.
65. A. J. Du, S. C. Smith, X. D. Yao and G. Q. Lu, *Surf. Sci.* **2006**, *600*, 1854.
66. J. F. Fernańdez and C. R. Sańchez, *J. Alloys Compd.* **2003**, *356-357*, 348.
67. N. Hanada, T. Ichikawa and H. Fujii, *J. Phys. Chem. B* **2005**, *109*, 7188.

CHAPTER 5

Effect of lattice vibrations at finite temperature

In every man's heart there is a secret nerve
that answers to the ***vibrations*** *of beauty.*
-Christopher Morley

The stability and static equation of state of magnesium hydride have been previously studied theoretically. However, it is important to go beyond the static calculations in order to assess the effect of temperature on its properties. Herein we present our results of Paper III in which the contribution of lattice vibrations at finite temperatures to free energy of magnesium hydride (MgH_2) were evaluated via the quasiharmonic approximation. In this chapter we begin by giving in Section 5.1 a brief description of the quasiharmonic approximation and the small displacement method used for determining the above mentioned lattice contributions. In the next section we outline the computational methodology employed. Our results from Paper III on the static and thermal equations of states and the temperature variation of certain thermodynamical properties of MgH_2 are reported in Section 5.3. Finally, the conclusions are given in the last section.

5.1
Introduction

Atomic vibrations contribute to thermal properties of all solids. For many solids there are no other appreciable contributions over a wide range of temperature. The vibrations are quantized, but at sufficiently high temperatures their statistical mechanics approaches the classical limit. In the limit of small amplitudes, the vibrations are harmonic and the motion can be expressed as the superposition of independent normal modes of vibration, each behaving as a linear harmonic oscillator. In reality the vibrations are of finite amplitude and so are not purely harmonic. However, they are approximately harmonic provided that the vibrational energy is small compared with the cohesive energy. Usually the harmonic approximation gives vibrational spectroscopic frequencies and heat capacities fairly accurately up to 20-30% of the melting temperature. However, even at the lowest temperature there is some departure from harmonic behavior, and it is this which is responsible for thermal expansion. An ideally harmonic solid would have a zero thermal expansion at all temperatures.

When anharmonicity is weak, its effect can be calculated by the *quasiharmonic approximation (QHA)* [1]. In QHA for each state of strain the vibrational contribution to the Helmholtz energy is calculated from the vibrational frequencies according to the harmonic approximation, and anharmonicity enters only through the strain-dependence of the frequencies. The different normal modes are still regarded as independent of each other, contributing separately to the thermodynamic properties as simple harmonic oscillators. The Helmholtz free energy F(V,T) is given by

$$F(V,T) = F_{static}(V) + F_{phon}(V,T) \tag{5.1.1}$$

where $F_{static}(V)$ is the energy of the static lattice at a given volume V and the vibrational contribution to it F_{phon} is:

$$F_{phon}(V,T) = \sum_{qi} \frac{1}{2} h\omega_{qj}(V) + k_B T \sum_{qj} \ln\left[1 - \exp\left(\frac{-h\omega_{qj}(V)}{k_B T}\right)\right] \qquad (5.1.2)$$

In Equation (5.1.2) ω_{qj} is the angular frequency $2\pi\nu_j$ of the jth normal mode at the point **q** in the Brillouin zone.

The strategy used for calculating the phonon frequencies is called the *small displacement method.* [2,3] The concept of this method is based on the facts that (i) the vibrational frequencies ω_{qj} are the eigenvalues of the dynamical matrix $D_{s\alpha.t\beta}(\mathbf{q})$ defined as:

$$D_{s\alpha,t\beta}(q) = \frac{1}{\sqrt{M_s M_t}} \sum_{l'} \Phi_{l s\alpha,l't\beta} \exp[iq.(R_{l'} + \tau_t - R_l - \tau_s)] \qquad (5.1.3)$$

where $\boldsymbol{R}_l + \tau_t$ represents the equilibrium position of atom *t* in primitive cell *l* and the sum is in principle over the infinite number of primitive cells in the crystal, and (ii) that $D_{s\alpha.t\beta}$ can be obtained directly using Hellmann-Feynman forces calculated with standard density functional theory (DFT) [4] codes.

For a crystal at very low temperature, its potential energy U_{harm} can be expanded around the equilibrium positions of the nuclei. At the minimum energy configuration the linear term of this expansion will be zero so that:

$$U_{harm} = E_{perf} + \frac{1}{2} \sum_{l s\alpha,l't\beta} \Phi_{l s\alpha,l't\beta} u_{l s\alpha} u_{l't\beta} \qquad (5.1.4)$$

where E_{perf} is the energy of the system with ions in their equilibrium positions, u_{ls} is the displacement of atom *s* in unit cell *l*, *α* and *β* are Cartesian components, and $\Phi_{ls\alpha,l't\beta}$ is the force-constant matrix, given by $\partial^2 U/\partial u_{ls\alpha}\partial u_{l't\beta}$ evaluated with all atoms at their equilibrium positions. $\Phi_{ls\alpha,l't\beta}$ gives the relation between the forces $F_{ls\alpha}$ and the displacements $u_{l't}$. In the small displacement method, the forces $F_{ls\alpha}$ on all atoms are calculated by displacing a single atom *t* in cell *l′* while keeping all other atoms fixed in their equilibrium positions. This procedure is repeated for all other displacements for obtaining all the elements of the force-constant matrix. The number of such calculations required is reduced significantly on the basis of symmetry.

First-principles calculations based on DFT have been widely used to predict the ground state properties of magnesium hydride. Electronic and structural properties of MgH_2 have been previously calculated using *ab initio* pseudopotential methods. [5-8] Density functional investigations performed to study H_2 desorption from a MgH_2 cluster reported a high activation barrier of 3.30 eV as a result of the ionic bonding in Mg-H. [9] The effect of cluster size on thermodynamic stability of Mg and MgH_2 has also been studied using DFT. [10] The calculations showed that MgH_2 was destabilized more than Mg on decreasing the cluster size to less than 19 Mg atoms implying a significantly lower desorption temperature in such small MgH_2 clusters. A cluster of 0.9 nm was predicted to correspond to a desorption temperature of 473 K.

All of the above studies were carried out at 0 K. This motivated us to examine the effect of temperature on the equation of state (EOS) and thermodynamic properties of MgH_2 by employing QHA. However, QHA is known to work well for temperatures lower than the melting point of the system under investigation. Thus, we also set out to test the validity of QHA in the high temperature regime for MgH_2. To this end we calculated thermal EOS parameters such as the lattice constant, equilibrium cell volume V_0, bulk modulus K_0 and its pressure derivative K_0' and thermodynamic quantities like entropy S, internal energy E, heat capacity C_P, thermal pressure $P_{thermal}$ and volume thermal expansion $\Delta V/V(\%)$ of MgH_2 using first-principles method over a wide temperature range of 0-1000 K that includes temperatures greater than its melting temperature (573 K).

5.2
Computational details

We used the Vienna *ab initio* simulations package (VASP) [11,12] for performing all the static calculations. These calculations were based on DFT within the generalized gradient approximation (GGA) [13,14]. The interactions between ions and electrons were described through Vanderbilt US-PPs [15,16] provided with VASP. The Kohn-Sham equations were solved iteratively to self-consistency within 10^{-4} eV/Å. To check the degree of convergence of the total energy, the Brillouin zone (BZ) sampling was performed for 4 x 4 x 4, 6 x 6 x 6, 8 x 8 x 8 and 10 x 10 x 10 **k**-point Monkhorst-Pack [17] meshes. The 6 x 6 x 6 **k**-point mesh yielded a total energy that was within 0.1 meV of the values obtained when denser 8 x 8 x 8 and 10 x 10 x 10 **k**-point grids were used. Therefore, for all static calculations the sums over BZ were performed using 6 x 6 x 6 **k**-points. Convergence of total energy with respect to the plane wave (PW) cut-off energy was studied. For the 6 x 6 x 6 **k**-point mesh the total energy at a PW cut-off of 440 eV agreed within 0.4 meV and 0.65 meV of the values calculated with cut-offs 460 eV and 480 eV, respectively. Thus, 440 eV was chosen as the cut-off energy to be employed in all the calculations.

The Pulay stress problem is known to arise during energy-volume calculations or cell shape and volume relaxations due to the fact that the PW basis set is not complete with respect to changes of the volume. This problem was avoided here by performing structure relaxations at fixed volumes rather than under constant pressures using the same energy cut-off of 440 eV. For each volume the structure was fully relaxed to optimize all internal coordinates and cell shape. The final energies were then fit to the Murnaghan EOS [18],

$$F(V,T) = F(V_0) + \frac{K_0 V}{K_0^{'}(K_0^{'} - 1)}\left[K_0^{'} - 1 + \left(\frac{V_0}{V}\right)^{K_0^{'}}\right] - \frac{K_0 V_0}{K_0^{'} - 1} \qquad (5.2.1)$$

The above EOS is parameterized by the equilibrium volume V_0, the isothermal bulk modulus K_0 and its pressure derivative $K_0^{'}$. These calculated EOS parameters were then used as input in the EOSFIT [19] program for deriving the total pressure of the system at different volumes. Thermal pressure $P_{thermal}(V,T)$ which accounts for the isochoric effect on pressure [20] was then calculated as the difference between the total pressure and the static pressure:

$$P_{thermal}(V,T) = P(V,T) - P(V) \qquad (5.2.2)$$

For evaluating the vibrational contribution to free energy F_{phon} (see Equation (5.1.1)) first the forces on the atoms of the 2 x 2 x 1 MgH_2 supercell as they are displaced from their ground state positions were obtained using VASP. These were then input into PHON [21] for generating the force constants, the dynamical matrix, the phonon frequencies and phonon density of states (DOS) by the small displacement method as implemented in PHON. The phonon DOS were calculated with a 24 x 24 x 12 **k**-point mesh and were then used to compute the vibrational contribution to free energy (F_{phon}) for a series of temperatures between 0 K and 1000 K. F_{phon} was next added to the static free energy F(V) to obtain the total free energy F(V,T) as a function of volume and temperature, defined in Equation (5.1.1). Fit of F(V,T) versus volume data at different temperatures to the Murnaghan EOS (Equation (5.2.1)) yielded the temperature dependent material properties of MgH_2. From F(V,T) other thermodynamic quantities such as internal energy E, entropy S and heat capacity at constant volume C_v were next derived by applying the following relations:

Entropy $$S = -\left(\frac{\partial F}{\partial T}\right)_{V,P} \qquad (5.2.2)$$

Internal energy $$E = F + TS \qquad (5.2.3)$$

Heat capacity $$C_V = \left(\frac{\partial E}{\partial T}\right)_V \qquad (5.2.4)$$

5.3
Results and discussion

5.3.1
Static equation of state

From the fit of the total energy versus cell volume data of the static lattice to the static EOS the following parameters were determined: V_0 = 60.85 $Å^3$, K_0 = 47.445 GPa, and K_0' = 3.594. Table 5.1 shows that our values compare well with those previously

Table 5.1 Selected bond distances and bond angles and optimized lattice parameters of MgH_2 computed from static calculations.

Parameter	*This work*	*Experimental value (Ref. 22)*	*Theoretical value (Ref. 22)*
V_0(Å^3)	60.85		60.33
K_0	47.445	45±2	51
K_0'	3.594	3.353±0.3	3.45
a (Å)	4.497	4.5176	4.4853
b (Å)	4.507	4.5176	4.4853
c (Å)	3.002	3.0205	2.9993
Mg-H (Å)	1.9387		1.944
	1.9498		1.961
H-Mg-H (deg)	90.0		

reported in a combined theoretical and high pressure X-ray diffraction study [22]. Some selected bond distances and bond angles of the optimized geometry at V_0 = 60.85 Å^3 are also listed in the table. We also calculated the cohesive energy of this ground state structure of MgH_2 as the difference between the total energy of the crystal and that of the atoms. For obtaining the total energy of the free atoms Γ-point was used and the atoms were placed in a simple cubic unit cell of size 10 Å. The cohesive energy of MgH_2 (6.73 eV/f.u.) thus evaluated was found to be close to the experimental cohesive energy 6.7 eV/f.u. as given in Ref. [5]. The agreement between the calculated and experimental data demonstrates the reliability of our calculations. In our optimization calculations reported so far vibrational effects were not taken into account.

5.3.2
Lattice dynamics

To determine the phonon DOS of MgH_2 first the vibrational frequencies were determined at a series of volumes. The predicted dispersion curve along several symmetry directions in the BZ zone obtained at the static ground state volume V_0 =

30.425 Å^3/f.u. is shown in Fig. 5.1. We compared these calculated phonon frequencies with experimental and theoretical data. Experimental data obtained from Raman spectra [23] are 300, 950, and 1276 cm^{-1}. The Raman active modes deduced by Ohba et al. [24] by first-principles calculations were at 299, 977, and 1291cm^{-1}. Our calculated values of 962 and 1314 cm^{-1} in the high frequency region agreed within ~3% of these computed results. Our low frequency Raman mode of 281 cm^{-1} showed a deviation of ~6%.

Further, the total and partial phonon DOS at the computed static equilibrium

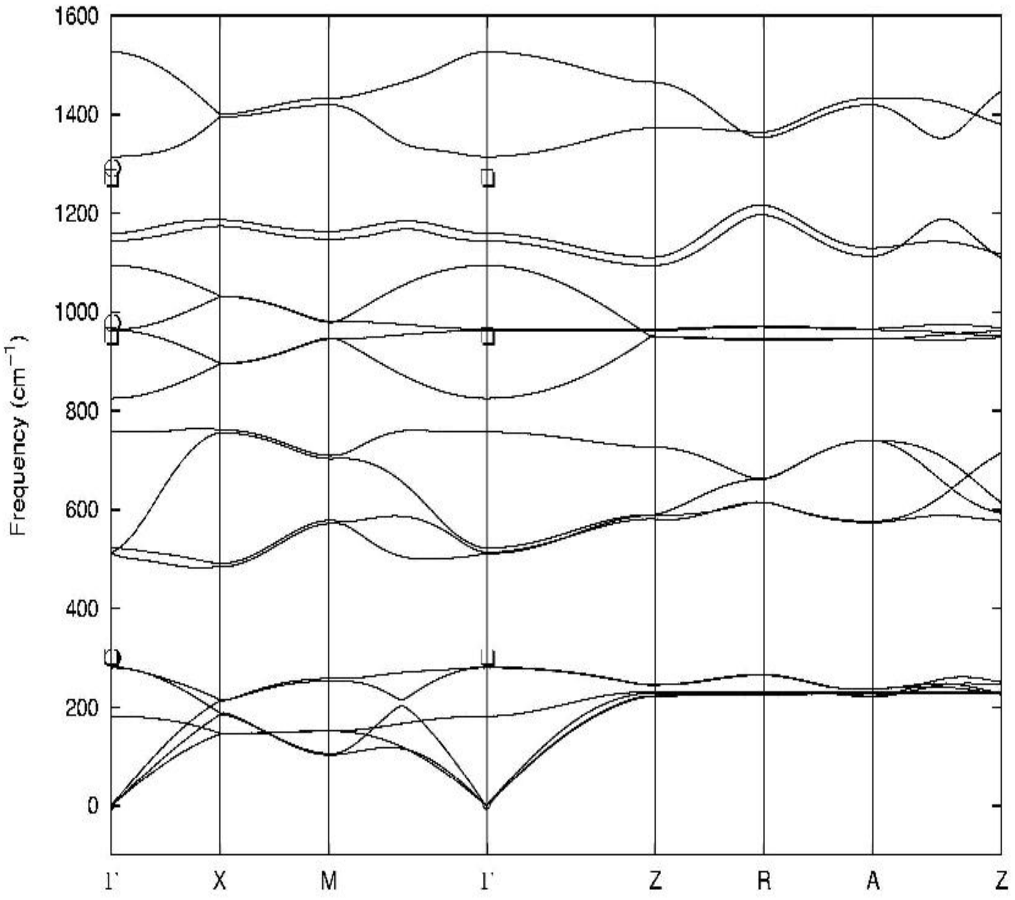

Figure 5.1 Calculated phonon dispersion curve along several high symmetry directions at the static equilibrium cell volume V_0 = 30.425 Å^3/f.u. Theoretical data (Ref. 24) are represented by circles and experimental data (Ref. 23) are denoted by squares.

cell volume V_0 = 30.425 Å^3/f.u. were generated and these are displayed in Figs. 5.2 (a)-(c). At this volume the total phonon DOS is divided into four broad ranges separated by three gaps between 300-450 cm^{-1}, 800-820 cm^{-1} and 1220-1320 cm^{-1}. As the mass of H atom is much smaller than that of Mg atom, the partial phonon DOS show that the high frequency modes (above 450 cm^{-1}) are dominated by H atoms while the low frequency modes (below 300 cm^{-1}) are dominated by Mg atoms with these modes being separated by a gap of nearly 200 cm^{-1}. The absence of coupling between the vibrations of the two atoms is understandable in terms of the ionic interaction between H and Mg atoms in MgH_2.

For V = 35.0 Å^3/f.u. there are two significant band gaps in the total phonon DOS plot between 250-400 cm^{-1} and 1000-1170 cm^{-1}. The center of the low frequency modes was shifted to a lower frequency value 150 cm^{-1} as compared to that for V_0. Therefore the separation between the high frequency modes due to H atoms and the low frequency modes due to Mg atoms still increases. Further the H atoms do not contribute in the region between 0-250 cm^{-1} implying absence of coupling between H and Mg atom vibrations.

The total phonon DOS for V = 25.0 Å^3/f.u. can be divided into three broad ranges separated by two band gaps between 800-1000 cm^{-1} and 1300-1400 cm^{-1}. The high frequency modes beyond 400 cm^{-1} are purely due to vibrations of H atoms. We note that the center of the low frequency modes which was initially at ~200 cm^{-1} for V_0 shifted to a higher frequency value 300 cm^{-1}. The low frequency modes though continue to be dominated by Mg atoms, now also have contributions from vibrations of H atoms. As a result a mild coupling occurs between the vibrations of Mg and H atoms in the 200-300 cm^{-1} region.

Summarizing, as the cell volume was reduced the interaction between H and Mg atoms increased as the partial DOS were found to overlap in the low frequency region. The overall picture of ionic bonding in MgH_2 however remained unchanged as the Mg atoms dominated the low frequency modes while the high frequency modes arose purely due to H atoms.

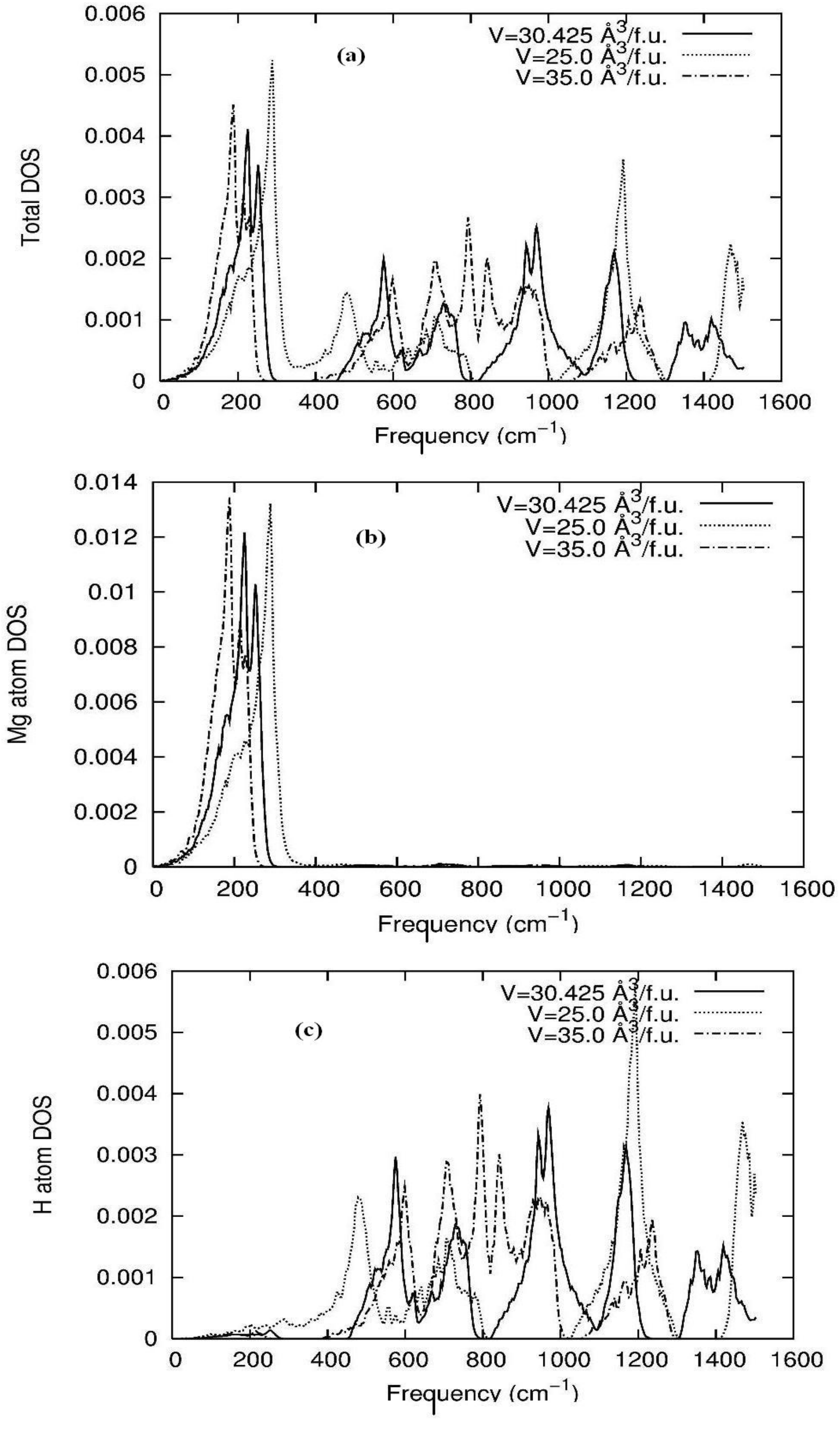

Figure 5.2 The calculated (a) total, (b) Mg atom, and (c) H atom phonon density of states at cell volumes 25.0, 30.425 and 35.0 Å^3/f.u.

5.3.3
Thermal equations of state

Equations (5.1.1) and (5.1.2) were used to compute the Helmholtz free energy F(V,T) as a function of V and T. A range of temperatures between 0 K and 1000 K were considered. This range also included temperatures beyond 573 K, that is, the temperature at which MgH_2 dissociates into Mg and H_2. This regime was chosen so as to put to test through our calculations the goodness of QHA for MgH_2 at both high and low temperatures.

The energy-volume curves at temperatures T = 0, 298, 500, and 900 K derived after fitting to Murnaghan EOS are displayed in Fig. 5.3. It can be clearly seen from the plots that at each volume, higher the temperature more negative is the free energy. This behaviour was interpreted by rearranging Equation (5.2.3) as: F = E – TS. Figures 5.4 (a) and (b) show the temperature variation of E and TS. Both E and TS

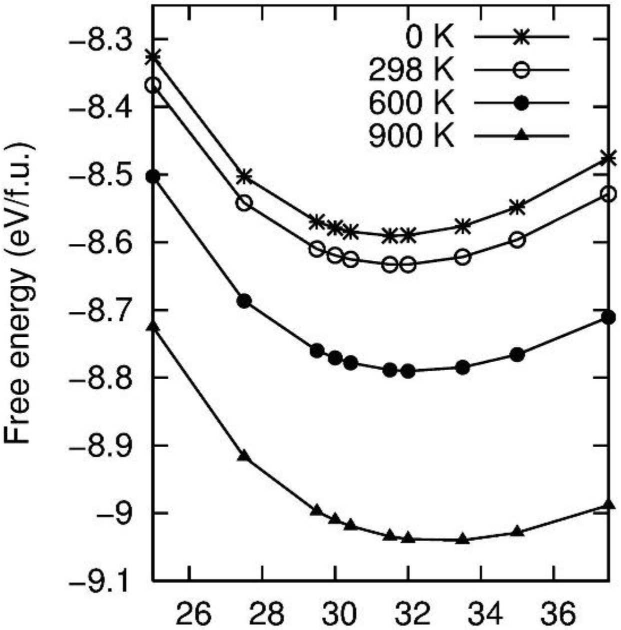

Figure 5.3 The thermal equations of state derived for T = 0, 298, 600 and 900 K, respectively, by fitting the cell volume-Helmholtz free energy data to the Murnaghan EOS at each temperature.

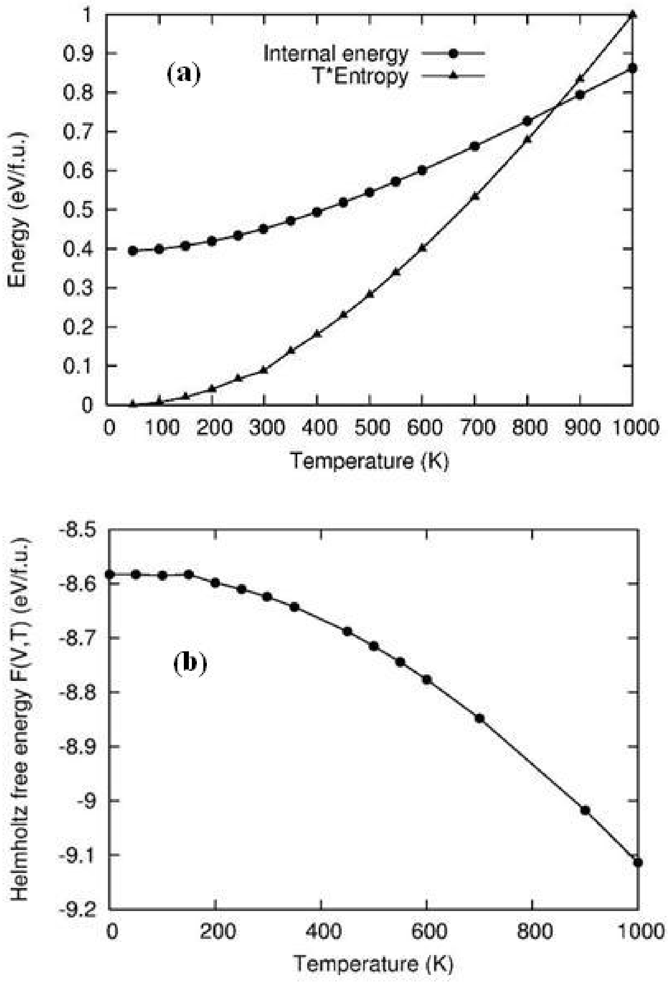

Figure 5.4 Temperature dependence of (a) internal energy E and product of temperature and entropy T*S and (b) Helmholtz free energy F(V,T) at V_0= 30.425 $Å^3$/f.u.

increase with temperature but the slope of the curve for TS is greater than that of E. The rise in TS more than compensates for the rise in E and hence, F(V,T) decreases with increase in temperature as exhibited in Fig. 5.3.

Table 5.2 lists the equilibrium cell volume, bulk modulus and its pressure derivative calculated at different temperatures by the thermal EOS fits. Comparison with the static EOS results showed that inclusion of vibrational effects significantly

Table 5.2 Static and thermal equations of state parameters, namely, equilibrium cell volume V_0, bulk modulus K_0 and pressure derivative K_0' of bulk modulus calculated at different temperatures.

Temperature (K)	*V_0 (Å^3/f.u.)*	*K_0 (GPa)*	*K_0'*
Static	30.43	47.445	3.594
0	31.59	42.867	3.498
298	31.77	41.031	3.427
350	31.82	40.715	3.617
500	32.02	38.037	3.789
900	32.91	32.650	4.103

altered the equation of state. The effect of zero point motion and temperature is to increase V_0 by ~4% relative to the athermal values. Our calculated value of V_0 at 298 K differs by as much percentage from the experimental [25] V_0 at 260 K.

The heat capacity at constant pressure C_P is calculated as:

$$C_P = C_V + \alpha^2 VTK_0(T) \qquad (5.3.1)$$

in terms of heat capacity at constant volume C_v and the thermal expansivity α which is defined as,

$$\alpha = \frac{a(T) - a(0)}{a(0) * T} \qquad (5.3.2)$$

In the above equation *a(T)* and *a(0)* are the lattice parameters at temperatures T and 0 K, respectively. Our computed entropies and C_P's at a series of temperatures for the ground state equilibrium cell volume V_0 = 30.425 Å^3/f.u. are compared with experimental data [26] in Table 5.3. The table demonstrates that at all temperatures our

Table 5.3 Thermodynamical properties (entropy and specific heat capacity at constant pressure) calculated at different temperatures, compared with experimental data (Ref. 26).

Temperature (K)	***S ($Jmol^{-1}K^{-1}$)***		***C_P ($Jmol^{-1}K^{-1}$)***	
	Present work	***Ref. 26***	***Present work***	***Ref. 26***
298	31.60	31.01	36.04	35.26
500	54.40	53.06	52.06	49.99
600	64.35	62.65	57.12	55.18
700	73.45	71.49	60.83	59.44
800	81.75	79.66	63.57	62.92
900	89.35	87.24	65.64	65.72
1000	96.33	94.28	67.24	67.95

calculated entropies show a reasonable agreement within 2.5% of the reference values and lend confidence in our computations. At 298 K and cell volume V_0 = 30.425 $Å^3$/f.u. our calculated entropy 36.6 $JK^{-1}mol^{-1}$ is very close to the experimentally measured value of 36.01 $JK^{-1}mol^{-1}$. The predicted heat capacities at 500 and 600 K show a deviation of 4.1% and 3.5% from the corresponding reference values. But at all other temperatures the proximity between the calculated and experimental heat capacities is within 2.5%. This suggests that QHA may be used as a tool for computing the thermodynamical properties of MgH_2 to a reasonable degree of accuracy at low as well as high temperatures which are away from its melting point of 573 K.

The thermal pressure $P_{thermal}(V,T)$ was evaluated using the Equation (5.2.2) in the same volume and temperature ranges in which the EOS were predicted. Figures 5.5 (a) and (b) display the volume and temperature dependence of $P_{thermal}(V,T)$ of MgH_2. At 0 K the thermal pressure decreases linearly with volume. At T = 298 K and

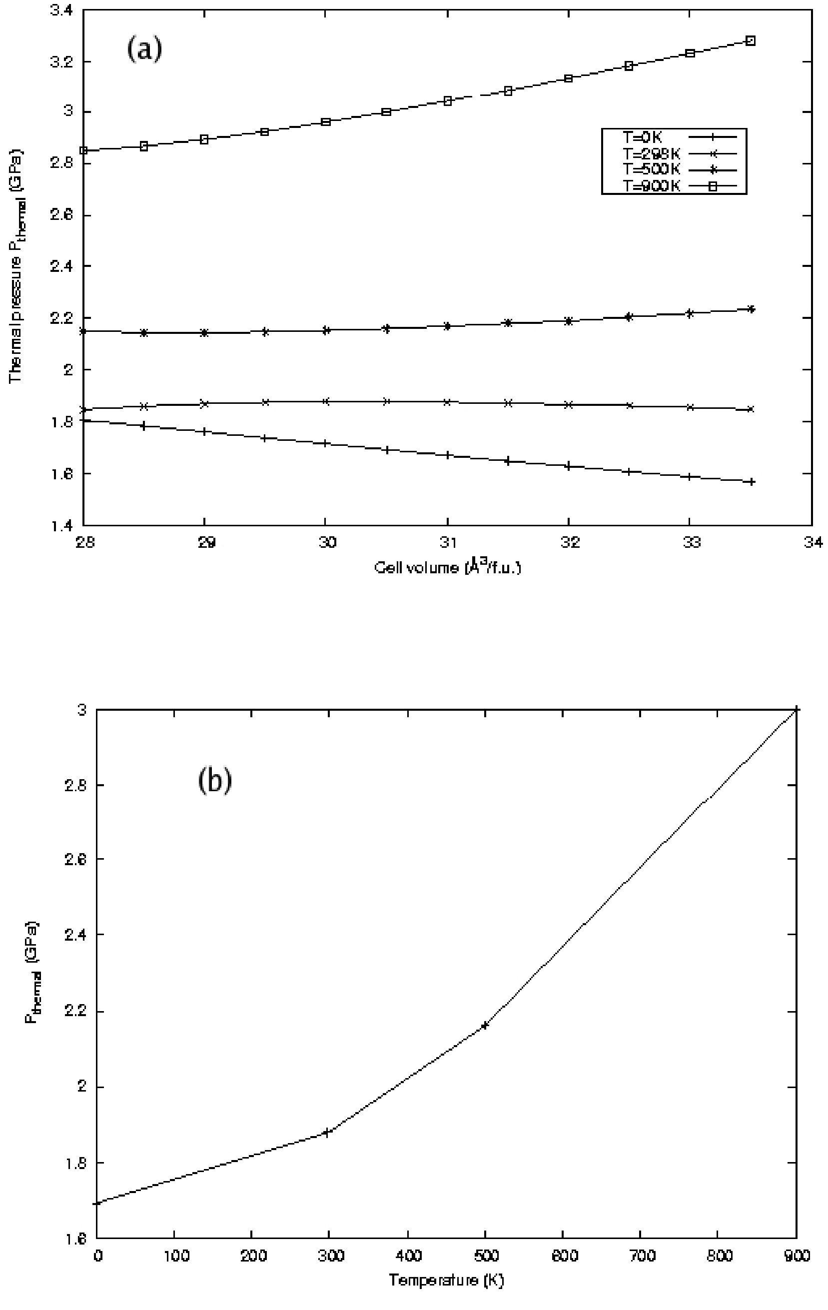

Figure 5.5 Thermal pressure as a function of (a) cell volume at different temperatures and (b) temperature at constant volume $V_0 = 30.425$ Å^3/f.u.

500 K however, $P_{thermal}(V,T)$ becomes a slowly varying function of volume. But as temperature was increased further to 900 K it began to exhibit a monotonic increase with cell volume. In comparison the thermal pressure increased strongly with increasing temperature at all the volumes that were considered. This indicates that within the temperature range of 298-500 K $P_{thermal}(V,T)$ is expected to be volume independent.

Using first-principles lattice dynamical calculations Karki [27] found a much smaller variation of thermal pressure with compression as compared to its variation with temperature for MgO and $MgSiO_3$. As a result he concluded that at high temperatures the volume-induced variations of $P_{thermal}(V,T)$ can be neglected for these minerals to a good approximation and that the thermal equations of state can be constructed from the knowledge of $P_{thermal}(V_0,T)$ and a room temperature isothermal compression. Hence, we too suggest the possible estimation of the equations of state for MgH_2 for temperatures lying in the range 298-500 K by using the measured $P_{thermal}(V,T)$ versus temperature data at ambient pressure and isothermal compression data at ambient temperature.

Using the equilibrium cell volumes predicted for different temperatures $V_0(T)$ the volume thermal expansion was determined as follows:

$$\frac{\Delta V}{V}(\%) = \frac{V_0(T) - V_0(298\text{ K})}{V_0(298\text{ K})} \text{ x } 100 \tag{5.3.2}$$

Figure 5.6 depicts the temperature dependence of the volume thermal expansion thereby obtained. The plot shows that at 350 K $V_0(T)$ increases by 0.17%. Using a similar expression as Equation (5.3.2) we calculated we calculated a decrease in K_0 of 0.77% from the values listed in Table 5.2. From the Fig. 5.6 it is noticeable that as temperature increases the volume thermal expansion also increases. The corresponding percentage decrease in K_0 and a consequent increase in compressibility were found to be greater in comparison. For instance, at 500 K the volume thermal expansion was simply 0.81% to while the calculated decrease in K_0 was 5.55%. Hence, we suggest application of temperatures higher than 298 K as a way of

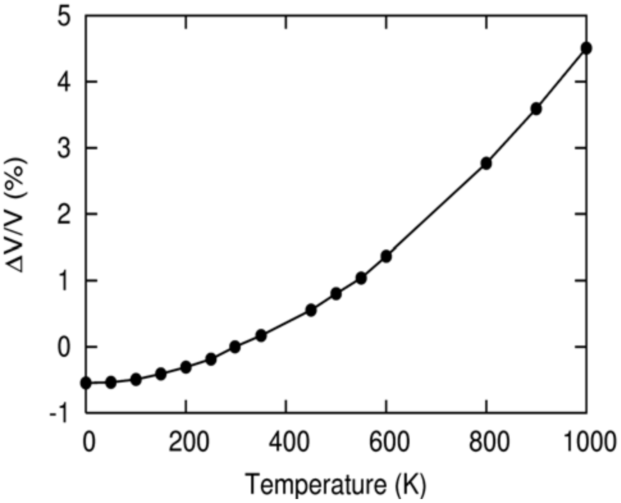

Figure 5.6 Temperature dependence of volume thermal expansion of MgH_2 at cell volume $V_0 = 30.425$ Å^3/f.u.

improving the volumetric hydrogen storage capacity of MgH_2 as a consequence of its better compressibility.

5.4
Conclusions

Free energies were calculated from phonon dispersions as a function of cell volume and temperature within the quasiharmonic approximation (QHA) for MgH_2. From the free energies the equations of state were determined for temperatures up to 1000 K. The temperature dependence of EOS parameters (equilibrium cell volume V_0, bulk modulus K_0 and its pressure derivative K_0') and several thermodynamical quantities such as internal energy E, entropy S, heat capacity at constant pressure C_P, volume thermal expansion ΔV/V(%), and thermal pressure $P_{thermal}(V,T)$ were determined. The temperature dependence of S and C_P was found to be in reasonable agreement with the experimental results thereby exhibiting QHA as a theoretical approach for calculating these quantities even at temperatures greater than the melting point of MgH_2. At 0 K $P_{thermal}(V,T)$ decreased linearly and at 900 K it increased monotonically with cell volume. In comparison within the temperature range of 298-500 K

$P_{thermal}(V,T)$ was found to be volume independent. The calculated percentage decrease in K_0 with temperature superseded the percentage increase in V_0 as reflected by $\Delta V/V(\%)$. From our calculations it was evident that the increase in compressibility as indicated by the decrease in K_0 will offset the effect of increase in V_0 even at temperatures moderately higher than 298 K. This presents a potential approach of application of a temperature slightly greater than room temperature for enhancing the volumetric hydrogen storage capacity of MgH_2.

References

1. A. A. Maradudin, E. W. Montroll, G. H. Weiss, and I. P. Ipatova, *Theory of Lattice Dynamics in the Harmonic Approximation* **1971**, 2nd ed. (Academic, New York).
2. G. Kresse, J. Furthmüller, and J. Hafner, *Europhys. Lett.* **1995**, *32*, 729.
3. D. Alfè, G. D. Price, and M. J. Gillan, *Phys. Rev. B* **2001**, *64*, 045123.
4. P. Hohenberg and W. Kohn, *Phys. Rev.* **1964**, *136*, 864.
5. R. Yu and P. K. Lam, *Phys. Rev. B* **1988**, *37*, 8730.
6. P. Vajeeston, P. Ravindran, A. Kjekshus, and H. Fjellvåg, *Phys. Rev. Lett.* **2002**, *89*, 175506.
7. C. M. Araüjo, S. Lebègue, O. Eriksson, B. Arnaud, M. Alouani, and R. Ahuja, *J. Appl. Phys.* **2005**, *98*, 096106.
8. Y. Song and Z. X. Guo, *Appl. Phys. Lett.* **2006**, *89*, 111911.
9. M. Tsuda, W. A. Dinö, H. Nakanishi, and H. Kasai, *J. Phys. Soc. Japan* **2004**, *73*, 2628.
10. R. W. P. Wagemans, J. H. van Lenthe, P. E. de Jongh, A. J. van Dillen, and K. P. de Jong, *J. Am. Chem. Soc.* **2005**, *127*, 16675.
11. G. Kresse, J. Furthmüller, and J. Hafner, *Europhys. Lett.* **1995**, *32*, 729.
12. G. Kresse and J. Furthmüller, *Phys. Rev. B* **1996**, *54*, 11169.
13. J. P. Perdew and Y. Wang, *Phys. Rev. B* **1992**, *45*, 13244.
14. J. P. Perdew, J. A. Chevary, S. H. Vosko, K. A. Jackson, M. R. Pederson, D. J. Singh, and C. Fiolhais, *Phys. Rev. B* **1992**, *46*, 6671.
15. D. Vanderbilt, *Phys. Rev. B* **1990**, *41*, 7892.

16. K. Laasonen, R. Car, C. Lee, and D. Vanderbilt, *Phys. Rev. B* **1991**, *43*, 6796.
17. H. J. Monkhorst and J. D. Pack, *Phys. Rev. B* **1976**, *13*, 5188.
18. F. D. Murnaghan, *Proc. Natl. Acad. Sci. U.S.A.* **1944**, *30*, 244.
19. R. J. Angel, *Rev. Miner. Geochem.* **2001**, edited by R. M. Hazen and R. T. Downs, vol. *41*, pp. 35-59 (Mineralogical Society of America, Washington); http://www.crystal.vt.edu/crystal/software.html
20. O. L. Anderson, O. L. *J. Phys. Chem. Solids* **1997**, *58*, 335.
21. D. Alfé, G. D. Price, and M. J. Gillan, *Phys. Rev. B* **2001**, *64*, 045123; http://chianti.geol.ucl.ac.uk/~dario
22. P. Vajeeston, P. Ravindran, B. C. Hauback, H. Fjellvåg, A. Kjekshus, S. Furuseth, and M. Hanfland, *Phys. Rev. B* **2006**, *73*, 224102.
23. J. R. Santisteban, G. J. Cuello, J. Dawidowski, A. Fainstein, H. A. Peretti, A. Ivanov, and F. J. Bermejo, J. *Phys. Rev. B* **2000**, *62*, 37.
24. N. Ohba, K. Miwa, T. Naritake, and A. Fukumoto, *Phys. Rev. B* **2004**, *70*, 035102.
25. M. Bortz, B. Mertheville, G. Böttger, and K. Yvon, *J. Alloys Compd.* **1999**, *287*, L4.
26. Jr. M. W. Chase, *NIST-JANAF Thermochemical Tables*, Fourth Edition; *J. Phys. Chem. Ref. Data* **1998**, *Monograph 9*, 1-1951.
27. B. B. Karki, *Am. Miner.* **2000**, *85*, 1447.

CHAPTER 6

Doped metal-organic framework-5

In life to be happy
drop the words "if only"
and ***substitute*** *instead*
the words "next time.".
-Anonymous

There has been increased interest in metal-organic frameworks (MOFs) as hydrogen storage materials because of their various positive characteristics such as high porosity, reproducible and facile syntheses, amenability to scale-up, and chemical modification for targeting desired properties. An important challenge for creating practical hydrogen adsorbents is increasing the room temperature hydrogen binding energy and hydrogen uptake within MOFs. Herein we present our results of Paper V in which a preliminary study of the effect of various light metal dopants on the thermodynamics of hydrogen adsorption in MOF-5 has been carried out by modeling the interactions of its organic linker with the metal ions and hydrogen molecules. This study is expected to give incite regarding the trends likely to arise in the actual systems.

We begin in Section 6.1 by giving a brief introduction regarding MOFs and the strategy of doping used to enhance their hydrogen storage capacities. The computational methodology employed in this work is described in Section 6.2. In the next section, a discussion on the significant results of our study is provided. Finally, the conclusions are presented in the last section.

6.1
Introduction

Metal-organic frameworks (MOFs) are high surface area nanoporous materials which can adsorb guest molecules and therefore hold great promise for storage of hydrogen (H_2). [1] Typically the interaction between physisorbed H_2 molecules and MOFs is weak with H_2 adsorption enthalpies in the range of 3.5-5.2 kJ/mol [2-4] As a result MOFs exhibit fast H_2 desorption kinetics as well as a reversible H_2 uptake and release. But this low interaction energy also implies that for achieving a significant H_2 storage capacity low temperatures are needed. For example, at 77 K and moderate pressures MOF-5 [5], [Cu(L_2)(H_2O)$_2$] where L_2=terphenyl-3,3'',5,5'-tetracarboxylate) [6], MOF-177 [7, 8], IRMOF-20 [9, 10], and MIL-101 [10, 11] have hydrogen uptake in the range of 4.5-7.5 wt.% H_2. But at room temperature their storage capacities fall below 1.5 wt.%. Thus, clearly today much research in MOFs is devoted to strengthening the H_2 interaction energies and to increasing H_2 adsorption and storage capacity to significant levels at or around room temperature. However, to tune H_2 storage in MOFs it is imperative to understand the fundamental interactions that lead to adsorption.

Kuc et al. [12, 13] have examined the role of the non-bonding interactions, London dispersion interactions, and electrostatic interactions in IRMOF-1 by reducing the MOF structure to clusters for modeling the MOF connectors and linkers. Their calculations illustrated that the physisorption of H_2 in MOFs is mainly due to London dispersion between linkers and connectors with hydrogen. In contract the host–guest induced electrostatic interactions were found to be unimportant, as the charge separation in the MOF is not large enough to induce significant dipole moments in H_2. Thus methods based on density functional theory (DFT) [14] which are unable to correctly describe dispersion forces and van der Waals interactions may face challenges in studying MOFs. Recently, Rapacioli et al. [15] devised a strategy to introduce these necessary corrections in the density functional tight binding (DFTB) method due to which they were able to successfully obtain results for benzene dimer in agreement with CCSD(T) calculations.

An approach being currently pursued to enhance H_2 adsorption in MOFs involves cation doping. Many theoretical studies have focused on the interactions of H_2 molecules with transition metal ions. [16-19] Noteworthy is the investigation by Gagliardi and Pyykko [20] which showed that bare neutral and cationic transition metals such as Cr, Mn^+, W, Mo, V^+,and Ti^{2+} can bind with as many as six H_2 molecules. Interestingly Chandrakumar and Ghosh [21] demonstrated that s-block metal cations can form $M(H_2)_8$ complexes. Thus M = Li^+, Na^+, K^+, Be^{2+}, Ca^{2+}, and Mg^{2+} ions are predicted to adsorb even more number of H_2 molecules than the above transition metal ions. The interaction of H_2 molecules with these s-block metal ions, though found to be weaker than with transition metal ions, is much stronger than with MOFs. The calculated binding energies for the alkali and alkaline earth metal ions were of the order of -30 kcal/mol to -13.5 kcal/mol and -180 kcal/mol to -60 kcal/mol. However, manufacturing such bare metals ions in reality is difficult. As an alternative, the metal ions can be stabilized by adsorbing them of surfaces with strong electron affinities.

This metal ion decoration approach has already been successfully applied to fullerenes and nanotubes. First-principles DFT calculations have shown that Ti^+ ion doped on Si_6H_{60} fullerene [22] and on BC_4N [23] nanotube can adsorb a maximum of four H_2 molecules with successive binding energies lying in the suitable range between the physisorption and chemisorption energies. Chandrakumar and Ghosh [24] have shown that doping C_{60} with Na has a stronger effect than doping with Li on its H_2 adsorption capacity and that with a high metal coverage of eight Na atoms 48 H_2 molecules can be adsorbed totally leading to a gravimetric storage capacity of ~9.5 wt.%.

Significant improvement in molecular H_2 uptake properties have also been predicted for Li-decorated MOF-5 by Blomqvist et al. [25] Using *ab initio* periodic DFT calculations they showed that each Li adsorbed over the benzene ring can cluster up to three H_2 molecules with a binding energy of 12.0-18.0 kJ/mol H_2. *Ab initio* molecular dynamics simulations revealed that a hydrogen uptake of 2.9 wt.% and 2.0 wt.% could be achieved even at high temperatures of 200 K and 300 K, respectively. Recently, Venkataramanan et al. [26] have explored isoreticular MOFs with different metals M = Fe, Cu, Co, Ni and Zn through DFT and predicted that Li doping will be possible only in Zn-based MOFs.

Materials such as carbon nanotubes, fullerenes, and MOFs can also be investigated by applying polycyclic aromatic hydrocarbons (PAHs) as models. In one such exhaustive quantum chemical study Srinivasu and co-workers [27] have considered the following model systems: C_6H_6, NH_2-C_6H_5, CH_3-C_6H_5, COOH-C_6H_5, CN-C_6H_5, and NO_2-C_6H_5 and examined the effect of (a) doping with light metal ions (Li^+ and Na^+), (b) functional groups in the models, and (c) curvature. It was concluded that ionic surface with a significant degree of curvature will enhance hydrogen adsorption more effectively. Of particular substance is their recent detailed analysis of the role played by nanoscale curvature [28] and aromaticity [29] in inducing H_2 adsorption in alkali metal doped carbon nanomaterials.

Even though some of the above hydrogen storage capacities are amongst the highest reported for MOF-5, the corresponding binding energies are still low. In this work, we explore the feasibility of tuning its hydrogen adsorption properties by doping the organic linker in MOF-5 with light metal ions M = Na^+, Be^{2+}, Mg^{2+}, and Al^{3+} as opposed to Li^+ ion. To this end, in Paper V we study by means of DFT calculations the optimized geometries, atomic charges, and the H_2 binding energies of the corresponding model complexes of the form $MC_6H_6{:}nH_2$.

It must be noted that here in we have not performed any solid-state calculations but have carried out preliminary molecular computations in which the interactions of H_2 molecules with the corner post Zn_4O units have been disregarded. The focus is on investigating the thermodynamical aspects of H_2 desorption over the doped MOF-5 model systems. The effect of the light metal ions on the kinetics of the H_2 uptake/ release processes has not been studied in so far during the course of this work.

6.2
Computational details

In this work we have considered two types of model systems. In the first one n = 1, 2 H_2 molecules are adsorbed over the light metal ions M = Li^+, Na^+, Be^{2+}, Mg^{2+}, and Al^{3+}. In the second case the same ions are adsorbed on top of benzene rings which interact with different number of H_2 molecules to form complexes of the type $MC_6H_6:nH_2$.

The geometries of the M:$1H_2$ and of M:$2H_2$ molecular systems were optimized both using DFT and second-order Møller-Plesset (MP2) perturbation theory without and with constraints, resptectively. The optimization of the geometries for the $MC_6H_6:nH_2$ complexes were done without any constraints at only the DFT level. All the calculations employed the 6-311+G* Pople basis set [30, 31] and were performed using the electronic structure program GAMESS [32]. The DFT functionals considered in the present study were: B3LYP [33, 34], BHHLYP [33, 35], PBELYP [33, 36, 37], and PWLOC [38]. The hydrogen binding energies were calculated as follows:

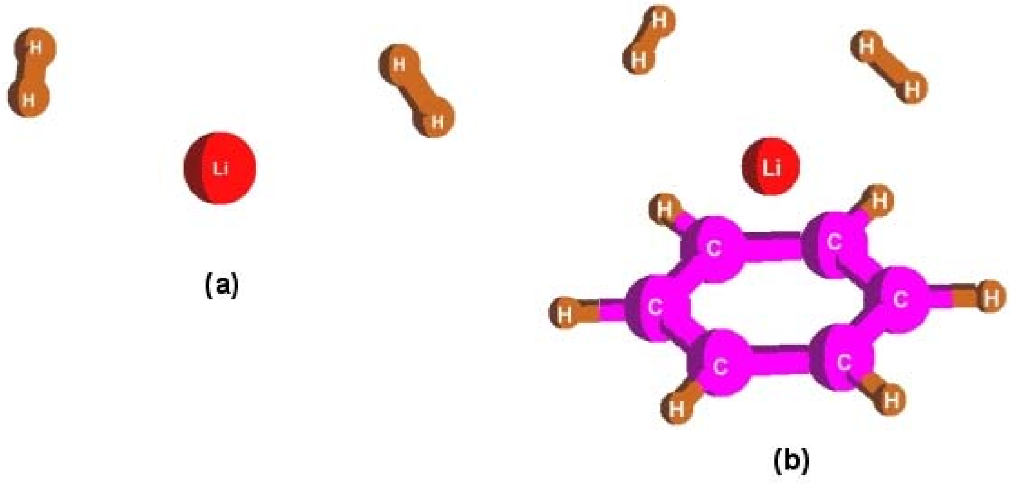

Figure 6.1 The BHHLYP/6-311+G* optimized geometry of (a) $Li^+:2H_2$ and (b) $Li^+C_6H_6:2H_2$.

$$\Delta B.E.[M:nH_2] = E_{tot}[M:(n-1)H_2] + E_{tot}[H_2] - E_{tot}[M:nH_2] \quad (6.2.1)$$

$$\Delta B.E.[MC_6H_6:nH_2] = 1/n\ E_{tot}[MC_6H_6] + E_{tot}[H_2] - 1/n\ E_{tot}[MC_6H_6:nH_2] \quad (6.2.2)$$

The atomic charges have been derived using the ESP method [39] implemented in MOLDEN [40].

6.3

Results and discussion

6.3.1

Model M:1H$_2$ and M:2H$_2$ systems

It is expected that in MC$_6$H$_6$:nH$_2$ complexes the H$_2$ molecules will not be able to interact with the metal ion M from all sides. In order to replicate this structural arrangement the geometries of the M:2H$_2$ systems were optimized under constraints. These structural similarities in the assembly of H$_2$ molecules around the metal ions in both the models can be understood from the geometries of Li$^+$:2H$_2$ and Li$^+$C$_6$H$_6$:2H$_2$, optimized using BHHLYP/6-311+G*, displayed in Fig. 6.1.

The bond distances, ESP derived charge on the metal ion, and H$_2$ binding energies of M:nH$_2$ (M = Li$^+$, Na$^+$, Be^{2+}, Mg^{2+}, and Al^{3+}) models calculated using the four DFT functionals are reported in Table 6.1 where for the purpose of benchmarking these values are compared with the corresponding MP2 results. All functionals were found to perform well with respect to bond distances and atomic charge calculations. However differences can be seen in the binding energies.

Overall the PBELYP functional behaves poorly with the percentage deviation relative to MP2 in ΔB.E. for Na$^+$:2H$_2$ being as high as 53.0 %. With BHHLYP and B3LYP the highest percentage deviations are 19.7 % and 13.8 % respectively for Na$^+$:2H$_2$ and for other systems are between 5-10%. The best binding energies were achieved using the PWLOC functional. The percentage deviations from MP2 results for Li$^+$:2H$_2$, Na$^+$:2H$_2$, Be^{2+}:2H$_2$, Mg^{2+}:2H$_2$, and Al^{3+}:2H$_2$ were 3.2 %, 3.9 %, 1.6 %, 1.5 %, and 1.5 %, respectively. Thus, for the subsequent computations for

Table 6.1 Bond distances, ESP derived atomic charge on M ion, and H_2 binding energies of M:2H_2 models calculated using different DFT functionals and MP2 with 6-311+G* basis set.

Parameter	*Method*	$Li^{+}:2H_2$	$Na^{+}:2H_2$	$Be^{2+}:2H_2$	$Mg^{2+}:2H_2$	$Al^{3+}:2H_2$
M-H (Å)	BHHLYP	(2.011, 2.013)	(2.396, 2.392)	(1.614, 1.615)	(2.062, 2.034)	(1.915, 1.889)
		(1.990, 2.025)	(2.379, 2.403)	(1.614, 1.615)	(2.051, 2.047)	(1.918, 1.888)
	B3LYP	(2.039, 2.037)	(2.396, 2.392)	(1.629, 1.629)	(2.051, 2.092)	(1.920, 1.954)
		(2.009, 2.055)	(2.379, 2.403)	(1.629, 1.629)	(2.045, 2.090)	(2.018, 1.870)
	PBELYP	(2.014, 2.014)	(2.380, 2.381)	(1.636, 1.634)	(2.076, 2.062)	(1.999, 1.954)
		(1.983, 2.034)	(2.359, 2.391)	(1.636, 1.634)	(2.058, 2.076)	(2.070, 1.900)
	PWLOC	(2.040, 2.038)	(2.453, 2.452)	(1.607, 1.608)	(2.056, 2.059)	(1.873, 1.869)
		(2.035, 2.038)	(2.451, 2.453)	(1.607, 1.608)	(2.057, 2.058)	(1.873, 1.869)
	MP2	(2.056, 2.057)	(2.466, 2.466)	(1.627, 1.629)	(2.076, 2.079)	(1.903, 1.899)
		(2.050, 2.054)	(2.464, 2.465)	(1.626, 1.629)	(2.076, 2.078)	(1.903, 1.899)
Q(M) (a.u.)	BHHLYP	0.815	0.882	1.208	1.570	2.033
	B3LYP	0.814	0.882	1.201	1.596	2.002
	PBELYP	0.802	0.866	1.182	1.545	1.952
	PWLOC	0.832	0.899	1.242	1.610	2.108
	MP2	0.829	0.897	1.234	1.604	2.090
ΔB.E. (kJ/mol)	BHHLYP	27.55	16.01	206.72	93.95	308.61
	B3LYP	26.51	15.22	205.74	93.69	310.71
	PBELYP	32.80	20.47	217.03	104.50	322.52
	PWLOC	25.72	12.86	193.93	83.98	287.62
	MP2	24.93	13.38	197.08	85.29	292.08

$Li^+C_6H_6:nH_2$ complexes only PWLOC, BHHLYP, and B3LYP were used and the PBELYP functional was disregarded.

A point to note is that irrespective of the method used the binding energy follows the order: $Na^+ < Li^+ < Mg^{2+} < Be^{2+} < Al^{3+}$.

6.3.2
$Li^+C_6H_6:nH_2$ complexes

The binding energy of n = 1 – 3 H_2 molecules adsorbed over $Li^+C_6H_6$ computed using BHHLYP, B3LYP, and PWLOC functionals are presented in Table 6.2. The appropriateness of these functionals is tested against previously reported binding energies evaluated by Blomqvist et al. [25] via a periodic DFT plane wave-pseudopotential based method. It can be seen in comparison to BHHLYP, B3LYP yields poor ΔB.E. for all numbers of H_2 molecules. PWLOC predicts the ΔB.E. for n = 1 and 2 H_2 molecules to a reasonable agreement with the periodic DFT results but fails for $Li^+C_6H_6:3H_2$. In contrast BHHLYP exhibits good concurrence for all n.

Table 6.2 Hydrogen binding energies calculated for $Li^+C_6H_6:nH_2$ (n = 1-3) systems in this work using different DFT functionals compared with previously reported results in Ref. [25] and ESP derived atomic charge on Li^+ ion obtained with BHHLYP/6-311+G* method.

System	*ΔB.E. (kJ/mol) (This work) 6-311+G* basis set*			*ΔB.E. (kJ/mol) Ref. [25] (Plane wave basis set)*	*Q(Li^+)*
	BHHLYP	*B3LYP*	*PWLOC*	*PW91*	*BHHLYP*
$Li^+C_6H_6$					+0.62 e
$Li^+C_6H_6:1H_2$	18.37	16.27	19.42	18	+0.39 e
$Li^+C_6H_6:2H_2$	13.65	12.33	13.25	16	+0.34 e
$Li^+C_6H_6:3H_2$	11.55	9.62	5.25	12	+0.23 e

These observations firstly lend confidence to our calculations using BHHLYP, which is applied henceforth exclusively for all further computations. Secondly, these suggest that up to a rational degree of accuracy it is fitting to consider only the organic linker moiety of MOF-5 instead of the entire unit cell consisting of 106 atoms.

We notice that as the number of H_2 molecules increases, the corresponding binding energy decreases. But the magnitude of decrease in energy at n = 3 (2.10 kJ/mol) is smaller than at n = 2 (4.72 kJ/mol) implying that it easier adding the subsequent H_2 molecules.

Table 6.2 also lists the ESP derived charge over Li^+ ion in $Li^+C_6H_6$:nH_2 complexes calculated with BHHLYP/6-311+G*. It is seen that the charge on the ion also decreases along with the binding energy from +0.62 e to +0.23 e. This is understandable because as more number of H_2 molecules interacts with Li^+ ion, the charge available on it depletes in the process.

We have in addition optimized the geometry of $Li^+C_6H_6$:$4H_2$ and found that the calculated charge on Li^+ ion here was +0.25 e which is very close in magnitude to that in $Li^+C_6H_6$:$3H_2$. This suggests that the fourth H_2 is being held together due to its interaction with the previously adsorbed H_2 molecules and not with the Li^+ ion.

In Fig. 6.2 we display the BHHLYP/6-311+G* optimized geometries of the above mentioned $Li^+C_6H_6$:nH_2 (n = 0 - 4) systems along with their corresponding Li^+-ring and Li^+-H distances, where H atoms belong to the adsorbed H_2 molecules. It is evident that the first H_2 molecule is adsorbed on top of the $Li^+C_6H_6$. As n increases from one to three, the arrangement of the H_2 molecules changes in order to accommodate the newer H_2 molecules around the Li^+ ion. These modifications were accompanied with a simultaneous increase in the distance of the Li^+ ion from both the benzene ring and the adsorbed H_2 molecules. This may be a result of the weakening of interactions with increasing n as suggested by the reduced H_2 binding energies.

The view of $Li^+C_6H_6$:nH_2 taken from the top is also illustrated in Fig. 6.2. It can be seen that when the fourth H_2 molecule is added the structural rearrangement occurs in such a way that two H_2 molecules are pushed away while two H_2 molecules are brought closer to Li^+ ion. For two of the H_2 molecules the Li^+-H distances are ~3 Å and for the other two the Li^+-H distances are similar in magnitude to those in

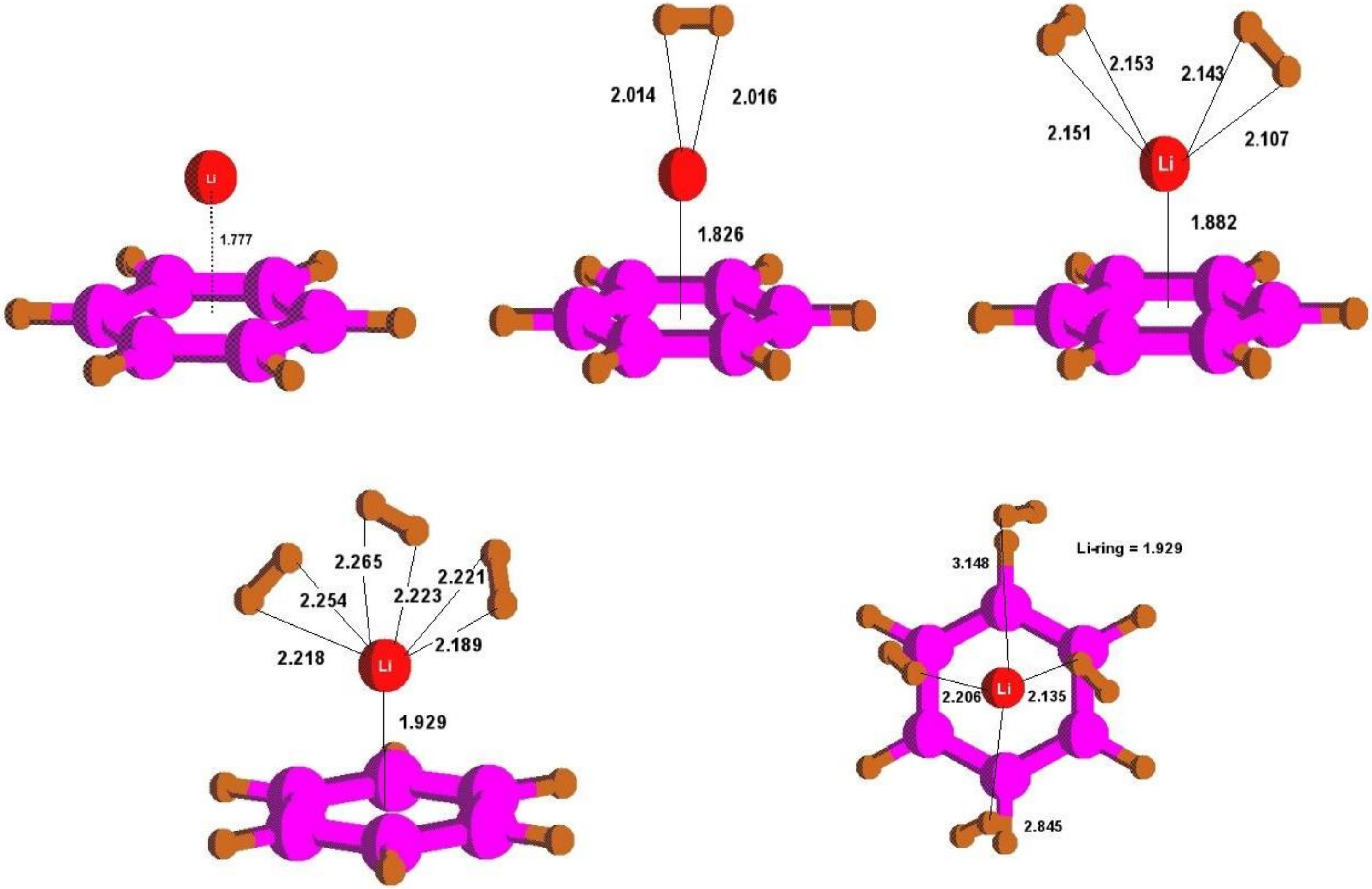

Figure 6.2 BHHLYP/6-311+G* optimized geometries of $Li^{+}C_6H_6{:}nH_2$ systems where n = 0 - 4. All the bond distances are in Å.

$Li^+C_6H_6$:$2H_2$. This picture in which two of the four H_2 molecules are thrown out by $Li^+C_6H_6$ could be due to an attempt of the small sized Li^+ ion to reduce the overcrowding around it. Thus, the structural geometry analysis shows that Li^+ ion in $Li^+C_6H_6$ is capable of adsorbing maximum of three H_2 molecules.

Recalling, the binding energy for $Li^+C_6H_6$:$3H_2$ is 11.55 kJ/mol which is nearly thrice that for pure C_6H_6 [2-4]. However, this value is still low and thus at operating conditions in practical H_2 storage applications less than three H_2 molecules may be adsorbed. It was indeed shown by Blomqvist et al. [25] from *ab initio* molecular dynamics simulations in a cell containing 18 H_2/f.u. of Li-decorated MOF-5 that at temperatures up to at least 200 K Li was coordinated with only two hydrogen molecules and at 300 K only approximately two-thirds H_2 remained bound to it.

All the above mentioned observations give incite regarding the attributes needed in a better metal ion dopant compared to Li^+ for enhancing the H_2 storage attributes of MOF-5. The metal ions M in MC_6H_6 should have a higher charge and larger size to avoid steric hindrance as number of H_2 molecules increases. At the same time it must be lightweight to ensure a high gravimetric H_2 storage capacity. Furthermore, its H_2 binding energies should be greater than for $Li^+C_6H_6$ and should lie in between the physisorption and chemisorption energy range of 20.0-50.0 kJ/mol. Thus, in the following section we compare the effectiveness of using Na^+, Be^{2+}, Mg^{2+}, and Al^{3+} ions versus Li^+ ion for improving hydrogen storage in MOF-5 with respect to each of the above points.

6.3.3

MC_6H_6:nH_2 complexes

The variation of the charge over M ion in MC_6H_6 complexes as a function of number of H_2 molecules is displayed in Figure 6.3 and Table 6.3 lists the corresponding bond distances and H_2 binding energies. It is noticeable that for n = 0 the charge available over M ion in MC_6H_6 exhibits the following sequence: $Li^+ < Na^+ \sim Be^{2+} < Mg^{2+} < Al^{3+}$. To understand the differences in $Li^+C_6H_6$ and $Na^+C_6H_6$ we have calculated the interaction energy of M ions with the benzene ring using the formula:

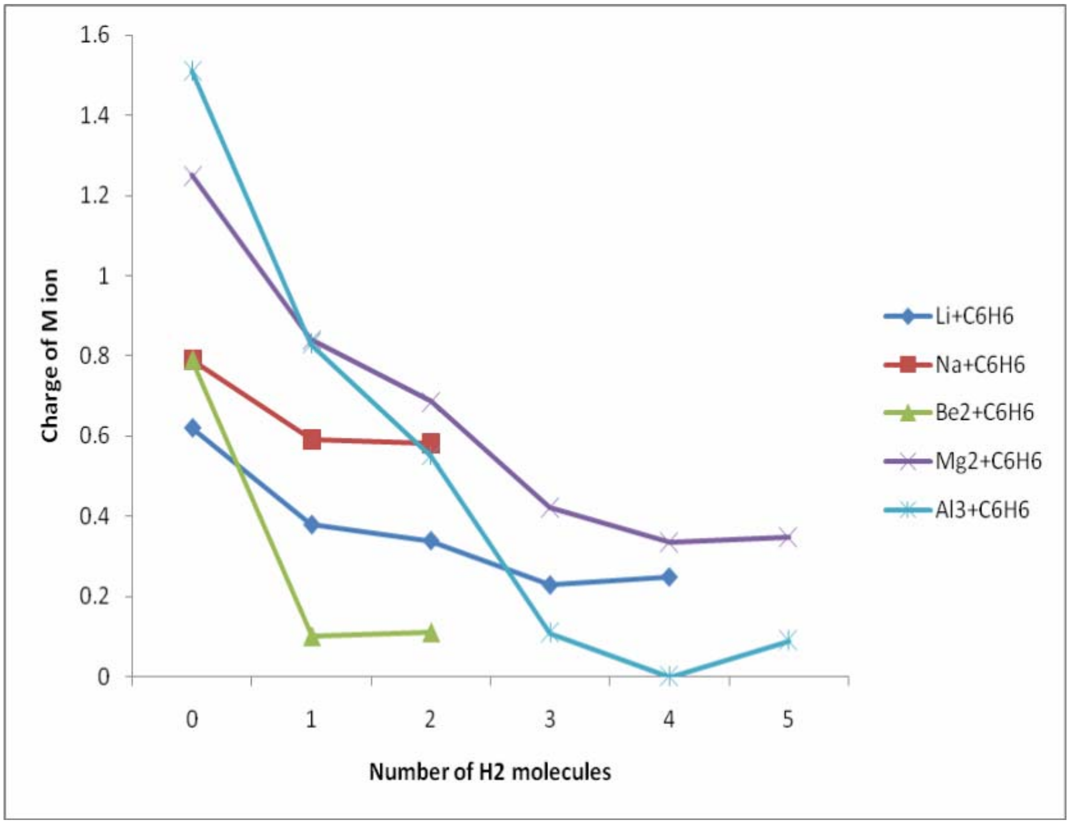

Figure 6.3 Variation of BHHLYP/6-311+G* ESP derived charge over M ion in $MC_6H_6{:}nH_2$ complexes with number of H_2 molecules adsorbed.

$$\Delta E[MC_6H_6] = E_{tot}[MC_6H_6] - E_{tot}[M] - E_{tot}[C_6H_6] \qquad (6.2.3)$$

The ΔE shows the trend: $Na^+ < Li^+ < Mg^{2+} < Be^{2+} < Al^{3+}$. Due to the much stronger interaction of Li^+ with C_6H_6 than of Na^+ ion it is more strongly adsorbed on top of the benzene. Consequently distance of the former from the benzene ring is much shorter than of Na^+ ion and the charge available over it to interact with H_2 molecules is smaller. However, a similar correlation cannot be simply drawn between the interaction energies and charge for the other M ions. For a correct interpretation one must look at the amount of charge transferred by the M ion to the benzene ring. This charge transfer Q_{trans} can be obtained as the difference between the charge of the bare ion and charge over the ion in the MC_6H_6 complex. The following order of Q_{trans}

Table 6.3 BHHLYP/6-311+G* calculated bond distances and H_2 binding energies in MC_6H_6:nH_2 models where M = Na^+, Be^{2+}, Mg^{2+}, and Al^{3+}.

System	***M-ring (Å)***	***M-H (Å)***	***ΔB.E. (kJ/mol)***
$Na^+C_6H_6$	2.373		
$Na^+C_6H_6:1H_2$	2.377	(2.404, 2.434)	14.70
$Na^+C_6H_6:2H_2$	2.391	(2.458, 2.456) (2.465, 2.443)	12.33
$Be^{2+}C_6H_6$	1.295		
$Be^{2+}C_6H_6:1H_2$	1.347	(1.602, 1.606)	113.32
$Be^{2+}C_6H_6:2H_2$	1.351	(1.613, 1.569) (3.423, 3.412)	62.33
$Mg^{2+}C_6H_6$	1.924		
$Mg^{2+}C_6H_6:1H_2$	1.949	(2.077, 2.078)	66.66
$Mg^{2+}C_6H_6:2H_2$	1.982	(2.140, 2.136) (2.140, 2.116)	54.45
$Mg^{2+}C_6H_6:3H_2$	2.018	(2.191, 2.161) (2.180, 2.159) (2.191, 2.166)	46.71
$Mg^{2+}C_6H_6:4H_2$	2.047	(2.266, 2.246) (2.260, 2.229) (2.275, 2.240) (2.253, 2.236)	38.45
$Mg^{2+}C_6H_6:5H_2$	2.047	(2.204, 2.215) (2.282, 2.258) (2.261, 2.218) (2.282, 2.258) (4.104, 4.168)	30.34
$Al^{3+}C_6H_6$	1.642		
$Al^{3+}C_6H_6:1H_2$	1.669	(1.900, 1.883)	178.97
$Al^{3+}C_6H_6:2H_2$	1.743	(1.967, 1.961) (1.966, 1.966)	131.61
$Al^{3+}C_6H_6:3H_2$	1.754	(2.044, 2.003) (2.038, 2.012) (1.996, 2.051)	106.81
$Al^{3+}C_6H_6:4H_2$	1.808	(2.152, 2.101) (2.110, 2.068) (2.060, 2.088) (2.161, 2.091)	81.94
$Al^{3+}C_6H_6:5H_2$	1.782	(2.059, 2.027) (2.031, 2.011) (1.860, 2.046) (3.190, 3.251) (3.759, 3.599)	70.64

ensues: Na^+ (+0.21 e) < Li^+ (+0.38 e) < Mg^{2+} (+0.75 e) < Be^{2+} (+1.21 e) < Al^{3+} (1.49 e) which clearly reflects the ΔE variation.

From Fig. 6.3 it is evident that as H_2 molecules are added the charge available over M in MC_6H_6:nH_2 complexes falls. When n = 1 H_2 the most drastic decrease of ~0.7 e occurs for M = Be^{2+} and Al^{3+}. As number of H_2 molecules increases the magnitude of decrease in charge reduces such that beyond a particular n, charge saturation sets in.

Examination of Table 6.3 shows that the H_2 binding energy displays the following two trends: (i) for all M as n increases ΔB.E. decreases and (ii) for the same n, ΔB.E. increases according to the order $Na^+ < Li^+ < Mg^{2+} < Be^{2+} < Al^{3+}$. The latter point implies in our choice for M, as one goes down a group in the periodic table ΔB.E. decreases while as we go across a row in the periodic table ΔB.E. increases.

The H_2 binding energies for $Na^+C_6H_6$ are even smaller than for $Li^+C_6H_6$. Even though it might have the capacity to interact with more number of H_2 molecules because of the poor adsorption energies Na^+-doped MOF-5 will be unable to withstand room temperature and atmospheric pressure conditions needed for practical H_2 storage. In comparison the first H_2 binding energies of $Be^{2+}C_6H_6$ and $Al^{3+}C_6H_6$ are approximately six times and nine times, respectively, of the first H_2 binding energies of $Li^+C_6H_6$. Thus, H_2 adsorption in these complexes might be associated with high energy barriers.

For $Mg^{2+}C_6H_6$ ΔB.E. decreases from 66.66 kJ/mol at n = 1 to 30.34 kJ/mol at n = 5. Recalling 20.0-50.0 kJ/mol as the energy range deemed appropriate for vehicular H_2 storage implies that Mg^{2+}-doped MOFs particularly attractive from a thermodynamics point of view. The corresponding BHHLYP/6-311+G* optimized geometries of the $Mg^{2+}C_6H_6$:nH_2 (n = 1 - 5) complexes are depicted in Fig. 6.4 along with selected bond distances. As n increases from one to four, the H_2 molecules rearranged themselves around the Mg^{2+} ion to accommodate each other. However, when the fifth H_2 molecule was added it was thrown out in order to minimize the resulting overcrowding. Its distance from Mg^{2+} ion was calculated to be 4.232 Å. This implies that per Mg^{2+} ion a maximum of four H_2 molecules can get adsorbed.

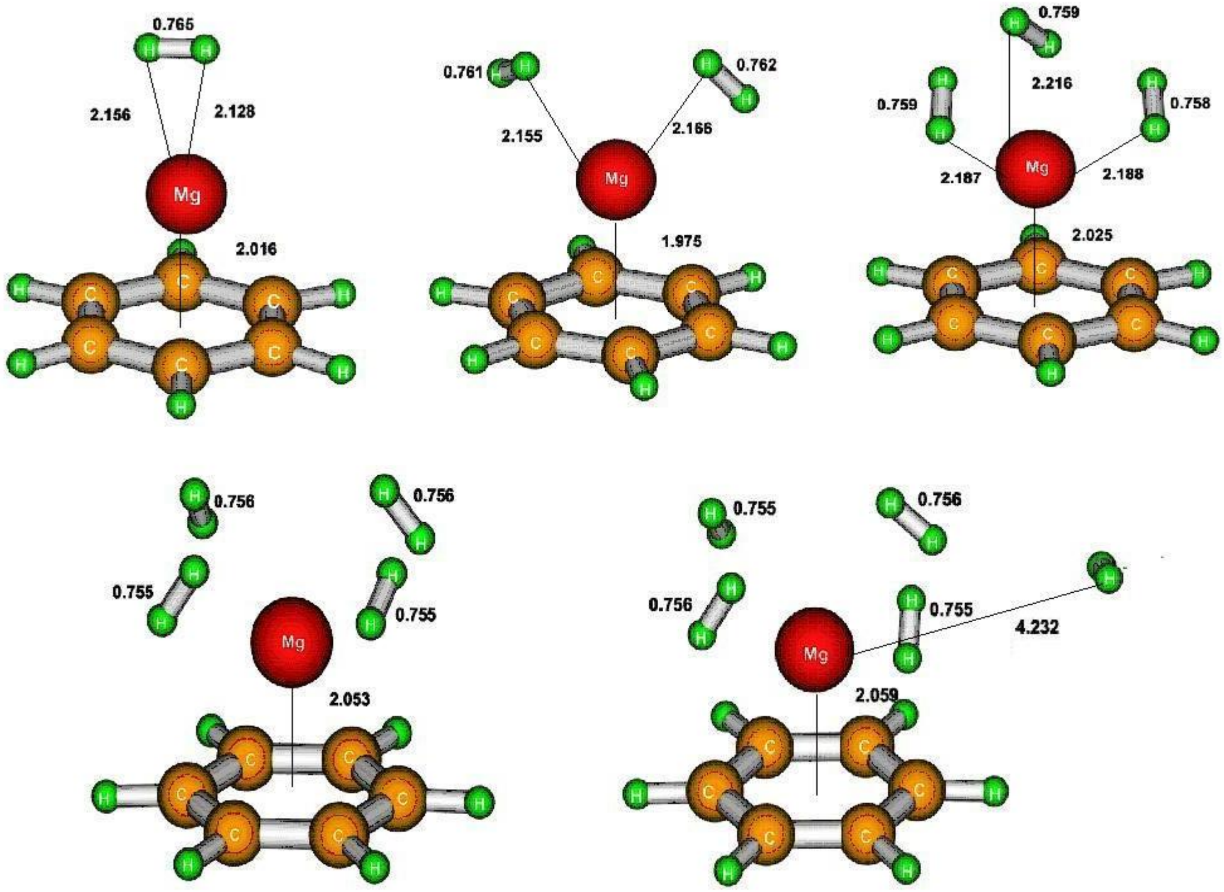

Figure 6.4 The BHHLYP/6-311+G* optimized geometries of $Mg^{2+}C_6H_6{:}nH_2$ systems where n = 1 - 5. All the bond distances are in Å.

Assuming each side of benzene ring in MOF-5 to be doped by one Mg^{2+} ion would lead to a formula unit of $Zn_4O(BDCMg_2(H_2)_4)_3$, that is, a H_2 storage capacity of 5.0 wt.%. Thus, amongst all the metal ions investigated in this study only Mg^{2+} doping proves suitable for both enhancing the hydrogen storage capacity of MOF-5 and yielding H_2 binding energies that would make room temperature H_2 storage applications of MOF-5 possible.

6.4
Conclusions

Herein we have studied the effect of light metal ion doping on H_2 adsorption of MOF-5 by examining the structures, atomic charges, and binding energies (ΔB.E.) complexes of the form $MC_6H_6{:}nH_2$ where M = Li^+, Na^+, Be^{2+}, Mg^{2+}, and Al^{3+}. It should be stressed that these are molecular calculations which serve as a preliminary investigation to future solid-state periodic DFT studies. However, our results provide a simplistic approach for predicting the trends in actual light metal ion decorated MOF-5 systems. Our systematic investigations revealed BHHLYP as the most suitable functional for the systems under study. A correlation between charge transfer from the M ions to the benzene ring and the interaction of metal ions with the benzene rings was illustrated. The calculated H_2 binding energies of $Li^+C_6H_6{:}nH_2$ and $Na^+C_6H_6{:}nH_2$ systems were found to be low and of $Be^{2+}C_6H_6{:}nH_2$ and $Al^{3+}C_6H_6{:}nH_2$ models were too high to prove useful as good hydrogen adsorbents at room temperature. In comparison doping C_6H_6 with Mg^{2+} ions was predicted to enhance its hydrogen adsorption as well as bring the H_2 binding energies within the suitable range of 20.0-50 kJ/mol that is a necessary requirement for practical H_2 storage applications.

References

1. M. Eddaoudi, H. Li, T. Reineke, M. Fehr, D. Kelley, T. L. Groy, and O. M. Yaghi, *Top. Catal.* **1999**, *9*, 105.
2. J. L. C. Roswell and O. M. Yaghi, *J. Am. Chem. Soc.* **2006**, *128*, 1304.

3. S. Bordiga, J. G. Vitillo, G. Ricchiardi, L. Regli, D. Cocina, A. Zecchina, B. Arstad, M. Bjørgen, J. Hafizovic, and K. P. J. Lillerud, *J. Phys. Chem. B* **2005**, *109*, 18237.
4. S. S. Kaye and J. R. Long, *J. Am. Chem. Soc.* **2005**, *127*, 6506.
5. N. L. Rosi, J. Eckert, M. Eddaoudi, D. T. Vodak, J. Kim, M. O'Keeffe, and O. M. *Science* **2003**, *300*, 1127.
6. J. L. C. Roswell, A. R. Milward, K. S. Park, and O. M. Yaghi, *J. Am. Chem. Soc.* **2004**, *126*, 5666.
7. X. Lin, J. Jia, X. Zhao, K. M. Thomas, A. J. Blake, G. S. Walker, N. R. Champness, P. Hubberstey, and M. Schröder, *Angew. Chem., Int. Ed.* **2006**, *45*, 7358.
8. G. Wong-Foy, A. J. Matzger, and O. M. Yaghi, *J. Am. Chem. Soc.* **2006**, *128*, 3494.
9. J. L. C. Roswell and O. M. Yaghi, *J. Am. Chem. Soc.* **2006**, *128*, 1304.
10. M. Latroche, S. Surblè, C. Serre, C. Mellot-Draznieks, P. L. Llewellyn, J. H. Lee, J. S. Chang, S. H. Jhung, and G. Fèrey, *Angew. Chem., Int. Ed.* **2006**, *45*, 8227.
11. O. I. Lebedev, F. Millange, C. Serre, G. van Tendeloo, and G. Fèrey, *Chem. Mater.* **2005**, *17*, 6525.
12. A. Kuc, T. Heine, G. Seifert, and H. A. Duarte, *Chem. Eur. J.* **2008**, *14*, 6597.
13. A. Kuc, T. Heine, G. Seifert, and H. A. Duarte, *Theor. Chem. Account* **2008**, *120*, 543.
14. W. Kohn and L. J. Sham, *Phys. Rev. A* **1965**, *140*, 1133.
15. M. Rapacioli, F. Spiegelman, D. Talbi, T. Mineva, A. Goursot, T. Heine, and G. Seifert, *J. Chem. Phys.* **2009**, *130*, 244304.
16. J. Niu, B.K. Rao, and P. Jena, *Phys. Rev. Lett.* **1992**, *68*, 2277.
17. J. Niu, B.K. Rao, S.N. Khanna, and P. Jena, *Chem. Phys. Lett.* **1994**, *230*, 299.
18. C.W. Bausclicher and S.P. Walch, *J. Chem. Phys.* **1982**, *76*, 4560.
19. F. Maseras, A. Lledo, E. Clot, and O. Eisenstein, *Chem. Rev.* **2000**, *100*, 601.
20. L. Gagliardi and P.K. Pyykko, *J. Am. Chem. Soc.* **2004**, *126*, 15014.
21. K. R. S. Chandrakumar and S. K. Ghosh, *Chem. Phys. Lett.* **2007**, *447*, 208.

22. S. Barman, P. Sen, and G. P. Das, *J. Phys. Chem. C* **2008**, *112*, 19963.
23. S. Bhattacharya, C. Majumder, and G. P. Das, *J. Phys. Chem. C* **2008**, *112*, 17487.
24. K. R. S. Chandrakumar and S. K. Ghosh, *Nano Lett.* **2008**, *8*, 13.
25. A. Blomqviśt, C. M. Araújo, P. Srepusharawoot, and R. Ahuja, *Proc. Natl. Acad. Sci.* **2007**, *104*, 20173.
26. N. S. Venkataramanan, R. Sahara, H. Mizuseki, and Y. Kawazoe, *Int. J. Mol. Sci.* **2009**, *10*, 1601.
27. K. Srinivasu, K. R. S. Chandrakumar and S. K. Ghosh, *Phys. Chem. Chem. Phys.* **2008**, *10*, 5832.
28. K. R. S. Chandrakumar, K. Srinivasu, and S. K. Ghosh, *J. Phys. Chem. C* **2008**, *11*, 15670.
29. K. Srinivasu, K. R. S. Chandrakumar and S. K. Ghosh, *ChemPhysChem* **2009**, *10*, 427.
30. R. Krishnan, J. S. Binkley, R. Seeger, and J. A. Pople, *J. Chem. Phys.* **1980**, *72*, 650.
31. A. D. McLean and G. S. Chandler, *J. Chem. Phys.* **1980**, *72*, 5639.
32. M. W. Schmidt, K. K. Baldridge, J. A. Boatz, S. T. Elbert, M. S. Gordon, J. J. Jensen, S. Koseki, N. Matsunaga, K. A. Nguyen, S. Su, T. L. Windus, M. Dupuis, and J. A. Montgomery, *J. Comput. Chem.* **1993**, *14*, 1347.
33. A. D. Becke, *J. Chem. Phys.* **1993**, *98*, 5648.
34. P. J. Stephens, F. J. Devlin, C. F. Chablowski, and M. J. Frisch, *J. Phys. Chem.* **1994**, *98*, 11623.
35. C. Lee, W. Yang, and R. G. Parr, *Phys. Rev. B* **1988**, *37*, 785.
36. J. P. Perdew, K. Burke, and M. Ernzerhof, *Phys. Rev. Lett.* **1996**, *77*, 3865; **1996**, *78*, 1396 (E).
37. M. Ernzerhof and G. E. Scuseria, *J. Chem. Phys.* **1999**, *110*, 5029.
38. J. P. Perdew and Y. Wang, *Phys. Rev. B* **1992**, *45*, 13244.
39. R. Bonaccorsi, E. Scrocco, and J. Tomasi, *J. Chem. Phys.* **1970**, *54*, 5270.
40. G. Schaftenaar and J. H. Noordik, *J. Comput.-Aided Mol. Design* **2000**, *14*, 123.

CHAPTER 7

Summary and future scope

This is not the ***end****. It is not even*
the beginning of the end.
But it is, perhaps,
the end of the beginning.
-Winston Churchill

In this thesis we have computationally investigated solid-state storage of hydrogen for fuel cells by first-principles calculations. Our studies have focused on complex metal hydrides, magnesium hydride, and metal-organic frameworks which have several favorable hydrogen storage properties. We have in particular examined the effect of presence of high pressure phases, doping by light metal ions, and temperature on these materials.

Our investigations on α- and β-$LiAlH_4$ and $LiBH_4$ revealed that the α phases were more stable than the β phases and that substitution of B by Al decreased the stability of the complex metal hydride. From an analysis of the reaction energies β-$LiBH_4$ was predicted to exhibit the most potential for hydrogen storage amongst the four complex metal hydrides studied.

We showed through periodic density functional theory calculations that the high pressure phases of MgH_2 demonstrated the following order for heats of formation (ΔH_f): β-MgH_2 << γ-MgH_2 ~ α-MgH_2. Their corresponding activation energy barriers (E_{act}) obtained for the one-step direct dehydrogenation path from the (001) MgH_2 surfaces displayed an almost similar trend: β-MgH_2 << γ-MgH_2 < α-MgH_2. This lead to the conclusion that using the pure β phase would lead to a lowering of the energy requirement for hydrogen removal and to a faster kinetics for hydrogen desorption from MgH_2.

Further, we studied the influence of fractional substitution of Mg in MgH_2 by Al and Si. The band structure and density of states analysis showed that for all the three phases the impurities resulted in generation of additional bands in between the band gaps of the analogous pure magnesium hydrides. It was suggested that the decrease in band gap due to presence of Al and Si could cause an easier Mg-H bond dissociation. Our calculations showed that this was reflected in the decreased ΔH_f of the doped magnesium hydride phases. Irrespective of the phase, between the two dopants Si was found to consistently decrease ΔH_f more than Al doping. However, no consistent trends were exhibited by E_{act} for hydrogen desorption from the Al- and Si-doped (001) MgH_2 surfaces. Our simplistic calculations thereby showed the necessity for performing a combined study of the dehydrogenation reaction energies and the hydrogen desorption kinetics for recognizing the true potential of dopants for enhancing the hydrogen storage properties of potential materials.

A preliminary study was also carried out for understanding the effect of doping by light metal ions on the hydrogen storage properties of metal-organic framework (MOF)-5. Molecular complexes of the benzene ring, which is the organic linker in MOF-5, with the metal ions M = Li^+, Na^+, Be^{2+}, Mg^{2+}, and Al^{3+} and different number (n) of hydrogen molecules were used for modeling the interactions in the actual solid-state MOF-5 system. We showed that though doping with M ions increased the hydrogen adsorption as compared to the pure organic linker, the corresponding hydrogen binding energies (ΔB.E.) for M = Li^+ and Na^+ were low and for M=Be^{2+} and Al^{3+} were significantly large. In comparison ΔB.E. of $Mg^{2+}C_6H_6{:}nH_2$ complexes were calculated to lie in the range of 20.0-50.0 kJ/mol indicating that Mg-doped MOF-5 could be suitable for practical hydrogen storage applications at room temperature.

For including the temperature effects on the thermodynamical properties of MgH_2 we employed the quasiharmonic approximation (QHA). The reasonable agreement between our calculated entropies and heat capacities at constant pressure with experimental results within the finite temperature range of 0-1000 K illustrated that QHA could be used as a theoretical approach for calculating these quantities even at temperatures greater than the melting point of MgH_2. It was also found that the calculated percentage decrease in bulk modulus (K_0) with temperature superseded the percentage increase in equilibrium cell volume (V_0). As bulk modulus is inversely related to compressibility it indicated that application of a temperature slightly greater than room temperature could be used for enhancing the volumetric hydrogen storage capacity of MgH_2 due to its increased compressibility.

An important point to remember is that except for the QHA based study for MgH_2, all other calculations were performed at 0 K and do not include zero-point corrections. In the future we plan to evaluate the reaction energies and activation energy barriers at 298 K for better comparison with experimental results. Our studies on MOFs in so far have focused only on the hydrogen adsorption energies. A possible extension of this work would involve studying the hydrogen desorption kinetics of these systems. Further, in our calculations we modeled doped MOF-5 systems as molecular complexes of the benzene ring with the light metal ions and hydrogen molecules. In this process the interactions due to the oxygen centered Zn tetrahedral clusters forming the cornerposts were completely disregarded. Thus, such preliminary studies need to be followed by periodic solid-state calculations in order to take into account the whole unit cell of the MOF under investigation. An attractive class of materials that can further be explored is that of clathrate hydrates. It has been shown that promoter molecules can lead to binary clathrate systems with a more advantageous balance between clathrate formation conditions and hydrogen storage capacity. Given the large range of promoter compounds, computational modeling can help in gaining insight about the potential of such promoted hydrogen containing clathrate hydrates. Furthermore, it is important to include quantum effects into the calculations to reproduce experimental results for the above hydrogen storage materials. The effect of isotopic substitution also needs to be addressed in the future.

A possible approach for such studies would require performing path integral molecular dynamics calculations.

In the last decade there have been significant scientific discoveries in the field of hydrogen storage materials. However, for vehicular hydrogen storage applications still further developments are needed in these currently existing technologies. This thesis shows that suitable chemical modifications can bring about such improvements. Our work clearly displays that computational studies can lead to better understanding of the underlying mechanisms of the hydrogen adsorption and desorption processes of the potential candidates and can also help in better designing of new hydrogen storage materials.